

Research Activities

Observation of Smith-Purcell radiation in Terahertz regime at electron linear accelerator LEENA

S.Hashimoto, S. Chin, K. Kawata, Y. Minagawa[#], Y. Takemura[#], D. Li^{*}, S. Amano, S. Miyamoto
LASTI, University of Hyogo

[#]JASRI

^{*}Institute for Laser Technology

Abstract

Terahertz radiation by the Smith-Purcell effect was successfully observed using 15 MeV electron beams of the linear accelerator LEENA. The radiation properties such as the angular dependence of peak wavelength were measured. Wavelength spectrum measured by the Martin-Puplett interferometer is very clear and the peak wavelength well corresponds to the calculated one.

Introduction

In order to develop high peak power, wide range (0.1-10 THz) and tunable terahertz radiation sources using relativistic electron beams, we have been upgrading the compact electron linear accelerator LEENA [1-5]. The electron beams with bunch length shorter than the wavelength of emitted light can generate high power radiation by coherent radiation. The main parameters of LEENA are shown in Table. I. In addition to the synchrotron radiation from a bending magnet, the Smith-Purcell radiation from a metal grating plate near an electron orbit was successfully observed. The spectrum of Smith-Purcell radiation was measured with the Martin-Puplett interferometer. In this paper we report the present status of the Smith-Purcell radiation in a terahertz regime.

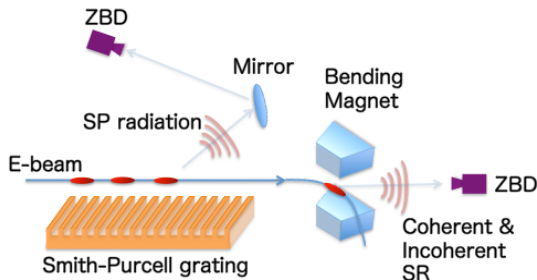


Fig.1 Observation of Terahertz radiation using LEENA electron beams; synchrotron radiation and Smith-Purcell radiation.

Table I Main parameters of LEENA.

Beam energy	6-15 [MeV]
Macropulse current	100 [mA]
Macropulse width	5 [us]
Repetition frequency	10 [Hz]
Gun	RF gun
Cathode	LaB ₆ (thermal)
Bunch length	~30 [ps]

Experimental results of Smith-Purcell radiation

The copper plate with grating period of 10 mm is equipped in a vacuum chamber of the LEENA. Using three mirrors located in the chamber, terahertz radiation can be extracted into the air through a quartz viewport. The Smith-Purcell radiation in a terahertz regime was measured with a Zero Bias Detector. Measured radiation power is about ten micro Watt. Because present bunch length is longer than terahertz wavelength, the measured radiation is incoherent.

The emitted wavelength of Smith-Purcell radiation has an angular dependence, i.e., shorter wavelength light is radiated in the forward direction and longer wavelength in the backward direction. The mirrors in the chamber can rotate according to the desired angle for measurement. Fig. 2 shows the angular dependence of radiation power measured by the two detectors with different measurement ranges. The calculated emission angle for the light of 0.075-0.11 THz is about 40 degrees and for 0.11-0.17 about THz 50 degrees. Experimental results show a good agreement to the calculation.

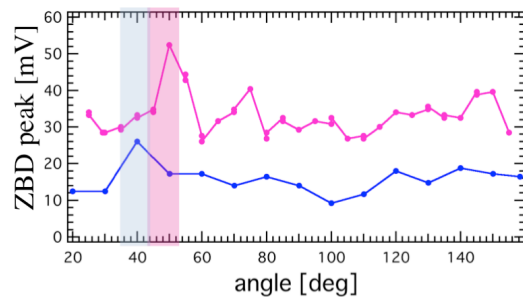


Fig.2 Observation of angular distribution of Smith-Purcell radiation power. Two detectors with different measurement ranges are used: 0.11-0.17 THz (upper) and 0.075-0.11 THz (lower).

Smith-Purcell radiation spectrum measured by Martin-Puplett interferometer

In a terahertz regime, the wire grid reflects the radiation component whose direction of the polarization plane is parallel to the wire and transmits the perpendicular component. The Martin-Puplett interferometer uses wire grids as a divider of terahertz light as shown in Fig. 3. The interferogram made from a path length difference between two lights by moving a mirror was measured with a ZBD. By the Fourier transform of this interferogram data, the wavelength spectrum of Smith-Purcell light is obtained as shown in Fig.4. Measured peak wavelength of Smith-Purcell light is 3.4 mm and is well corresponding to the calculations.

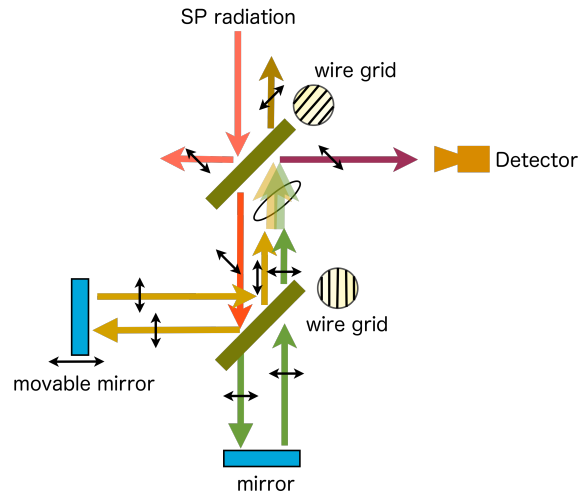


Fig.3 Martin-Puplett Interferometer

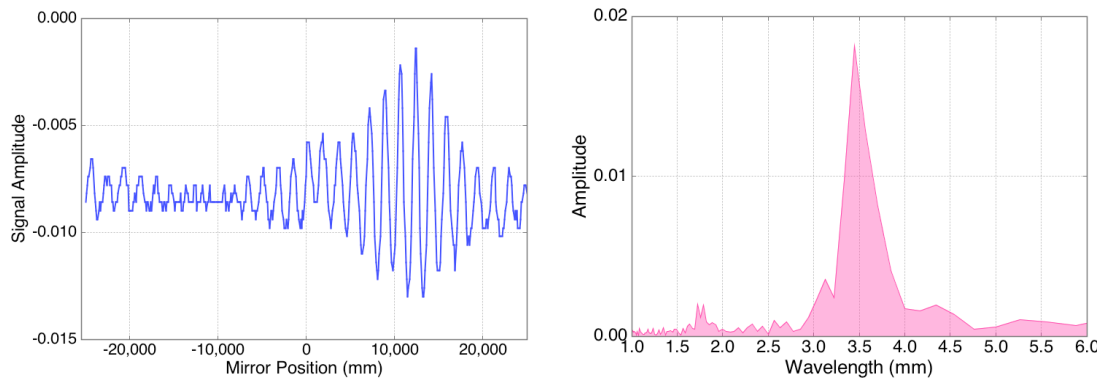


Fig.4 Interferogram of Smith-Purcell radiation measured with Martin-Puplett interferometer (left) and its FFT result (right).

Summary and Future plan

The Smith-Purcell light was successfully observed at LEENA accelerator. The observed terahertz radiation is incoherent, that is the electron bunch length is longer than the light wavelength. If the bunch length becomes shorter than the light wavelength, coherent radiation occurs and radiation intensity becomes several orders higher. To make electron bunch shorter using an alpha magnet effectively, new solenoid coil is under construction just after the electron gun to suppress beam divergence. The emission angle of coherent Smith-Purcell (CSP) radiation depends on the electron bunch length. Thus CSP is not only a powerful terahertz light source but also a useful beam monitor for electron bunch length in linear accelerators.

And the construction of new terahertz beam-line for user experiments will be started in the summer of 2013.

References

- [1] S.Hashimoto *et al.*, Lasti Annual Report, **12**, pp.13-14 (2010).
- [2] S.Hashimoto *et al.*, Lasti Annual Report, **13**, pp.11-12 (2011).
- [3] S.Hashimoto *et al.*, The 8th Annual Meeting of Particle Accelerator Society in Japan (2011).
- [4] S.Hashimoto *et al.*, The 9th Annual Meeting of Particle Accelerator Society in Japan (2012).
- [5] S.Chin *et al.*, The 9th Annual Meeting of Particle Accelerator Society in Japan (2012).

Energy calibration of electron beams by laser Compton-scattering γ -rays at BL01

H. Utsunomiya¹, T. Shima², K. Takahisa², D.-M. Filipescu³, O. Tesileanu³, I. Gheorghe³, H.-T. Nyhus⁴,
T. Renstrøm⁴, Y.-W. Lui⁵, Y. Kitagawa⁶, S. Amano⁶, S. Miyamoto⁶
¹Konan Univ., ²Osaka Univ., ³IFIN-HH Romania, ⁴Univ. Oslo, ⁵Texas A&M Univ., ⁶LASTI-UH

Abstract

We have calibrated electron beam energies in a nominal energy range 550 - 974 MeV using laser-Compton scattering γ -ray beams at the synchrotron radiation facility NewSUBARU. The γ -ray beams were produced at energies from 562 keV to 1727 keV and detected with a high-purity germanium detector. The electron beam energies were determined by reproducing the full energy peaks of the γ -ray beams by Monte Carlo simulations with a precision of 0.068% in 1σ .

Introduction

In the NewSUBARU, electrons are injected from a linear accelerator into a storage ring and undergo a top-up operation at the nominal energy 974 MeV. The storage electrons can be either accelerated up to 1.5 GeV or decelerated down to 0.5 GeV. Recently, a new γ -ray experimental hut, GACKO (Gamma Collaboration Hutch of Konan University), was built at NewSUBARU-BL01 and has become fully operational. Quasi-monochromatic γ -ray beams can be produced in the energy range 1 - 76 MeV by the laser Compton scattering. The capability of tuning the electron beam energy between 0.5 GeV and 1.5 GeV is important to nuclear physicists who use the laser Compton scattering (LCS) γ -ray beams [1, 2]. However, the nominal energy of electrons is determined only with 1% uncertainty based on the beam optics of the storage ring [3].

We calibrated the electron beam energy by producing low-energy LCS γ -ray beams with a CO₂ laser, where γ -ray energies are in the range of the standard γ -ray sources. This report presents the energy calibration for electron beams stored in a storage ring NewSUBARU at nominal energies between 550 MeV and 974 MeV. The absolute calibration of the electron beam offers an opportunity to calibrate the energy of LCS γ -ray beams.

Experiments and Results

Low-energy LCS γ -ray beams were produced below 2 MeV with a grating-fixed CO₂ laser (wave length $\lambda=10.59 \mu\text{m}$). Electrons were injected from a linear accelerator into the NewSUBARU storage ring at the nominal energy 974 MeV, decelerated to 950 MeV, and subsequently down to 550 MeV in steps of 50 MeV. The LCS γ -ray beams were measured with a coaxial (64 mm in diameter \times 60 mm in length) high-purity germanium detector (HPGe). The energy of γ -ray spectra was calibrated with the standard γ -ray sources, ⁶⁰Co including the sum peak, ¹³³Ba, ¹³⁷Cs, and ¹⁵²Eu and a natural radioactivity ⁴⁰K. The energy calibration was carried out before and after the measurement of LCS γ -rays. From the calibrated γ -ray spectra, we determined absolute values of the electron beam energies by means of Monte Carlo simulations in a nominal energy (E_e^n) range 550 – 974 MeV.

Figure 1 shows results of the energy calibration for the HPGe detector carried out before the measurement of LCS γ -ray beam. The best linear fit to the data gives a relation between the γ -ray energy E_γ in keV and the channel number X by $E_\gamma = 0.3624X - 0.8022$. The data taken after the LCS γ -ray measurement gives the same slope coefficient and an intercept -0.7458. The uncertainty of the energy calibration is 0.08% in 1σ in the energy range 120 keV – 2.5 MeV. The electron beam energy was determined by Monte Carlo simulations that best reproduce the experimental γ -ray spectra measured with the HPGe detector. The simulation code incorporates the production process of γ rays in the inverse Compton scattering into the EGS4 code [4] which simulates interactions of photons with the detector material.

The energy of the LCS γ rays is given by

$$E_\gamma = \frac{4\gamma^2 \varepsilon_L}{1 + \gamma^2 \theta^2 + 4\gamma \varepsilon_L / (mc^2)} \quad (1)$$

where ε_L is the energy of a laser photon, mc^2 is the rest-mass energy of an electron, θ is the scattering angle of the laser photon with respect to the electron beam, and γ is the Lorentz factor of the relativistic electron which is defined by $\gamma = E_e / mc^2$ with the total electron energy E_e . For simplicity, the collision

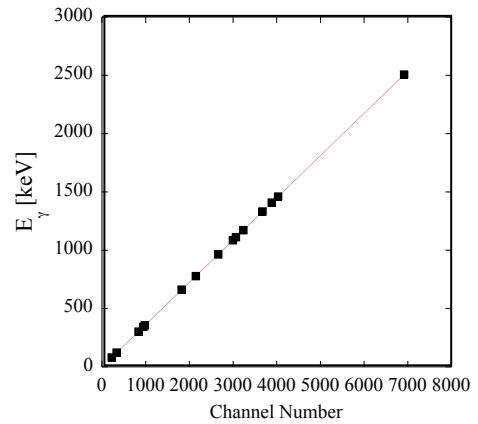


FIG. 1. Energy calibration of the HPGe detector with the standard γ -ray sources. The solid line is the best linear fit to the data.

between laser photons and electrons is assumed to take place at a point where the electron beam forms a narrow waist in the beam optics. The collision point with a maximum collision efficiency is located at a distance of 887cm for the CO₂ laser ($\lambda=10.59 \mu\text{m}$) photons from a collimator and at 1847 cm for the Nd:YVO₄ laser ($\lambda=1064 \text{ nm}$) photons [2]. The electron beam size, which is smaller than the photon beam size at the collision point, determines the size of a light source that emits γ rays inside a solid angle subtended by a 2 mm (in diameter) collimator made of 10 cm thick Pb. We introduce an effective source size in circular shape. The electron beam spot is circular at the collision point for 10.59 μm photons of the CO₂ laser but is elliptic for 1064 nm photons of the Nd:YVO₄ laser [2].

Monte Carlo simulations were carried out to reproduce the experimental γ -ray spectra with two fitting parameters, the effective source size (ζ) and the electron beam energy. It is to be noted that the energy resolution of the HPGe detector was taken into account as an energy spread of the electron beam in the Monte Carlo simulations. The energy resolution of the HPGe detector was 6.7 keV (0.5%) in full width at half maximum (FWHM) for 1332 keV γ rays (60Co). Following the relation $(\Delta E_\gamma/E_\gamma) \approx 2(\Delta E_e/E_e)$ based on Eq. (1), the detector resolution was incorporated into the simulation as $(\Delta E_e/E_e) \approx 0.1\%$ in the standard deviation of Gaussian function. Examples of the best fits to the spectra are shown in Fig. 2. The full energy peaks were well reproduced by the Monte Carlo simulations with the effective source size $\zeta=0.9 - 1.1 \text{ mm}$. The uncertainty in γ -ray

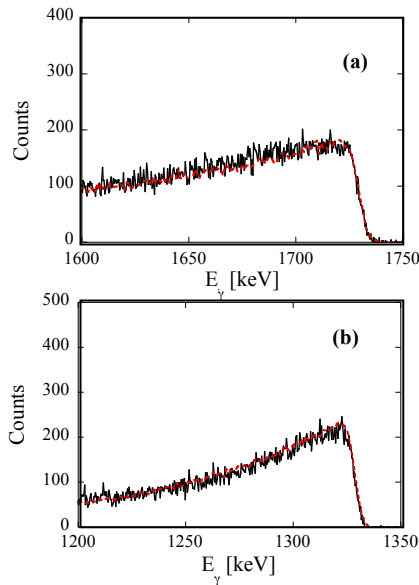


FIG. 2. (a) Monte Carlo simulation (dotted line) with an electron beam energy $E_e^r=982.2 \text{ MeV}$ for LCS γ -ray spectra produced with a CO₂ laser in comparison with the experimental data (solid line) taken at the nominal energy $E_e^n=974 \text{ MeV}$. (b) The same as (a), but for a simulation with $E_e^r=860.7 \text{ MeV}$ in comparison with the data at $E_e^n=850 \text{ MeV}$.

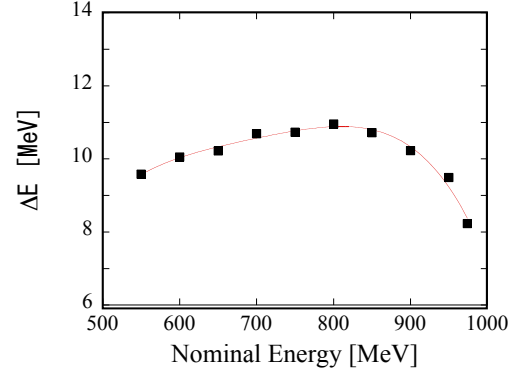


FIG. 3. The difference ΔE of the real energy E_e^r from the nominal energy E_e^n of the electron beams: $\Delta E = E_e^r - E_e^n$. The solid line is the 4th-order polynomial fit to the data. See text for details.

energy associated with the simulation was 0.1%. Together with the 0.08% uncertainty arising from the energy calibration, the γ -ray energy was determined with 0.128% uncertainty, which corresponds to 0.064% uncertainty in electron beam energy.

Figure 3 shows $\Delta E = E_e^r - E_e^n$, the difference of the real energy E_e^r of the electron beams thus determined by the Monte Carlo simulation from the nominal energy E_e^n as a function of E_e^n . The 4th-order polynomial fit to the data gives

$$\Delta E = -4.695 \times 10^{-10}(E_e^n)^4 + 1.302 \times 10^{-6}(E_e^n)^3 - 1.360 \times 10^{-3}(E_e^n)^2 + 0.6385(E_e^n) - 103.94 \quad (2)$$

Here ΔE and E_e^n are given in MeV.

An attempt was made of experimentally detecting the neutron threshold for Au located at 8.072 MeV [5]. A disk of 2mm-thick Au was irradiated with the LCS γ -ray beams produced with the Nd:YVO₄ laser at the nominal electron-beam energies from 677 to 661 in steps of 2 MeV. By changing the electron-beam energy by 2 MeV, we changed the γ -ray energy by $\sim 50 \text{ keV}$. Neutrons were detected with a 4π triple-ring neutron detector [6]. Statistically significant events were observed above 667 MeV followed by no net counts at the three lowest energies, 665, 663, and 661 MeV. In view of the fact that the LCS γ -rays at the threshold energy for Au are produced by 676.52 MeV electrons, the nominal energy of 667 (665) MeV is, in reality, larger (smaller) than 676.52 MeV. Thus, the result of the experimental detection of the neutron threshold for Au is consistent with the present energy calibration.

References

- [1] S. Amano et al., Nucl. Instr. Meth. A 602, 337 (2009).
- [2] K. Horikawa, S. Miyamoto, S. Amano, and T. Mochizuki, Nucl. Instr. Meth. A 618, 209(2010).
- [3] A. Ando et al., J. Synchrotron Rad. 5, 342 (1998).
- [4] W.R. Nelson, H. Hirayama and W.O. Roger, "The EGS4 Code Systems", SLAC-Report-265 (1985).
- [5] G. Audi, A.H. Wapstra and C. Thibault, Nucl. Phys. A 729, 337 (2003).
- [6] A. Makinaga, H. Utsunomiya et al., Phys. Rev. C 79, 025801 (2009).

NEXAFS Study on Hyperthermal Atomic Oxygen Beam Irradiation Effect on the Ti-containing DLC Film

Kazuhiro KANDA¹, Kengo KIDENA¹, Kazuhiro FUKUDA¹, Ryo IMAI¹, Masahito NIIBE¹,
Synya FUJIMOTO², Kumiko YOKOTA², Masahito TAGAWA²

¹*Laboratory of Advanced Science and Technology for Industry, University of Hyogo, Japan,*

²*Faculty of Engineering, Kobe University, Japan*

Abstract

Surface structural changes of Ti-doped diamond-like carbon (Ti-DLC) film exposed to a hyperthermal atomic oxygen beam were investigated using near-edge X-ray absorption fine structure (NEXAFS) spectroscopy using synchrotron radiation. The spectral shape of the C *K* NEXAFS spectrum of as-deposited Ti-DLC film resembled that of DLC film. After exposure to atomic oxygen, the spectrum resembled that of TiC powder. On the other hand, the spectral shape in the Ti *L* NEXAFS spectrum of as-deposited Ti-DLC film resembled that of TiC powder and became similar to that of TiO₂ powder after exposure to atomic oxygen. These changes are ascribable to the desorption of C atoms as CO and/or CO₂ from Ti-DLC film due to the irradiation of atomic oxygen beam.

Introduction

Diamond-like carbon (DLC) films were expected to be used as lubrication materials in space, where oil cannot be used, because they exhibit excellent friction properties both in a vacuum and in air. One of the most important concerns is the reliability of DLC films as a lubricating material in an extreme space environment (temperature, soft X-ray, radiation of atomic oxygen, and their synergistic conditions). The most important factor in causing deterioration of the material in low Earth orbit (LEO), where artificial satellites and spacecraft are positioned, is atomic oxygen exposure. In this orbit, artificial satellites and spacecraft are exposed to atomic oxygen with a translation energy of 5 eV. In our previous study, we investigated the effects of atomic oxygen exposure with an impinging energy of 5 eV on the surface chemistry and structure of DLC film surfaces by using an atomic oxygen beam source [1]. A departure of hydrogen from DLC films and structural change of carbon atom in the surface layer of a hydrogenated DLC film were verified during hyperthermal atomic oxygen exposure.

Recently, the development of functional DLC films advanced due to the incorporation of other elements, such as N, Si, F, and metal content, into DLC films to enhance their electrical, optical, and mechanical properties. In particular, Ti-doped DLC films have been widely investigated due to their thermal stability. In the present study, we investigated the effect of atomic oxygen exposure with an impinging energy of 5 eV on the surface chemistry and structure of Ti-DLC films by measuring the near-edge X-ray absorption fine structure (NEXAFS) spectra.

Experimental methods

The Ti-containing hydrogenated DLC (Ti-DLC) films used in this study are commercially available. The films were deposited at 200 nm thickness on Si wafers by using an amplitude modulated RF plasma-enhanced chemical vapor deposition (CVD) method. The hydrogen content of these films were estimated to be greater than 40 at.% using the combination of Rutherford backscattering spectrometry (RBS) and elastic recoil detection analysis (ERDA) of DLC films by using the same synthesis method.

The exposure of an atomic oxygen beam into the Ti-DLC films was done using a laser detonation-type beam apparatus located at the Kobe Univ. The translational energy of atomic oxygen was estimated to be 5.46 eV by using a time-of-flight (TOF) measurement system consisting of a quadrupole mass spectrometer with a scintillation detector and a multichannel scalar. The typical atomic oxygen flux at the sample position (46 cm from the nozzle) was estimated to be 3.51×10^{15} atoms cm⁻² s⁻¹ by using a Ag-coated quartz crystal microbalance (QCM). In the present study, four sheets of Ti-DLC film were exposed to an atomic oxygen beam corresponding to the fluences of 2.74×10^{19} , 5.47×10^{19} , 8.3×10^{19} , and 1.85×10^{20} atoms cm⁻², respectively. All exposure experiments were carried out at room temperature.

The NEXAFS measurements were carried out on beamline 09A (BL09A). Undulator light dispersed by a invalid spacing planer-grating monochromator was irradiated on the sample film at 54.7° (magic angle) with respect to the surface normal of the samples. The NEXAFS spectra were measured in the total electron yield mode. The measured energy range of the C *K* edge absorption and Ti *L* edge absorption were 275–330 eV and 450–500 eV, respectively.

Results and Discussion

Figure 1 shows the C *K*-edge NEXAFS spectra of a Ti-DLC film exposed to by an atomic oxygen beam with that of a Ti-DLC film before exposure. The spectral features of the C *K* NEXAFS spectrum of the Ti-DLC film before exposure resembled that of the DLC film. By the exposure to an atomic oxygen beam, the spectral features of the C *K* NEXAFS spectrum of the Ti-DLC film noticeably changed. 1) A sharp peak was observed at 289 eV due to the increase in intensity at which a peak was observed as a small shoulder peak in the spectrum of the Ti-DLC film before exposure. 2) The intensity of the peak at 285.4 eV decreased. This decrease indicates that the sp^2 component decreased in the Ti-DLC film. The spectral features of the Ti-DLC film after exposure to atomic oxygen beam resembled that of TiC powder. In addition, the peak at 289 eV was assignable to the $1s \rightarrow \sigma^*$ transition originating from the C atoms neighboring the Ti atoms.

Figure 2 shows the Ti *L*-edge NEXAFS spectra of the Ti-DLC exposed to an atomic oxygen beam with that of the Ti-DLC film before exposure. The spectral features of the Ti *L* NEXAFS spectrum of the Ti-DLC film before exposure resembled that of TiC powder. After exposure to an atomic oxygen beam, the spectral features of the Ti-DLC films changed and became similar to those of TiO₂ powder.

From these results, the changes in the local structure of the Ti-DLC film due to exposure to an atomic oxygen beam are summarized as follows: 1) In the as-deposited Ti-DLC films, almost all the C atoms were bonded to each other with single bonding and double bonding at a certain ratio. Most of the Ti atoms bonded to the C atoms. 2) After exposure to an atomic oxygen beam, most of the C atoms bonded to Ti atoms and most of the Ti atoms bonded to the O atoms. These changes are ascribable to the desorption of C atoms from Ti-DLC films due to the irradiation of the atomic oxygen beam. The C atoms were desorbed from the films as gas species (CO and/or CO₂). On the other hand, oxidized Ti (TiO_x) was not desorbed from the Ti-DLC films as a gas species. Therefore, the Ti/C ratio on the surface of the Ti-DLC films increased due to the irradiation of the atomic oxygen beam. As the result, residual C atoms bonded to the Ti atoms. The $sp^2/(sp^2+sp^3)$ ratio of C atoms in the Ti-DLC films exponentially decreased because the C-Ti bonding could not form double bonding. The discrepancy a the previous work on DLC film [1] is ascribable to Ti-DLC films containing Ti atoms, which were not desorbed from the film even if they were oxidized due to the irradiation of an atomic oxygen beam.

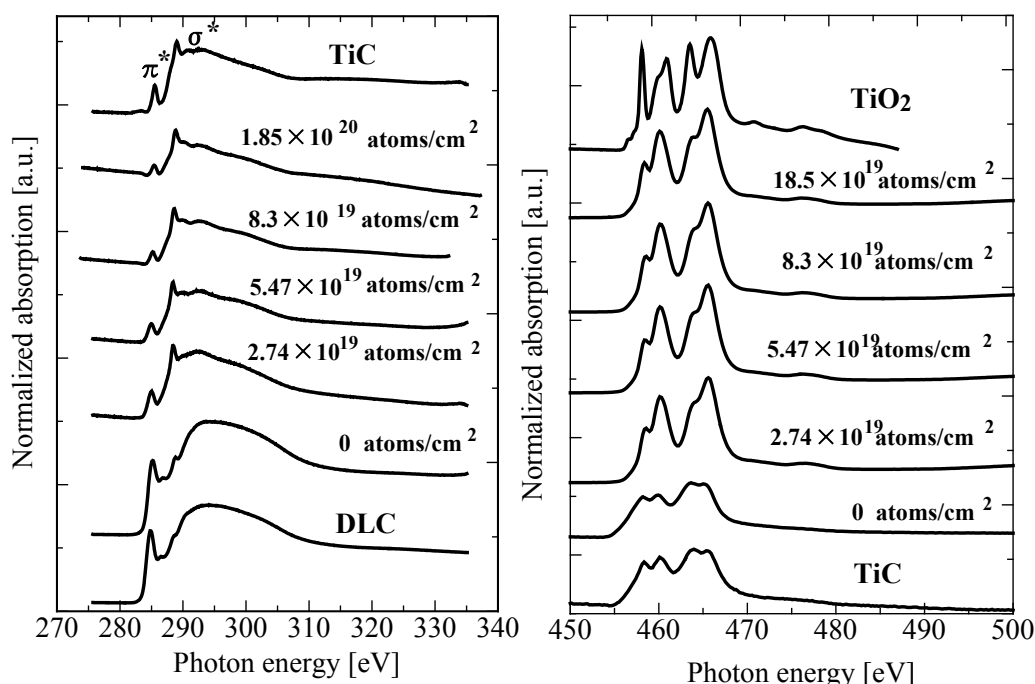


Fig.1 C *K*-edge NEXAFS spectra of commercial DLC film and Ti-DLC films before and after exposure to atomic oxygen beam and TiC powder

Fig.2 Ti *L*-edge NEXAFS spectra of TiC powder, Ti-DLC films before and after exposure to atomic oxygen, and TiO₂ powder.

References

- 1) K. Yokota, M. Tagawa, A. Kitamura, K. Matsumoto, A. Yoshigoe, Y. Teraoka, Appl. Surf. Sci. 255 (2009) 6710.
- 2) M. Tagawa, K. Yokota, A. Kitamura, K. Matsumoto, A. Yoshigoe, Y. Teraoka, K. Kanda, M. Niibe, Applied Surface Science 256 (2010) 7678-7683.

Soft X-ray Irradiation Effect on Highly Hydrogenated Diamond-like Carbon Films

Ryo IMAI¹, Makoto OKADA¹, Shinji MATSUI¹, Tsuneo SUZUKI², Kazuhiro KANDA¹

¹Laboratory of Advanced Science and Technology for Industry, University of Hyogo, Japan,

²Energy-Density Research Institute, Nagaoka University of Technology, Japan

Abstract

Surface and bulk properties' changes of a hydrogenated Diamond-like carbon (H-DLC) film exposed to synchrotron radiation (SR) in the soft X-ray region were investigated by an atomic force microscope (AFM) and a combination of Rutherford Backscattering Spectroscopy (RBS) and Elastic Recoil Detection Analysis (ERDA) techniques. The surface of H-DLC films became flat and the hydrogen content of H-DLC films decreased with increasing SR dose.

Introduction

Diamond-like carbon (DLC) films have excellent properties including high hardness, a low friction coefficient, high abrasion quality, a gas barrier, chemical inertness, and surface lubrication and are therefore being utilized as coating materials on automobile parts, hard disks, artificial blood vessels, edged tools, and food containers. Film-forming methods affect the properties of DLC films differently, and thus a wide variety of DLC films have been developed. DLC films are expected to be used in outer space as a lubrication substitution for oil, which cannot be used in space because it disappears in vacuums [1-2].

DLC films are generally known to be durable against X-ray exposure [3]. However, it has recently been reported that soft X-ray exposure on highly hydrogenated DLC (H-DLC) films leads to desorption of hydrogen and an increase in film density and refractive index [4-5]. A theoretical calculation has suggested that this hydrogen desorption could be associated with a structural change of DLC films [6]. Clarification of the effect of soft X-ray exposure on DLC films is necessary to ensure that DLC films can be used in outer space safely.

In this study, we investigated the modification processes by soft X-ray exposure on H-DLC films. Specifically the SR dose dependence of surface roughness (R_a), and hydrogen content was investigated. The elementary composition analysis was performed using a combination of Rutherford Backscattering Spectroscopy (RBS) and Elastic Recoil Detection Analysis (ERDA) techniques. The surface roughness was measured using an atomic force microscope (AFM).

Experiments

200-nm-thick H-DLC films were deposited on Si wafers by using an amplitude-modulated RF plasma-enhanced CVD method. This method enables the deposition of DLC films containing a lot of hydrogen. The SR irradiation of the H-DLC films was carried out at BL06 of the NewSUBARU synchrotron facility at the University of Hyogo, Japan. The SR at the BL06 sample stage had a continuous spectrum from IR to soft X-rays, lower than 1 keV. This includes 300 eV, which is the ionization energy of a carbon K edge. As a result, the K -shell electrons of the C atoms could be excited by the SR at BL06. During this experiment, the electron energy of the NewSUBARU ring was 1.0 GeV. The BL06 sample stage was room temperature and the pressure in the chamber was the order of 10^{-5} Pa. An SR dose [$\text{mA}\cdot\text{h}$] is derived from the product of the ring current [mA] and exposure time [h]. The exposure on the H-DLC films was carried out over SR doses ranging from 0 to 3000 $\text{mA}\cdot\text{h}$.

Results and discussion

The hydrogen content of H-DLC films was quantitatively determined by RBS/ERDA. The measurements were performed using an electrostatic accelerator (Nissin High Voltage, NT-1700HS) located at the Extreme Energy-Density Research Institute, Nagaoka University of Technology, Japan. He^+ ions accelerated to 2.5 MeV using a tandem Pelletron accelerator were used as the incident beam, whose angle with respect to the surface normal was 72° . The measurement error of this apparatus is 1%.

Figure 1 shows the SR dose dependence of the hydrogen content of H-DLC films. The hydrogen content of the unirradiated H-DLC films was $\approx 50\%$. After SR exposure, the hydrogen content drastically decreased in the range of 0–200 $\text{mA}\cdot\text{h}$, eventually becoming $\approx 30\%$ at 200 $\text{mA}\cdot\text{h}$. Above $\approx 200 \text{ mA}\cdot\text{h}$, the hydrogen content slowly decreased and consequently became $\approx 20\%$. This result shows that the SR exposure on H-DLC films leads to hydrogen desorption. However, hydrogen of $\approx 20\%$ in H-DLC films had no influence due to SR exposure. This indicates that hydrogen atoms exist at different chemical environments in H-DLC films: where hydrogen emitted or not emitted from films by the exposure to soft X-rays. It has previously been found that the structure of H-DLC films varied to that of typical DLC films whose hydrogen content is

20–30 % by the exposure to soft X-rays [5].

The surface roughness of the H-DLC films were measured by using a tapping method with AFM apparatus (SII nanotechnology E-sweep/nanoNavi Station); the determining area was 1000×1000 nm. SR dose dependence of R_a estimated by the measurements of AFM, are shown in Fig. 2. The R_a of the unirradiated H-DLC films was 0.29 nm, which was the largest. The R_a of H-DLC films with even smallest SR dose (10 mA·h) rapidly decreased compared to the unirradiated one. In addition, R_a remained approximately constant at ≈ 0.18 nm in regions above ≈ 100 mA·h. These results show that SR exposure on H-DLC films led to a decrease of R_a , and it also flattened the surface of the H-DLC films. In terms of the hydrogen content, the change was observed in ≈ 0 –200 mA·h. In contrast, the process of flattening decreased at a lower SR dose. Therefore, the process of surface flattening differs from that of hydrogen desorption.

The modification of H-DLC films by the SR exposure includes hydrogen desorption and surface flattening. Immediately after the SR exposure, the surface becomes flat due to desorption from the salient. Up to ≈ 200 mA·h, the hydrogen content of the H-DLC films was ≈ 30 %.

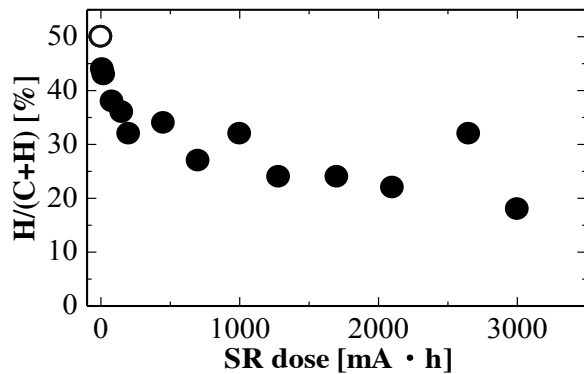


Fig. 1. SR dose dependence of hydrogen content of H-DLC films.

○ and ● represent unirradiated and irradiated, respectively.

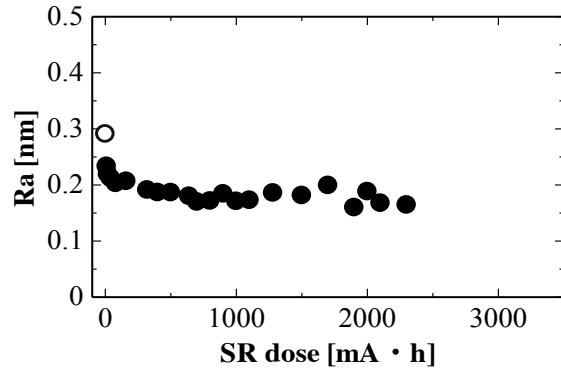


Fig. 2. SR dose dependence of surface roughness of H-DLC films.

○ and ● represent unirradiated and irradiated, respectively.

Conclusions

Soft X-ray irradiation effect on the surface and material properties of highly hydrogenated Diamond-like carbon thin films was investigated using an atomic force microscope (AFM) and a combination of Rutherford Backscattering Spectroscopy (RBS) and Elastic Recoil Detection Analysis (ERDA) techniques. The hydrogen content of H-DLC films decreased from ≈ 50 % to ≈ 20 % by the SR exposure on films. Hydrogen desorption was not observed at higher doses. In the range of ≈ 0 –200 mA·h, hydrogen content decreased. In contrast, the surface roughness (R_a) of the H-DLC films decreased at lower SR doses compared with hydrogen content, and the surface of the H-DLC films became flat. We found that the modification processes of H-DLC films by SR exposure include hydrogen desorption and flattening on the surface.

References

- [1] C. Donnet *et al.*, Tribology of Diamond-like Carbon, Springer (2008).
- [2] C. Donnet *et al.*, Surf. Coat. Technol. 68-69 (1994) 626.
- [3] H. Kyuragi *et al.*, Appl. Phys. Lett. 50 (1987) 1254.
- [4] K. Kanda *et al.*, Jpn. J. Appl. Phys. 50 (2011) 055801.
- [5] H. Matsuura *et al.*, SEI Tech. Rev. 171 (2007) 36 [in Japanese]
- [6] Y. Miura *et al.*, J. Appl. Phys. 93 (2003) 3395.

Low-Temperature Activation of Boron in Si wafer by Soft X-ray Irradiation

Akira Heya¹, Takuto Fukuoka¹, Naoto Matsuo¹, Kazuhiro Kanda², and Takashi Noguchi³

¹ University of Hyogo, 2167 Shosha, Himeji, Hyogo 671-2280, Japan

Phone: +81-79-267-4909 E-mail: heyaa@eng.u-hyogo.ac.jp

² LASTI, University of Hyogo, 3-1-2 Koto, Kamigori, Hyogo 678-1205, Japan

³ University of the Ryukyus 1, Senbaru, Nishihara, Okinawa, 903-0213, Japan

Abstract

Novel activation method of B dopant using a soft X-ray undulator was investigated. The activation energy of B activation by soft X-ray irradiation was lower than that of B activation by an annealing. As the irradiated photon energy closed with the core level of Si 2p, the activation ratio increased. This related to the enhancement of electron excitation as a base on Fermi golden rule. At low temperature, the B activation occurred by the atomic migration of Si atoms due to Coulomb force via the electron excitation.

Introduction

Fabrication method of an ultra-shallow junction lower than 10 nm is required. We proposed a novel activation method of B dopant at low temperature by using a soft X-ray undulator [1]. The photon energy dependence of sheet resistance was investigated. In addition, the mechanism of soft X-ray activation was discussed in comparison with a conventional thermal activation.

Experimental

B ions were implanted to Si (100) wafer (n-type, 8-12 Ωcm) with an energy of 5 keV and a dose quantity of $2 \times 10^{15} \text{ cm}^{-2}$. The irradiation of soft X-ray was carried out at BL07A of NewSUBARU[1]. The photon energy was changed from 50 to 250 eV, with the dose quantity of 50 mA h. In addition, to reduce the sample temperature, the storage-ring current decreased from 250 to 50 mA. The gas pressure during irradiation was $6 \times 10^{-5} \text{ Pa}$. The surface temperature of Si substrate during soft X-ray irradiation was measured by thermocouple and via a ZnSe window by a thermo-viewer. For the comparison, the annealing in N_2 atmosphere was carried out in the range of 100 to 1000°C.

The sheet resistance was measured by a four-point probe method at room temperature. The activation ratio is given by Irvin curve and dopant dose quantity. Activation energy of B activation (E_a) was estimated by Arrhenius plot of activation ratio.

Results and discussion

The sheet resistance and the temperature of Si wafer as a function of photon energy are shown in Fig. 1. The temperature at the photon energy of 100 eV, which corresponds to the energy level of Si 2p core-electron (99.8 eV), shows the highest value. The Si 2p core-electrons of Si atom are excited by soft X-ray irradiation and they relax resulting in a temperature increase of Si wafer. The activation was enhanced at 100 eV. According to Fermi golden rule, the electron excitation is enhanced by closing to energy of core level. It is found that the sheet resistance after soft X-ray irradiation strongly depended on the irradiated photon energy.

As the storage ring current decreased, the sample temperature decreased to 110°C and the sheet resistance was increased to 3.1 $\text{k}\Omega/\square$ (Fig. 2). The sheet resistance of annealed sample at 100°C was 8.0 $\text{k}\Omega/\square$. It shows that the activation was enhanced by the electron excitation during the soft X-ray irradiation.

The relationship between the activation ratio and the reciprocal absolute temperature are shown in Fig. 3. The sheet resistance of soft X-ray irradiated Si was lower than that of annealed Si below 400°C. The E_a for the soft X-ray activation was smaller than that for the annealing. The discrepancy of E_a between the soft X-ray irradiation and annealing indicates that the soft X-ray activation occurred by not only the thermal effect but also the excitation of the core electrons followed by the atomic migration.

The activation mechanism of B by soft X-ray irradiation is considered as follows (Fig. 4). The activation by annealing generally occurs by movement of dopant atoms to lattice sites of Si. This process corresponds to the Arrhenius plot for thermal annealing in high temperature range. The soft X-ray irradiation enhances the atomic

migration via excitation of Si2p core-electrons of Si. During the recovery of crystallinity in amorphized Si surface by atomic migration via electron excitation, B atom can shift to the lattice site of Si atom. Because the size of B atoms is smaller than that of Si atom, the B activation is influenced by atomic migration of Si such as “knock-on” effect.

Conclusions

1) The activation of B dopant occurs at 110°C, although the activation ratio shows small value of 6.2×10^{-3} . The B activation ratio of Si wafer subjected to photon with an energy of Si2p and B1s were 1.8×10^{-2} and 5.7×10^{-3} , respectively. Because the size of B atoms is smaller than that of Si atom, the enhancement of Si migration by soft X-ray irradiation triggers the movement of B atoms.

2) The B activation energy for the soft X-ray irradiation was smaller than that for the annealing. The soft X-ray activation occurred by not only the thermal effect but also the excitation of the core electrons followed by the atomic migration.

References

- [1] A. Heya, K. Kanda, K. Toko, T. Sadoh, S. Amano, N. Matsuo, S. Miyamoto, M. Miyao, and T. Mochizuki: Thin Solid Films 534 (2013) 334.

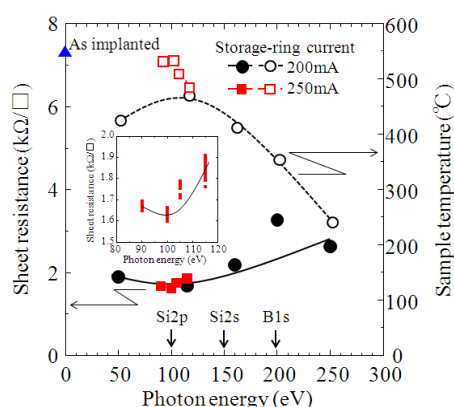


Fig. 1. Sheet resistance (closed symbol) and temperature of Si wafer (open symbol) as a function of photon energy of soft X-ray. The insert shows the sheet resistance of Si wafer for the photon energy from 90 to 115 eV.

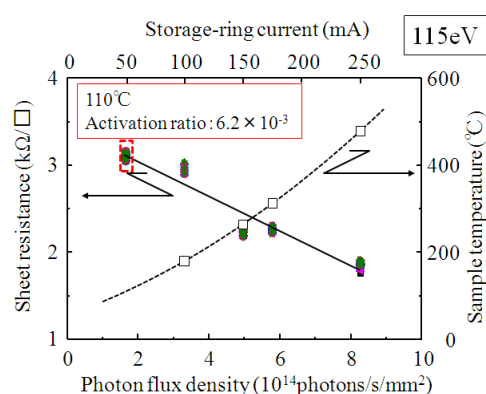


Fig. 2. Sheet resistance and sample temperature as a function of photon flux density (storage-ring current) at photon energy of 115 eV. The B activation occurs at 110°C, although the activation ratio shows small value of 6.2×10^{-3} .

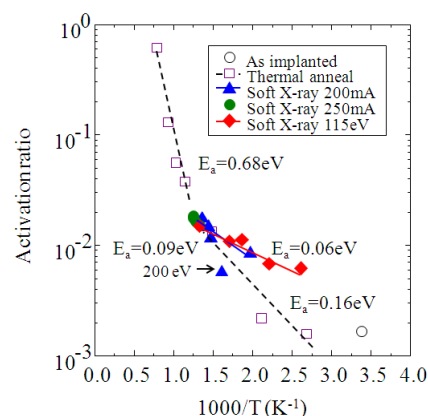


Fig. 3. Relationship between the activation ratio and reciprocal absolute temperature. Activation energy of B dopant activation was estimated from the slope. The E_a for the soft X-ray activation (0.06 and 0.09 eV) was smaller than that for the annealing (0.16 eV).

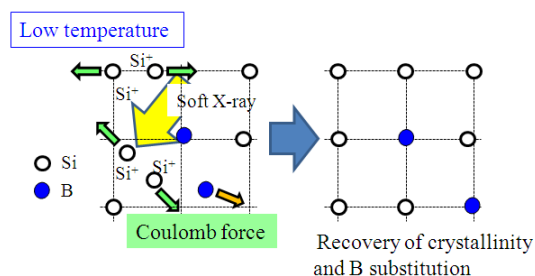


Fig. 4. Schematic diagram of mechanism of low-temperature activation by soft X-ray irradiation. The soft X-ray irradiation enhances the atomic migration via excitation of Si2p core-electron. During the recovery of crystallinity in amorphized Si surface by the atomic migration via the electron excitation, B atom can shift to the lattice site of Si atom.

Surface Modification in Silica-Based Films by Undulator Radiation

K. Moriwaki, S.Takezawa, Graduate School of Eng./ Kobe Univ.,
K.Kanda, and S.Matsui, LASTI/Univ. Hyogo

Abstract

Undulator radiation (UR) by the NewSUBARU is used to modify the surface in pure silica and GeO₂-doped silica films for optical waveguide devices. Irradiated films are found to show reduction for both SiO₂ and GeO₂ bonds by analyzing XPS (X-ray Photoelectron Spectroscopy) results. The surface reduction results generating Si-Si bonds show a clear peak-energy-dependence of UR, in which there is a threshold energy near the L₃ absorption-edge for Si. The surface reduction layer for Si-Si bonds is found to be very thin less than 1.5nm, while that for Ge-Ge bonds is less than 40nm.

Introduction

We use synchrotron radiation (SR) and undulator radiation (UR) for photo-induced refractive-index modifications in silica-based glasses for optical waveguide devices^{1,2)}. Our main objectives are to induce large refractive-index changes more effectively using SR or UR without a spectrometer, and to investigate their origins depending on wavelengths of SR or UR spectra. Especially, UR would be a very useful tool for the materials modifications, because it can select a useful wavelength and it has very high intensity. For those reasons we mainly use UR for the materials modifications. In this report, we investigated the modification effects on the surface of SiO₂ films or GeO₂ doped SiO₂ films irradiated with UR. XPS was mainly used for the characterizations.

Experiments and Results

Experimental conditions are almost the same as in the previous experiments^{1,2)}. UR (from the NewSUBARU BL-7A) was mainly used to investigate irradiation-wavelength effects. SR (from the NewSUBARU BL6) was also irradiated on samples directly without a spectrometer. The electron energy of the SR was 1GeV. The UR peak energy in the first order was controlled from 20 to 120 eV. The samples were thermally grown SiO₂ films (0.5 or 1 μ m thickness) on Si substrates and GeO₂-doped SiO₂ films (2 μ m thickness) fabricated by the FHD (Flame Hydrolysis Deposition) technique on Si substrates in this experiments. Relative refractive index difference for the GeO₂-doped SiO₂ films was 1.9%. XPS measurements and the following RIE (Reactive Ion Etching) were used to investigate the surface reduction effects and depth profiles for the modification.

It was shown in Fig.1 that Si-Si bonds were generated on the surface of thermally grown SiO₂ films, after irradiating UR with peak energy values of 20, 60, and 80eV by measuring Si2p peaks in the XPS. On the other hand, after irradiating UR with peak energy values of 100 and 120eV, Si-Si bonds were not generated as shown in Fig.1. It may suggest that the Si-Si bonds generations are influenced by the L₃ absorption at 99.2eV for Si. The modified layer was very shallow, because the generated Si-Si bonds on the surface were disappeared after etching the sample up to a depth of 1.5 nm as shown in Fig.2. The etched sample in Fig.2 shows the same SiO₂ bond peak without a Si-Si bond peak as in the original ones. In GeO₂ doped SiO₂ films irradiated by UR, almost the same tendency were found for the Si-Si bonds generation. The depth profile was also the same as that in the Fig.2

As for the Ge3d peaks in GeO₂ doped SiO₂ films after irradiating UR, the reduction layer with Ge-Ge bonds was also found to be generated especially for

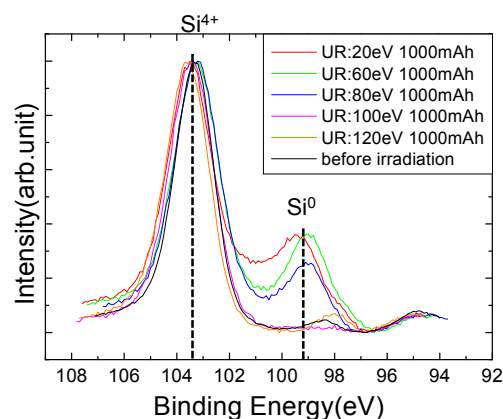


FIG.1. Si2p peaks in the XPS spectra, before and after irradiating UR with peak energy from 50 to 120 eV in pure SiO₂ films. Si-Si bonds are generated for the sample for peak energies less than 100eV. The UR dose was 1000mAh.

low peak energy such as 50 or 60 eV as shown in Fig.3. The Ge-Ge peak decreases gradually by increasing the peak energy of UR. For a sample irradiated with peak energy of 100 or 120eV, peaks for Ge-Ge bonds are not seen in Fig.3, but this might be caused by a weak intensity for the Ge3d peak as compared to that for Si2p. The threshold energy is not clear for the Ge-Ge bonds generation comparing to that for the Si-Si bonds, which may be caused by the absence of clear absorption-edge for Ge around the irradiation energy range. After etching the sample, the reduction layer with Ge-Ge bonds was removed by 40 nm-deep etching. The Ge-Ge bonds layer is generated deeper than that for the Si-Si bonds layer of 1.5nm, which may be a cause of a penetration-depth difference for the effective irradiation wavelength.

The surface reduction effects appeared in Fig.1 was changed by other samples with different film thickness. A sample with thinner film with the same irradiation condition showed more intense peaks for Si-Si bonds in the XPS. Sample temperature might be the origin for the thickness dependence, because the sample temperature might be more than a few hundreds of degrees during the irradiation.

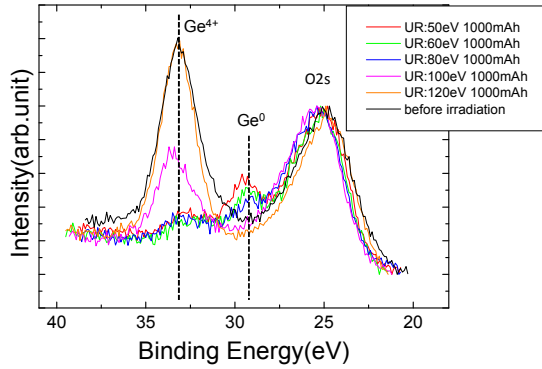


FIG.3. Ge3d peaks in the XPS spectra, before and after irradiating UR with a peak energy from 50 to 120 eV in GeO₂ doped SiO₂ films. Ge-Ge bonds are generated for the sample for peak energies of 50 and 60eV. The peak intensity for the Ge-Ge bonds (Ge⁰) is gradually decreased for peak energy from 80 to 120 eV, The UR dose was 1000mAh.

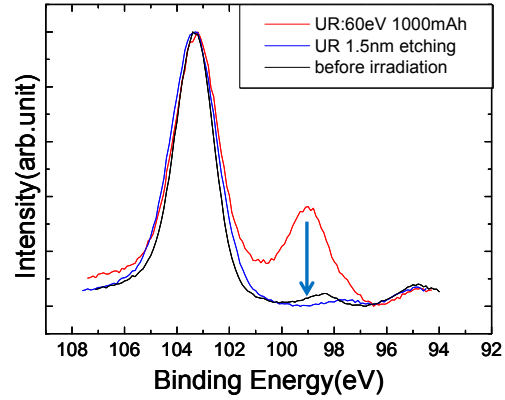


FIG.2. Si2p peaks in the XPS spectra, before, after irradiating UR with a peak energy of 60 eV and after etching up to a depth of 1.5nm in SiO₂ films. The generated Si-Si bonds are disappeared after the etching as in the non-irradiated sample. The UR dose was 1000mAh.

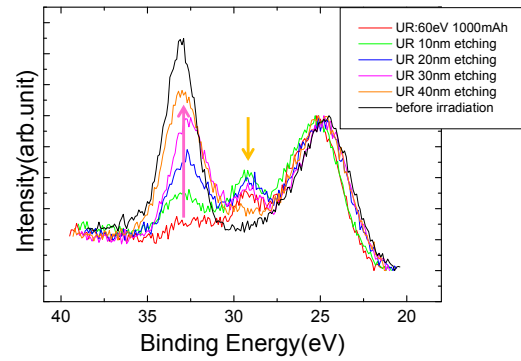


FIG.4. Ge3d peaks in the XPS spectra, before, after irradiating UR with a peak energy of 60 eV and after etching up to a depth of 40nm in GeO₂ doped SiO₂ films. The generated Ge⁰ peaks are disappeared gradually by increasing the etching depth. After 40nm etching, Ge⁰ and Ge⁴⁺ peaks are almost the same as that in the non-irradiated one. The UR dose was 1000mAh.

Conclusions

UR irradiation effects are investigated for an application of silica-based materials to optical waveguide devices. Although large refractive-index changes were obtained by SR and UR irradiation in silica-based films in our previous report¹⁾, other modification effects such as the surface reduction shown here are also important in the applications as an utilization tool and an obstacle for other applications. In our results, it is shown that the surface modification effects for Si and Ge bonds could be controlled by changing the peak energy of UR. From those results, UR is expected to be a useful irradiation source for modifying materials effectively and also controlling the modification effects as a desired way.

References

- [1] K.Moriwaki *et al.*, LASTI Annual Report vol.10 (2008).
- [2] K.Moriwaki *et al.*, LASTI Annual Report vol.13 (2011).

Characterization BN Thin Film Deposited on Cemented Carbide using Soft X-ray Absorption Spectroscopy

Masahito Niibe¹, Takuya Kotaka¹, Satoshi Jinguji², Satoko Hori², and Shozo Inoue²
LASTI¹ & Graduate School of Eng.,² University of Hyogo

Abstract

Crystalline structure of BN thin film deposited on cemented carbide substrate by magnetron sputtering technique was characterized using soft X-ray absorption spectroscopy (XAS). Boron and nitrogen K near edge X-ray absorption fine structures (NEXAFS) of the BN thin films were measured with total electron yield (TEY) method and total fluorescence yield (TFY) method. The film structure changed dramatically from t-BN phase to c-BN phase when film thickness increased from 6.5 nm to 20 nm. The crystalline structure of the film deposited on the WC substrate with a bias voltage of -90 V was still t-BN type. However, the structure changed to c-BN phase when the bias voltage increased to -130 V.

Introduction

As similar to carbon allotropic forms, boron nitride presents a polymorphism of hexagonal structure (h-BN) having a hexagonal plane network; such as graphite, and cubic structure (c-BN) having a steric structure; such as diamond. It is well known that h-BN is a relatively soft material. However, c-BN is known to be the second hardest material after diamond. The preparation of c-BN thin film for a coating material onto cutting tools is extensively studied. In cases of BN thin film fabrication by sputtering or ion plating depositions, h-BN structure is preferentially formed because it is a stable phase at normal pressures. Stably-forming technology for c-BN structured thin film was not confirmed as affairs.

Characterization of crystalline structure of BN thin film is indispensable to confirm the fabrication technology. Near edge X-ray absorption fine structure (XANES) spectroscopy is an appropriate technique to identify the crystal structure of BN thin film because the spectra of c-BN and h-BN are quite distinct and the bonding state on sp^2 and sp^3 can be observed in isolation. In this study, NEXAFS measurement at B-K and N-K edge was carried out for the characterization of crystalline structure of BN thin film deposited on cemented carbide (WC) as well as Si wafer by an RF magnetron sputtering technique.

Experiments

BN thin films were prepared on Si (100) and WC substrates by the RF magnetron sputtering system. The substrate holder was electrically floated for applying a bias voltage and could be heated up to 600°C, simultaneously. Ar+N₂ mixed gas was used as working gas, and its pressure was 0.4 Pa. The DC bias was changed from -80 to -130 V in this study. Atomic composition of the prepared sample was determined by an Auger electron spectroscopy (AES).

B-K and N-K NEXAFS spectra of prepared samples were measured in the analyzing station of the beamline BL9a at the NewSUBARU SR facility. The beamline monochromator was mounted with a plane varied-space grating with central groove density of 1200 l/mm, the energy resolution of which was about 0.2 eV near the photon energy of 400 eV. The measurement was conducted with a total electron yield (TEY) method with sample current mode and with a total fluorescence yield (TFY) method with measuring the amount of fluorescence by a photodiode [1] for the same sample at the same position. It is well known that the TEY method can yield information in a shallow region from the sample surface because of the small escape length of photo-generated electrons of less than about 5nm [1, 2]. Meanwhile, the TFY method can yield information in a deeper region (bulk) of the sample of more than 100 nm [1] because of the much longer penetration depth of soft X-ray photons.

Results and discussion

In order to clarify the growth process of BN films containing the c-BN phase, the films were deposited for 1, 2, 3, 5, and 30 min at 600°C and applied bias voltage of -90 V. Figures 1 and 2 show the B-K and N-K absorption spectra of a prepared films, respectively. The thicknesses of those films were estimated to 6.5, 13, 20, 33, and 200 nm using the deposition rate. For the 6.5-nm-thick film, both B-K edge and N-K edge spectra have a large π^* resonance peaks at 192 eV for B-K and at 401 eV for N-K edges, respectively, which are caused from sp^2 bonding states like a graphite. As the thickness increases to 20 nm, the π^* peak at 401 eV in N-K edge spectra becomes a shoulder. The B-K edge spectrum for the 20-nm-thick film also shows that film has an c-BN-dominant structure in spite of the presence of the small π^* peak. The NEXAFS spectra for the films with the thicknesses of 33 nm and above are almost the same as the spectrum of the 20-nm-thick film. This means that the t-BN (or h-BN with sp^2 bonding) underlayer thickness of the film deposited at 600°C was less than 20

nm and that the c-BN-dominant layer grew from an early stage of the deposition. It was also found from the measurement of incident angle dependency that the t-BN underlayer had a preferential orientation of the c-axis parallel to the film surface. The results also correspond well to the results of infrared absorption spectra measured with FT-IR spectrometer [3].

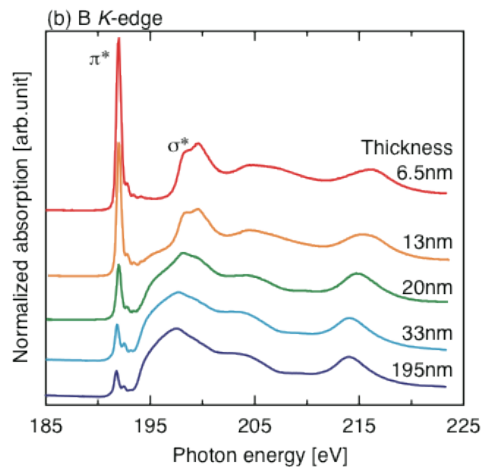


Fig. 1 B-K NEXAFS spectra of BN thin films with various film thicknesses prepared on Si wafer at 600°C.

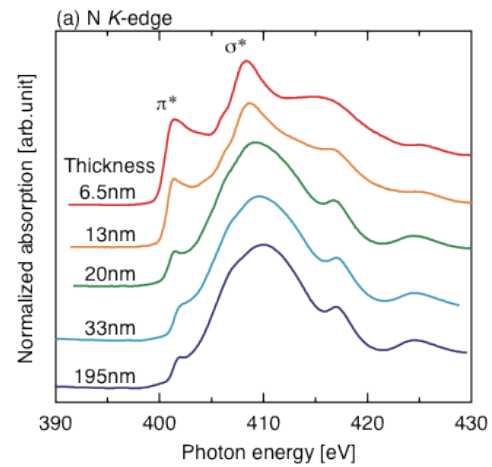


Fig. 2 N-K XANES spectra of BN thin films with various film thicknesses prepared on Si wafer at 600°C.

After the structural investigation on the Si substrate, we deposited BN films onto the Si wafer and the cemented carbide (WC) substrates at the same time with substrate temperature of 600°C. At the negative bias voltage of -90 V, the crystalline structure of the film deposited on the WC substrate was still t-BN phase as shown in Fig. 3, though the structure of film simultaneously deposited on the Si wafer was c-BN phase. N-K NEXAFS spectra at different angles of incidence of 90° and 45° for the prepared BN film are shown in Fig. 3 for TEY and TFY methods. Although, the π^* resonance peak measured by TFY method (bulk) shows a small dependency of incident angle, the angular dependency is very large for the spectra obtained by TEY method (surface). When the negative bias voltage increased to -130 V, the NEXAFS spectrum on WC substrate changed dramatically to c-BN phase as shown in Fig. 4.

It is difficult to evaluate the crystalline structure of BN film deposited on WC substrate by transmission type FT-IR spectroscopy. Therefore, the results obtained in this study suggests the effectiveness of X-ray absorption (NEXAFS) spectroscopy for evaluation of crystalline structure of BN thin films deposited on WC substrates.

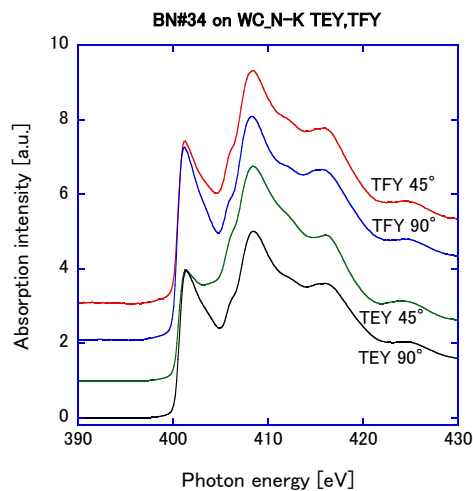


Fig. 3 N-K NEXAFS spectra of the BN thin film prepared on WC substrate with a bias voltage of -90 V.

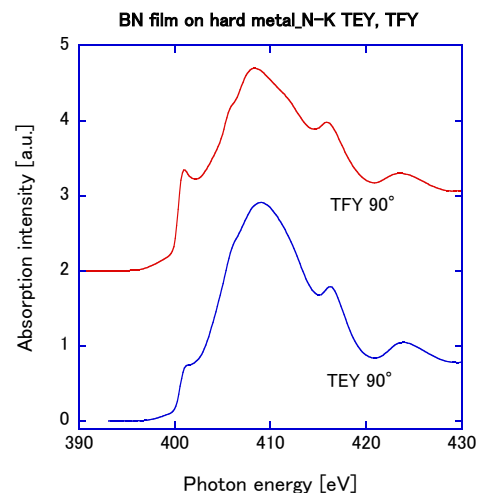


Fig. 4 N-K NEXAFS spectra of the BN thin film prepared on WC substrate with a bias voltage of -130 V.

References

- [1] M.Niibe T. Kotaka, T. Mitamura: J. Phys. Conf. Ser., **425**, 132008, (2013).
- [2] J. Stohr, "NEXAFS Spectroscopy" Springer, Berlin (2003).
- [3] S. Hori, M. Niibe, T. Kotaka, S. Inoue *et al.*, Jpn. J. Appl. Phys., **52**, 045602 (2013).

Spectral Recovery of Etching Damage by Soft X-ray Irradiation Observed in XAS spectra of TiO₂ Thin Film

Keiji Sano¹, Masahito Niibe¹, Takuya Kotaka¹,
Retsuo Kawakami², Kikuo Tominaga², Yoshitaka Nakano³
(Univ. Hyogo¹, Univ. Tokushima², Chubu Univ.³)

Abstract

We analyzed TiO₂ thin films etched with capacitively coupled plasma etching apparatus by near edge X-ray absorption fine structure (NEXAFS) method. As a result, spectral change due to disordering of the crystalline structure was observed by TFY method in the sample treated with higher gas pressure. We also found that Ti-L spectra of etched sample was recovered to as-grown like by irradiation with soft X-rays (496 eV) for 10 min. This recovery occurred not only on the irradiation point of soft X-rays but also on the point 2 mm or more away. Furthermore, it was found that the spectral recovery can also be observed for the surface irradiated with ultraviolet (UV) light instead of soft X-rays.

Introduction

TiO₂ is expected to apply as MOS gate oxide film because of its high dielectric constant. To use TiO₂ as MOS gate film, it has to be processed by etching. However, there are few reports about the effect of etching damage to TiO₂ thin films by etching process. Therefore, we analyzed the effect of etching damage to TiO₂ samples by NEXAFS method. As it happens, we found the phenomenon in the analyzing process that disordered NEXAFS spectra of the etched film recovered to as-grown like by irradiation with soft X-rays.

The purpose of this study is the elucidation of the phenomenon that NEXAFS spectra of etched TiO₂ thin film were recovered by soft X-ray irradiation. We investigated the condition of the etching damage to recover. For example, recovery of the spectra is studied for irradiation condition, light source, and irradiation position.

Experiments

TiO₂ thin films were deposited on a glass substrate (Corning 1737) by facing cathodes DC magnetron sputtering system. We used capacitively coupled plasma (CCP) etching apparatus (Tokushima Univ.) to etch the samples. The etching gas was N₂ and its pressure and etching time were varied from 10 to 100 mTorr and 5 to 200 minutes, respectively. These samples were analyzed by NEXAFS method conducted at BL09A in the NewSUBARU synchrotron radiation facility^[1]. The measurements were carried out with total fluorescence yield (TFY) method (bulk sensitive) and total electron yield (TEY) method (surface sensitive) at the Ti-L_{2,3} edges (443 ~ 496 eV)^[2]. NEXAFS method can obtain the information of chemical state or local structure around the element selectively by measuring an absorption edge of any element in the sample in non-destructive.

Results

As shown in Fig.1 (a), the spectra measured by TFY method was changed that the peak near 467 eV became lower with increasing the etching gas pressure. However, as shown in Fig.1 (b), there was little change due to increase of the gas pressure in the spectra by TEY method. Therefore, we got a very strange result that the etching damage of the sample surface was small but the damage at the sample inside was larger.

Continuing the measurement in order to investigate the cause, we found that the spectra of the etched sample were recovered to as-grown like by soft X-ray irradiation. Fig.2 shows the recovery process of the NEXAFS spectra by soft X-ray irradiation measured with TFY method. The etching gas pressure of the sample was 100 mTorr, and the etching time was 60 minutes. The spectrum of etched sample became as-grown like by soft X-ray irradiation (496 eV, tens of mW/cm²) for 30 minutes. After the irradiation, the spectra of recovered samples were returned to disordered shape by exposure to air, and then measured again after 21 days later. After returning to disordered shape by air exposure, the sample spectrum changed to as-grown like again by re-irradiation with soft X-rays for 10 minutes.

The bonding orbital around the Ti atoms should be disturbed by generation of oxygen vacancies. The spectra should be disturbed by disarray of crystalline structure. Therefore, it was considered that the spectra were recovered by supplement of the defective part. Since the spectral recovery by soft X-ray irradiation returned to that of after etching by exposure to the air, we considered that the spectrum recovered apparently by electrons which are from the electron-hole pairs generated by light irradiation and are trapped at the oxygen vacancies.

Etched Sample was irradiated with soft X-rays for 25 minutes at the center position of the sample in order to find out whether NEXAFS spectrum was recovered as spatially distributed. After irradiation, the sample was measured at the position separated from 2 mm above and below the irradiation center. soft X-rays were not irradiated at the position separated 2 mm from the center because the beam size of irradiated soft X-rays in

BL09A is $0.8 \text{ mmH} \times 0.3 \text{ mmV}$. However, the spectrum was recovered as-grown like not only at the center position of the sample but also the position separated 2 mm above and below from the center. We consider that recovery of spectrum was observed at the position outside of the irradiation due to the diffusion of generated excitons to the periphery of the irradiation position as free excitons.

If the fact of spectral recovery is caused by excitons generated by soft X-ray irradiation, it is considered that the spectra should be recovered by UV irradiation instead of the soft X-rays, the energy of which is above the band gap energy of anatase TiO_2 (3.2 eV). Therefore, we tried to irradiate UV light (3.4 eV, 49 mW/cm^2) to the etched sample (CCP- N_2 , 100 mTorr, 60 min) in vacuum. Fig.3 shows the recovery process of the NEXAFS spectra by UV irradiation measured with TFY method. The spectrum of etched sample was recovered to as-grown like by UV irradiation. From the results above, it was considered that the spectral recovery of the etched sample should be apparent recovery due to the electrons generated by soft X-ray irradiation and trapped in the oxygen vacancies.

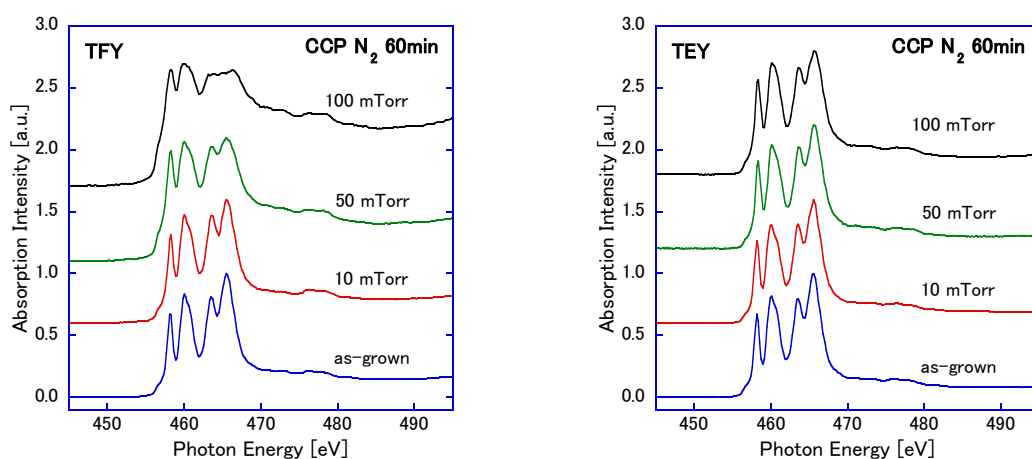


Fig.1 $\text{Ti-L}_{2,3}$ NEXAFS spectra of etched TiO_2 thin films
(a): TFY method and (b): TEY method.

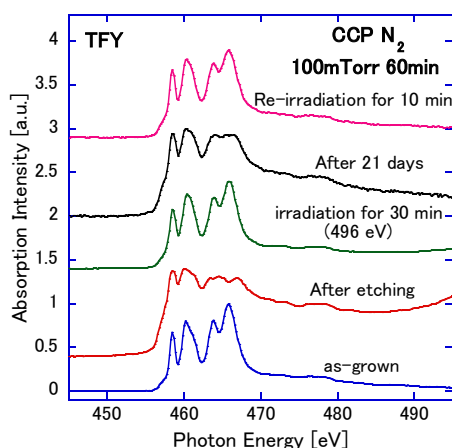


Fig.2 Recovery of Etching Damage by Soft X-ray Irradiation.

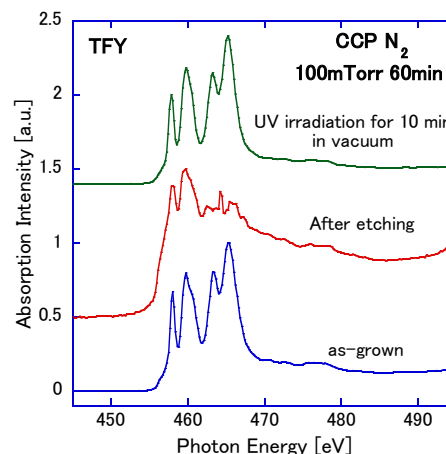


Fig.3 Recovery of Etching Damage by UV Irradiation.

References

- [1] M.Niibe et al.: AIP Conf. Proc. No. **705** (AIP, New York, 2004), p.576
- [2] T.Kotaka and M.Niibe: Adv. X-ray Chem. Analysis, **43** (2012) 175.

Modification of Electronic States of Multi-layer Graphenes by Ion Irradiation

S. Honda^{1,7}, A. Tsukagoshi^{1,7}, R. Osugi^{1,7}, M. Niibe², and M. Terasawa^{2,7}

¹Univ. of Hyogo, ²LASTI Univ. of Hyogo

R. Hirase³, H. Yoshioka³, and H. Izumi³

³Hyogo Pref. Inst. of Tech.

K.-Y. Lee⁴

⁴National Taiwan Univ. of Sci. and Tech.

K. Niwase⁵

⁵Hyogo Univ. of Teacher Education

E. Taguchi⁶

⁶Research Center for Ultra-High Voltage Electron Microscopy, Osaka Univ.

M. Oura⁷

⁷RIKEN SPring-8 Center

Abstract

Low energy Ar ions (0.5 - 2 keV) were irradiated to multi-layer graphene films and the local electronic states were investigated by x-ray absorption spectroscopy (XAS). XAS analysis indicated that the number of sp^2 -hybridized carbon (sp^2 -C) atoms decreased after ion irradiation. At the same time, sp^3 -hybridized carbon (sp^3 -C) atoms were suggested to be formed in the multi-layer graphenes.

Introduction

Graphenes [1] have been attracting tremendous attention as new semiconductors because of their intriguing properties, such as the extraordinarily high room-temperature carrier mobility, high thermal conductivity and high Young's modulus. These properties of graphenes can be employed in numerous potential applications such as transparent conductors and quantum devices. On the other hand, the control of electrical and optical properties is essential to realize graphene devices. Irradiation of graphenes with energetic particles is thought to enable us to control their properties and structure [2,3]. It has been reported that the doping level of graphenes can be also controlled by ion irradiation [4]. Several analytical techniques can be used to characterize irradiated graphenes. For example, Raman spectroscopy [5–9], transmission electron microscopy (TEM) [10], scanning tunneling microscopy (STM) [11], and X-ray photoelectron spectroscopy (XPS) [3] have been employed to study the properties and structure of irradiated graphenes. Soft X-ray absorption spectroscopy (XAS), on the other hand, is a powerful tool since it provides information on not only the local electronic structure surrounding excited carbon atoms, but also the orientation of the carbon π bonds [12]. In this study, to modify the electronic states of the multi-layer graphenes by the irradiation, we irradiated multi-layer graphenes with low-energy Ar ions (0.5–2 keV), and investigated the local electronic states by XAS.

Experiments and Results

Multi-layer graphene films were synthesized by thermal catalytic chemical vapor deposition. Figure 1(a) shows a transmission electron

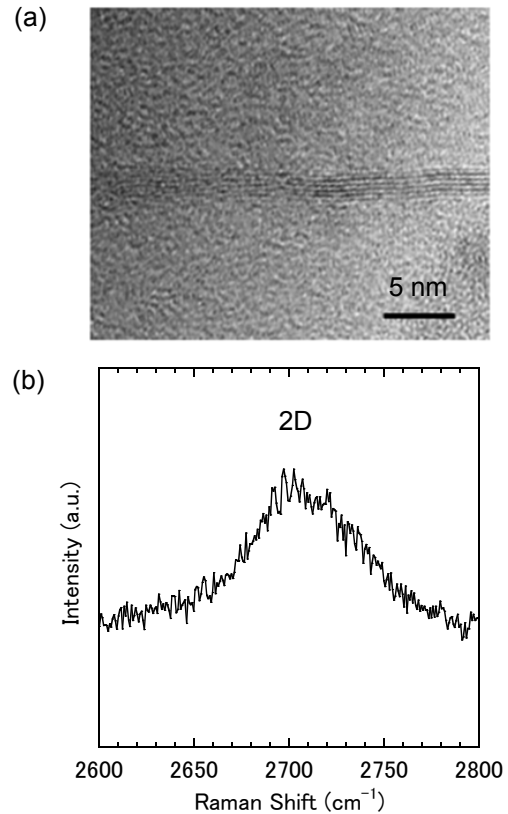


Fig. 1. (a) Cross-sectional TEM image of as-prepared multi-layer graphene films. (b) 2D peak of Raman spectrum of as-prepared graphene films.

microscopy (TEM) image of as-prepared multi-layer graphene films. The number and the total thickness of graphene layers were 6 and about 2 nm, respectively. We employed a Kaufman ion source (ULVAC-PHI MOD 04-370B) to irradiate the multi-layer graphene films at room temperature (RT) with Ar ions. The incident energy ranged from 0.5 to 2 keV and the dose varied between 1×10^{13} and $1 \times 10^{15} \text{ cm}^{-2}$. Micro-Raman spectra were taken with Ar ion laser (514.5 nm) using a Raman spectroscope (JASCO, NRS-2100). Fig. 1(b) shows the 2D peak of the Raman spectrum of the graphene films. It has been reported that the 2D peak changes in shape, width, and position with increasing number of graphene layers [13]. On the basis of the previous assignment, the number of graphene layers is estimated to be 3–5. This result is consistent with the results of TEM. The carbon K-edge XAS measurement was performed using BL09 of the 1.5 GeV synchrotron radiation source NewSUBARU at the University of Hyogo [14]. The total electron yield method was used for the measurement.

In order to explore local electronic states of the multi-layer graphene films, XAS was utilized for the multi-layer graphene films irradiated under different conditions. The spectra were measured at different angles of incident soft X-rays to the substrate surface (α) and normalized to their intensity at $\sim 320 \text{ eV}$. Fig. 2 is the XAS spectra of graphene films irradiated at an energy of 1 keV, taken at $\alpha = 55^\circ$. The π^* peak of 285 eV and σ^* peak of 292 eV were clearly observed. The $\text{sp}^2\text{-C}$ atom generally exhibits both π^* and σ^* peaks, whereas the $\text{sp}^3\text{-C}$ atom exhibits only the σ^* peak [15]. It was found that the intensity of the peak decreased with increasing ion fluence. This indicates decreasing number of $\text{sp}^2\text{-C}$ atoms after the ion irradiation. At the same time, an additional shoulder at $\sim 289 \text{ eV}$ is also recognized after the ion irradiation, as shown by arrow in Fig. 2. The energy at the shoulder is close to that at the C-K absorption edge for single-crystal diamond, and may be related to the formation of $\text{sp}^3\text{-C}$ atoms in the multi-layer graphene films [16]. With increasing ion fluence, an additional peak at $\sim 287 \text{ eV}$ was recognized in the XAS spectra, as shown by arrow in the Fig. 2. Additional peaks at $\sim 289 \text{ eV}$ and $\sim 287 \text{ eV}$, which appeared similarly in the previous study for the study for the damaging stages of multiwalled carbon nanotube films [17], have been respectively assigned to relate to the formation of $\text{sp}^3\text{-C}$ and dislocation dipoles. The dislocation dipoles possess fivefold and sevenfold rings, thereby inducing the buckling and the rotation of the hexagonal networks [18–20].

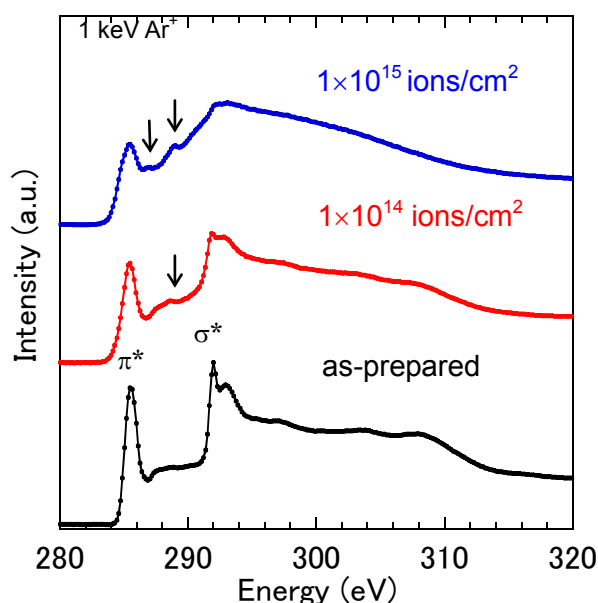


Fig. 2. XAS spectra of multi-layer graphene films irradiated by 1 keV Ar ions at different fluences.

References

- [1] K. S. Novoselov *et al.*, *Science* **306**, 666 (2004).
- [2] A. V. Krasheninnikov and K. Nordlund, *J. Appl. Phys.* **107** (2010) 071301.
- [3] F. Banhart *et al.*, *ACS Nano* **5** (2011) 26.
- [4] H.-G. Jee *et al.*, *Phys. Rev. B* **84** (2011) 075457.
- [5] G. Compagnini *et al.*, *Carbon* **47** (2009) 3201.
- [6] J.-H. Chen *et al.*, *Phys. Rev. Lett.* **102** (2009) 236805.
- [7] Y.-B. Zhou *et al.*, *J. Chem. Phys.* **133** (2010) 234703.
- [8] J. J. Lopez *et al.*, *Appl. Phys. Lett.* **107** (2010) 104326.
- [9] S. Mathew *et al.*, *J. Appl. Phys.* **110** (2011) 084309.
- [10] J. C. Meyer *et al.*, *Nano Lett.* **8** (2008) 3582.
- [11] L. Tapasztó *et al.*, *Phys. Rev. B* **78** (2008) 233407.
- [12] T. Hemraj-Benny *et al.*, *Small* **2** (2006) 26.
- [13] A. C. Ferrari *et al.*, *Phys. Rev. Lett.* **97** (2006) 187401.
- [14] M. Niibe *et al.*, *AIP Conf. Proc.* **705** (2004) 576.
- [15] J. Stöhr, *NEXAFS Spectroscopy* (Springer, Heidelberg, 1992).
- [16] F. L. Coffman *et al.*, *Appl. Phys. Lett.* **69** (1996) 568.
- [17] S. Honda *et al.*, *Jpn. J. Appl. Phys.* **51** (2012) 110202.
- [18] K. Niwase, *Philos. Mag. Lett.* **82** (2002) 401.
- [19] K. Niwase, *Mater. Sci. Eng. A* **400–401** (2005) 101.
- [20] K. Niwase, *Int. J. Spectrosc.* **2012** (2012) 1.

Fabrication of amino acid analysis chip using SR direct dry etching of PTFE

H. Kido ^a, I. Okada ^b, H. Mita ^c, A. Yamaguchi ^a, and Y. Utsumi ^a

^a University of Hyogo, 3-1-2 Kouto, Kamigori, Ako, Hyogo, 678-1205, Japan

^b Nagoya University, Furo-cho, Chikusa-ku, Nagoya, 464-8601, Japan

^c Fukuoka Institute of Technology, 3-30-1 Wajiro-Higashi, Higashi-ku, Fukuoka, 811-0295, Japan

Abstract

Polytetrafluoroethylene (PTFE) is very attractive material for various fields, because of its chemical resistance and heat resistance, etc. But, micro fabrication of PTFE is very difficult from its high stability. Therefore, PTFE has never been applied to micro fluidic device. However, it is known that synchrotron radiation (SR) induces scission of polymer chain of PTFE. We have ever been succeeded in the fabrication of PTFE micro fluidic chip using SR dry etching and thermal compression bonding. As a next step, we have been engaged in the fabrication of PTFE micro fluidic chip for amino acid derivatization process. PTFE is an ideal material for performing the derivatization process. Because, this process using some strong acid, and some processes such as extraction and hydrolysis require high temperature heating operation. There is no precedent of the application of such complex micro structure made of PTFE to the device for chemical analysis.

Introduction

In Solar system bodies, Amino acids, which are biologically important organic compounds, have played a key role in the chemistry that led to the origin of life on Earth. Precise analysis of the amino acid contained in extraterrestrial samples is very important in the study of the origin of life. We recently have opportunities for analyzing fresh extraterrestrial samples by collection of cosmic dust and sample return from asteroids, etc [1]. However, the amounts of the samples which can be used for analysis are limited because the samples are small in amount. Therefore, amino acid analyses for the samples using a micro fluidic chip are required. In this study, we develop the micro fluidic chip which can realize fluorescent derivatization required for optical isomer ratio analysis of the amino acid included in the samples.

Experiments and Results

The sequence of analysis operations for the amino acid in the extraterrestrial samples includes extraction, filtration, hydrolysis, and evaporative drying. Therefore, high chemical resistance and heat resistance are required for the material of the chip. For this reason, we chose polytetrafluoroethylene (PTFE) as a chip material. PTFE has very excellent chemical stability, and its heat resistance is far higher than those of plastic materials. Although the PTFE has the high chemical stability, micro fabrication of PTFE is difficult because the small modulus of elasticity is not suitable for normal mechanical processing. Up to now, micro fluidic device made of PTFE has never been reported. It is known that synchrotron radiation (SR) induces scission of polymer chain of PTFE [2 3]. Figure 1 shows the etching mechanism of SR direct dry etching of PTFE. We have been fabricated PTFE microstructures by direct dry etching using SR [4]. The combination of PTFE microstructure using SR dry etching process and compression bonding enables us to PTFE micro fluidic chemical analyzer. In previous study, we fabricated simple micro fluidic chip which had only one micro channel.

In this study, we developed a novel micro fluidic device which had multiple micro channels and incorporated a filter structure for filtration. Figure 2 shows the schematic diagram of fabricated amino acid analysis device. This device consists of two chips, and the function of valve is performed by sliding of the upper chip. The micro channels are incorporated into the lower chip. The lower chip has four reservoirs for reagent such as derivatization reagent, and each reservoir can hold 10 μ l. In addition, we disposed two reaction reservoirs for extraction and derivatization into the lower chip. Extraction reservoir has micro filter for filtration of protein contained in the sample on the downstream side of reservoir. We set the filter dimension to 50 μ m square because the size of extraterrestrial sample is assumed to be 100–200 μ m in diameter. Derivatization reservoir operates the hydrolysis of protein to amino acid and fluorescent derivatization. Heating operation in the derivatization reservoir is required in both sealed and open states. We realize both heating states in a single reservoir by opening and closing the upper part of the reservoir using the slide mechanism. In addition, the filter structure is incorporated in the derivatization reservoir for prevention of liquid leakage. For the function of the capillary valve, we set the filter dimension to 50 μ m square.

There is no precedent of the application of such complex micro structure made of PTFE to the device for chemical analysis. This study is very important for progress of science, technology and space development because our device has the potential to perform the chemical analysis with laboratory level on the spot where we are difficult to visit.

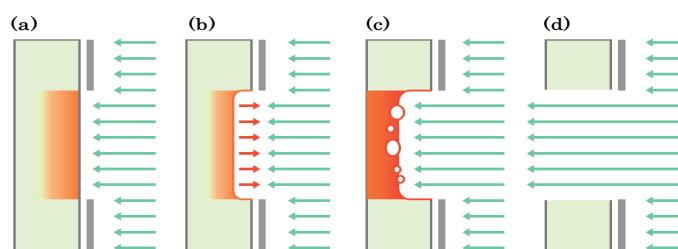


Figure 1. Etching mechanism of SR direct dry etching of PTFE: (a) drastic bond break in near surface, (b) bond break deep inside of the substrate and vaporizing from surface, (c) melting point shift and vaporizing from deep inside of the substrate, (d) penetration of mask pattern.

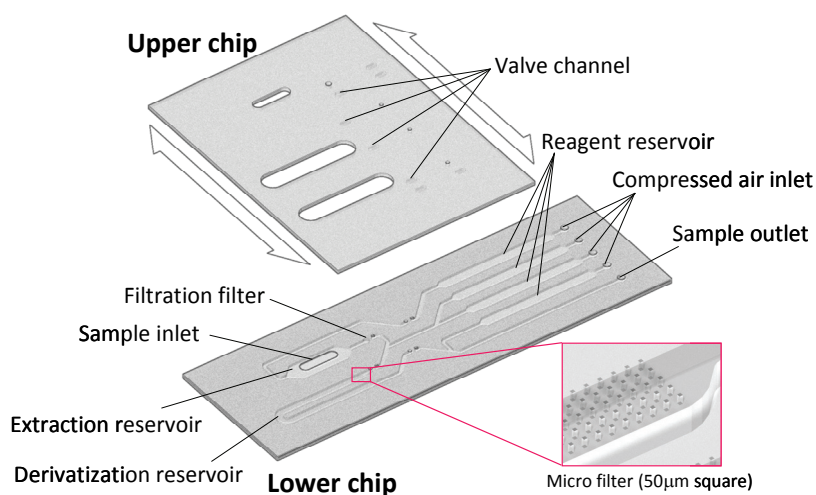


Figure 2. Schematic diagram of amino acid analysis device.

References

- [1] D. E. Brownlee, P. Tsou, J. D. Anderson, M. S. Hanner, R. L. Newburn, Z. Sekanina, B. C. Clark, F. Horz, M. E. Zolensky, J. Kissel, J. A. M. McDonnell, S. A. Sandford, A. J. Tuzzolino, JGR Planets, 108 (E10) (2003) 8111-8126.
- [2] Y.Zhang, T.Katoh, M.Washio, H.Yamada, S.Hamada, Appl.Phys.Lett.67 (1995) 872-874.
- [3] Yuichi Utsumi, Takefumi Kishimoto, Tadashi Hattori, Hirotsugu Hara, Jpn. J. Appl. Phys., 44,7B (2005) 5500-5504
- [4] Yoshiaki Ukita, Kazuhiro Kanda, Shinji Matsui, Mitsuyoshi Kishihara, Yuichi Utsumi, Microsyst Technol 14 (2008) 1567-1572.

Powder Transport Direction Control Method by Using Drive Frequency of Surface Acoustic Wave

Yasuto Arisue¹, Yuya Matsui¹, Tsunemasa Saiki², Kazusuke Maenaka³, Akinobu Yamaguchi¹
and ,Yuichi Utsumi¹

¹Laboratory of Advanced Science and Technology for Industry, University of Hyogo,
3-1-2 Koto, Kamigori, Ako-gun, Hyogo, 678-1205, JAPAN
Phone: +81-791-58-0232, Fax: +81-791-58-0232,

²Hyogo Prefectural Institute of Technology, Kobe, 654-0037, JAPAN
E-mail: pippikki@lasti.u-hyogo.ac.jpPlease

abstract

We propose a novel method for controlling the powder transport direction by drive frequency, and demonstrate the validity of this method by experiments. In our experiments we could observe several powder transports by specific combinations of inclination angles and drive frequencies.

Introduction

To integrate a lab-on-a-chip has been extensively studied. The surface acoustic wave (SAW) is particularly interesting because of its ability to add a novel liquid actuation method which makes to simplify the designing of lab-on-a-chips. Up to now, we succeeded in developing (SAW) actuators for transporting continuous liquid and a high-efficiency liquid mixing chip using SAW actuators [1]. Meanwhile, the displacement of solid by the SAWs had been reported [2]. If powder can be transported, we can establish a controlling process consisting of powder movement, powder injection into liquid, and themselves mixing operated only by the SAWs on one-chip. However, unlike continuously flowing liquid in a channel, spatially controlling powder transport by using the SAWs is difficult, because the powder transport direction must be aligned with an axis direction of an interdigital transducer (IDT) that generates the SAWs. Therefore, we changed the method for controlling the powder transport direction by using reflected SAWs from a micro groove and succeeded in moving the powder by the reflected SAW [3]. Moreover, if the powder can be transported in not only the upstream direction but also downstream direction of the SAWs, the flexibility of powder transportation will be enlarged in its applications. In this paper, we propose a novel method for controlling the powder transport direction by drive frequency, and demonstrate the validity of this method by experiments.

Figure 1(a) shows a photograph of our fabricated SAW actuator for powder transport. The SAW actuator was fabricated by IDT (1- μ m thick Al layer) patterning on a piezoelectric substrate (127.8 degree y-rotated x-propagating LiNbO₃) using photolithography. We fabricated four SAW actuators on a 4-inch wafer. Figure 1(b) shows a schematic diagram shown relationship between IDT and orientation flat of the wafer. The IDTs of the SAW actuators were located at inclination angles θ of 0, 30, 60, and 90-deg. against perpendicular direction of the wafer orientation flat. Here, we chose a proven IDT shape of a 200 μ m stripline pitch, a 5mm aperture, and 20 stripline pairs.

Experiments and Results

Figure 1(a) shows a photograph of our fabricated SAW actuator for powder transport. The SAW actuator was fabricated by IDT (1- μ m thick Al layer) patterning on a piezoelectric substrate (127.8 degree y-rotated x-propagating LiNbO₃) using photolithography. We fabricated four SAW actuators on a 4-inch wafer. Figure 1(b) shows a schematic diagram shown relationship between IDT and orientation flat of the wafer. The IDTs of the SAW actuators were located at inclination angles θ of 0, 30, 60, and 90-deg. against perpendicular direction of the wafer orientation flat. Here, we chose a proven IDT shape of a 200 μ m stripline pitch, a 5mm aperture, and 20 stripline pairs.

Figure 2 shows frequency characteristic of return loss (RL) of our fabricated SAW actuator. The RL is the logarithmic ratio of the incident electric power P_I to the reflected electric power P_R and increases as the applied power ratio to the IDT increases. At the SAW actuator with 0-deg. inclination angle, one RL peak was observed at 19.1MHz, and then multiple peaks were observed. The 19.1MHz is the conventional drive frequency of the SAW actuator, and corresponds approximately to the value of propagation velocity of a Rayleigh-wave (3690m/s) divided by IDT's pitch size (200 μ m). On the other hand, because there existed the multiple peaks, it is considered that the SAW actuator had potential to generate SAWs at their peak frequencies. In the same way as the SAW actuator with 0-deg inclination angle, there exist lots of RL peaks in the other SAW actuators with

different inclination angles.

Next, we investigated powder transport behaviors by the SAW actuators applied at the RL peak frequencies as drive frequencies. Figure 3 shows experimental setup for powder transport. Before starting the experiments, the powder was uniformly spread on the wafer by a sifter. Here, for the powder we used tungstic anhydride (average particle size of $22.3\mu\text{m}$) in consideration of visibility and insulation. In the experiment, a function generator created 1-kHz burst waveforms consisting of 2000 cycles of f_D MHz sine waves, where, it, corresponded to the obtained RL peak frequencies. If SAWs were generated by applying the boosted voltage, the powder might be transported by the propagated SAWs. At this time, the powder transport behavior was recorded with a high-definition video camera.

In our experiments we could observe several powder transports by specific combinations of inclination angles and drive frequencies. The most notable ones are that the SAW actuator with 90-deg. inclination angle could transport the powder forward and backward with high transport efficiencies in comparison with the other SAW actuators. The investigation powder transport characteristics with different inclination angles can be very useful in the designomg a chip consisting of the SAW actuators for powder transport control

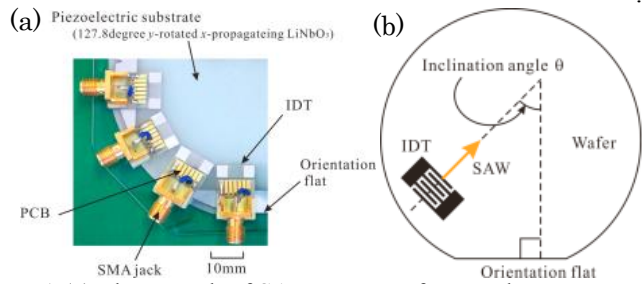


Figure 1 (a) Photograph of SAW actuator for powder transport. (b) Location relationship between IDT and orientation flat.

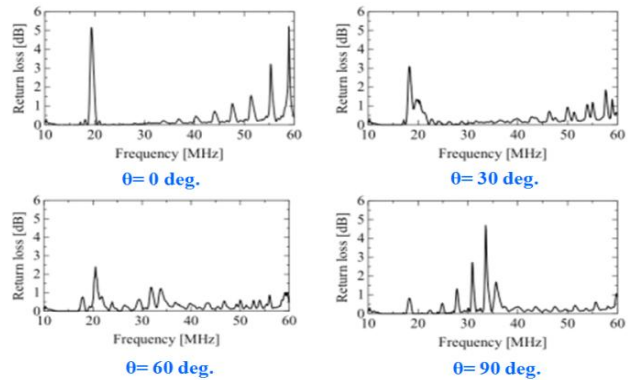


Figure 2 Frequency characteristic of return loss of SAW actuator.

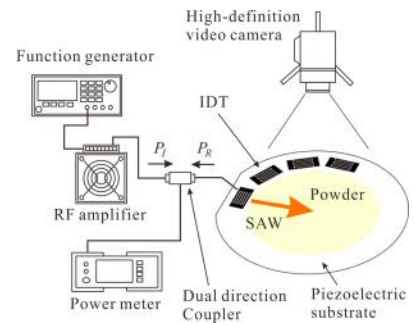


Figure 3 Experimental setup for observing the powder transport driven by SAW actuators.

- [1] T. Saiki, K. Okada and Y. Utsumi, "High Efficiency Mixing and Pumping of Continuous Liquid Flow using Surface-Acoustic-Wave", 13th International Conference on Miniaturized Systems for Chemistry and Life Sciences ($\mu\text{TAS}2009$), 58 (2009).
- [2] M. Kurosawa, M. Takahashi and T. Higuchi, "Ultrasonic Linear Motor Using Surface Acoustic Waves", IEEE Transactions on Ultrasonics, Ferroelectrics, and Frequency Control, 43, 901 (1996).
- [3] T. Saiki, H. Tomita, H. Shizuka, K. Okuda, K. Maenaka, Y. Utsumi, "Reflected Surface Acoustic Wave Actuator Using Micro Groove", 37th International Conference on Micro and Nano Engineering (MNE2011), 490 (2011).

Fabrication of SERS Active Three-dimensional Silver Nanostructure

R.Hara*, R.Takahashi*, T.Fukuoka*, A.Yamaguchi*, Y.Utsumi*

*Laboratory of Advanced Science and Technology for Industry, University of Hyogo

3-1-2 Koto, Kamigori, Hyogo, 678-1205 JAPAN

E-mail: hara099@lasti.u-hyogo.ac.jp Phone/Fax: +81-791-58-0232

Introduction

Recently, surface enhanced Raman scattering (SERS) is attracting attention as a high sensitive analysis system. SERS is the detection method using Raman spectroscopy and localized surface plasmon resonance (LSPR). To enabling strong LSPR, the noble metal nanostructure like gold or silver is essential. In previous report, gold nanoparticles were used to fabricate nanostructure. In this study, by using convective self-assembly [1] of particles, we developed the three-dimensional silver nanostructure (Ag3D) because low cost silver is more desirable material for SERS active nanostructure than gold. In addition, silver is thought to be suitable for the SERS measurement of various compounds.

Fabrication of Ag3D

We pasted silicone sheet with 6 mm throughhole on the UV-cleaned slide glass, and made a well. 5 μ l of the mixed solution of the silver nanoparticle (AgNP) and polystyrene latex beads (PS) was dropped into the well and dried at 75 % relative humidity for about 1 day. The PS colloidal crystal was fabricated by convective self-assembly, where AgNP were simultaneously accumulated in the gaps of the PS. The structure was soaked in dichloromethane to remove PS. Thus, Ag3D was successfully obtained (Fig.1).

SERS measurements

As shown in Fig.2, unique honey-comb structure of Ag3D was fabricated at a part of the well. We demonstrated in situ SERS measurement of 4,4'-Bipyridine (4bpy) as the Raman active molecule, using the Ag3D. First, silicone sheet with 6mm throughhole was pasted to the Ag3D on the glass to make a measurement well. Second, 35 μ l of 4bpy aqueous solution was dropped into a well on the Ag3D. A cover glass was put on to prevent drying of 4bpy solution and changing of 4bpy concentration. Ag3D was set to Raman spectrometer, and 1 s irradiation of 785 nm (50 mW) laser focused on the Ag3D was started.

We observed the characteristic enhanced Raman spectrum of 4bpy (1000 cm^{-1} , 1250 cm^{-1} , 1580 cm^{-1}) within 1 min after dropping 4bpy (Fig.3). SERS spectrum was only observed in the part of Ag3D, while no SERS was observed in the part without Ag3D. Raman spectra were enhanced about 10^5 times, compared with the case without Ag3D. Although the peak of 1 nM 4bpy solution was weak, it was detectable. The case with Ag3D and the case with Ag colloid aggregation were compared in the 4bpy peak height of 1580 cm^{-1} (Fig.4). SERS measurement using Ag3D was stable even after time passed, while peak intensity drastically dropped within minutes in the case with Ag colloid. one reason for this was that SERS active structure of Ag colloid was broken by aggregation process over time. In addition, we succeeded in observing the chloride activation which increased to 2-3 times in Raman intensity of 4bpy by the addition of NaCl to Ag3D (Fig.5). As a result, we have achieved a high sensitivity SERS measurement using Ag3D. SERS activity of Ag was generally higher than Au in the colloidal system, although obtained SERS using Ag3D [2] was still weak compared to the case using Au3D which was consisted gold nanoparticles. There is a possibility of enabling strong SERS if Ag3D fabrication is optimized.

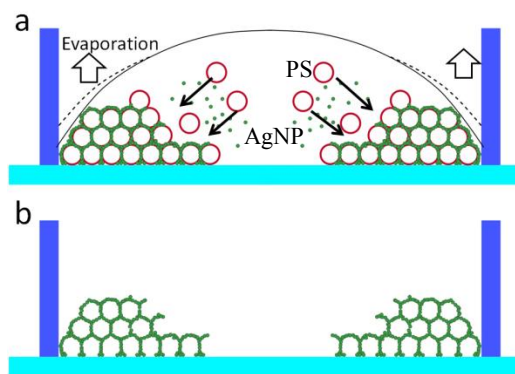


Fig.1: (a) A schematic diagram of self-assembled structure. (b) Ag3D after drying and remove PS

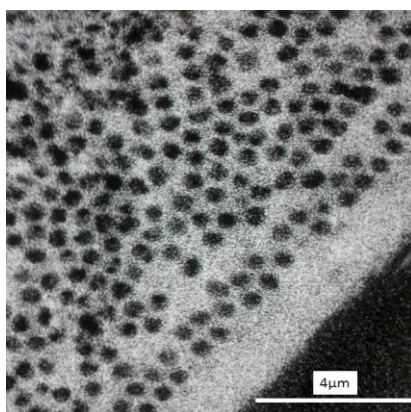


Fig.2: Microscopic image of three-dimensional silver nanostructure.

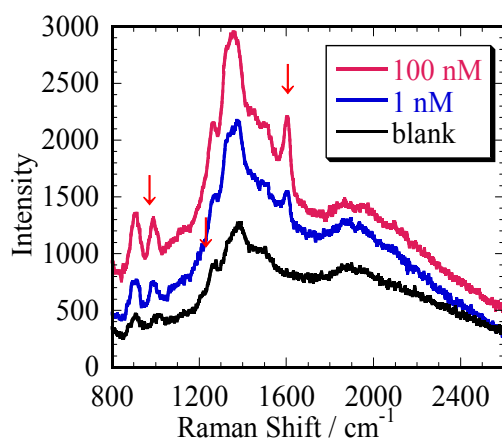


Fig.3: SERS spectra of 4,4'-Bipyridine.

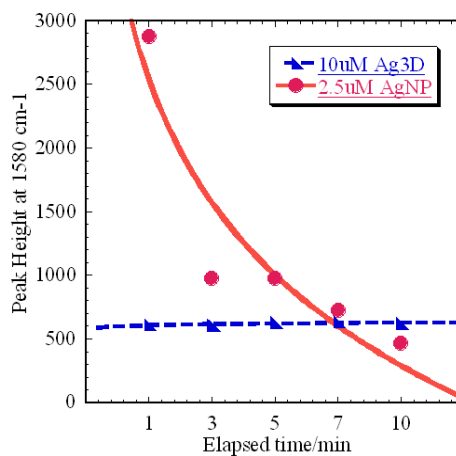


Fig.4: 4,4'-Bipyridine peak intensity with Ag3D and Ag colloid aggregation.

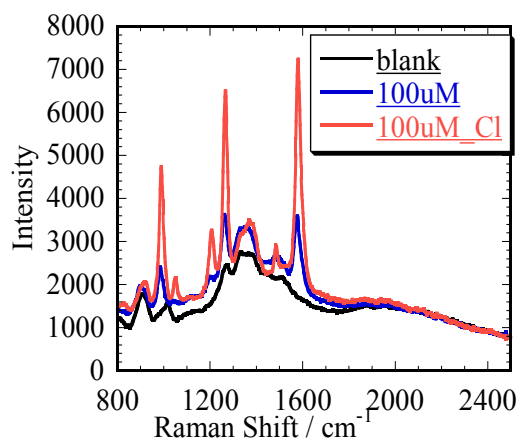


Fig.5: Chloride activation of 4,4'-Bipyridine

References:

- [1] Y. Mori, N. Shinohara, and T. Fukuoka, *International Workshop on Nanomechanical Cantilever Sensors 2008*, P48, 2008.
- [2] T. Fukuoka, and Y. Utsumi: *Rev. Laser Eng.* **40** (2012) 930 [in Japanese].

Blood separation chip

for automated biological analysis

T.Kunisada¹, H.Nose¹, M.Ishizawa¹, K.Kuroda¹, I.Okada², A.Yamaguchi¹ and Y.Utsumi¹

¹ *Laboratory of Advanced Science and Technology for Industry, University of Hyogo,*

3-1-2 Kouto, Kamigori, Ako-gun, Hyogo 678-1205, Japan

² *Nagoya University Synchrotron Radiation Center, Japan*

E-mail: takeshi@lasti.u-hyogo.ac.jp Phone/Fax: +81-791-58-0232

Abstract

We present a chip for the blood separation using centrifugal force and capillary force. We expect that this chip can perform overall assay with high-efficiency and significantly shorten the analysis time by integrate our proposed 3D lab-on-a-CD. The material of the chip which is fabricated by using X-ray lithography is SU-8 and Si. Blood separation is done using centrifugal force by spinning the chip at a frequency of 40Hz and transport to collection reservoir from separation reservoir using capillary force. It is necessary for capillary force to treat surface condition. We succeed in liquid transportation by only control spin speed.

Introduction

The lab-on-a-CD is promising for the automation of multiple microreactor systems. Recently, high-performance immunoassay based on lab-on-a-CD has been proposed [1]. The extraction of plasma from whole blood is the first preparative step in many assay protocols and major importance in medical diagnosis [2]. We present a chip for the extraction of blood plasma from whole blood using centrifugal force of spin and capillary force. We expect that this chip can be overall assay with high-efficiency and significantly shorten the analysis time by integrate our proposed 3D lab-on-a-CD [3].

We present a chip for the blood separation using centrifugal force and capillary force. We expect that this chip can perform overall assay with high-efficiency and significantly shorten the analysis time by integrate our proposed 3D lab-on-a-CD. The material of the chip which is fabricated by using X-ray lithography is SU-8 and Si. Blood separation is done using centrifugal force by spinning the chip at a frequency of 40Hz and transport to collection chamber from separation chamber using capillary force. It is necessary for capillary force to treat surface condition. We succeed in liquid transportation by only control spin speed.

Experiments and Results

We designed chip as shown in Fig.1. We formed a CHF₃ plasma chemical vapor deposition (CVD) film on the capillary valve just before the experiment. The plasma chemical vapor deposition (CVD) film with fluorine has a contact angle of over 100° [4]. By coating valve, liquid can be held until the higher rotation.

Process of blood separation is described in Fig.2. First of all, we injected whole blood into the separation reservoir (Fig.2a). In spinning the chip blood separation was performed by centrifugal force (Fig.2b,e①). Rotational speed is accelerated up to frequency of 25Hz (Fig.2e②). It was less than the burst frequency of the capillary valve. Phase separation was caused in a centrifugal field by a difference in mass density (Fig.2c). During blood separation, the capillary valve is used to control the flow sequence and hold liquid by surface tension. After finishing the separation, rotating speed was accelerated above the burst frequency. Then, the capillary valve was burst by the stronger centrifugal force (Fig.2d,e③). Next, liquid transportation was started and rotating speed should be decelerated to avoid disturbing rise by centrifugal force (Fig.2e④). Liquid rose in the capillary to the same height as the surface of liquid in the separation reservoir and reached the hydrophilic area. As soon as liquid reached the hydrophilic area, liquid is extracted by capillary force toward the collection reservoir. When liquid passed through the top of the capillary, rotating speed was accelerated again and extraction to the collection reservoir quickly (Fig.2e⑤). Blood cells remained at the bottom of the separation reservoir.

In this way, it is possible to control the flow sequence only controlling the rotation speed of the chip. We expect that the proposed chip will be able to extract only plasma from whole blood automatically.

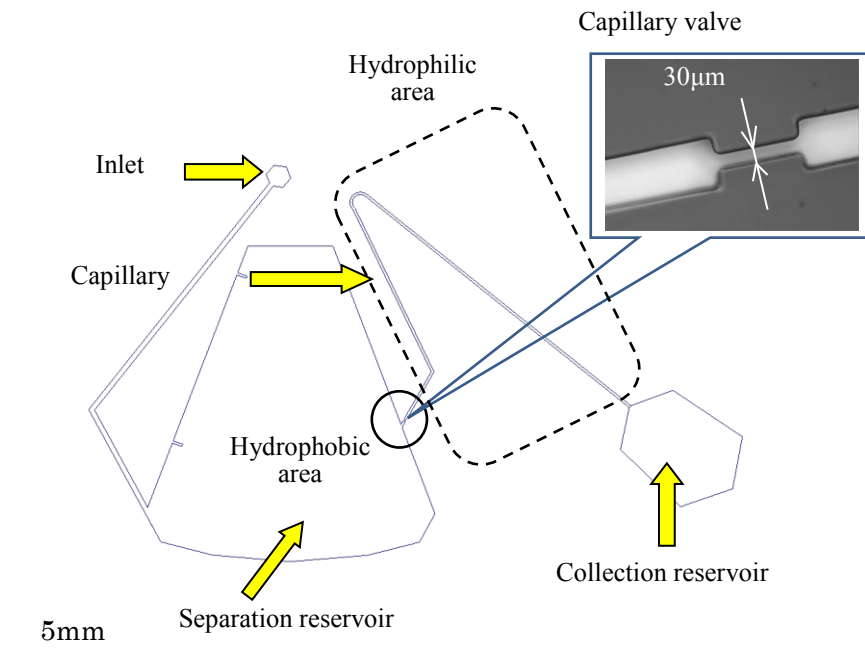


Fig.1: Schematic of microchannel.

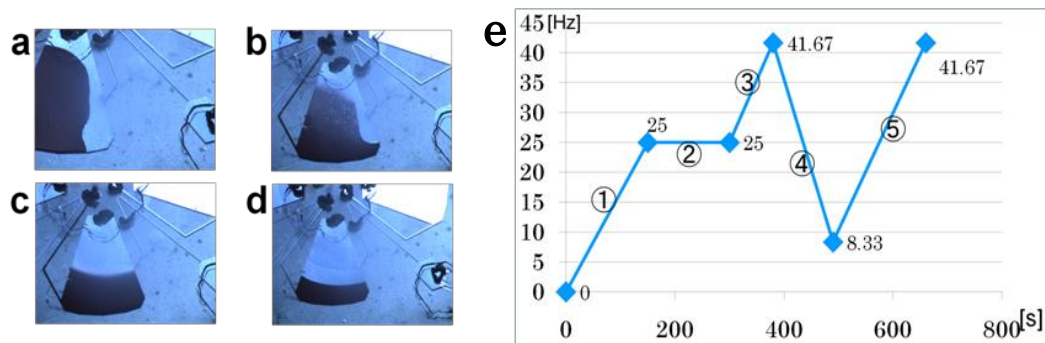


Fig.2: (a)-(d) Optical micrograph of each process of blood separation. (e) Protocol diagram.

References

- [1] S. Lai, S. Wang, J. Luo, L. J. Lee, S. T. Yang, and M. J. Madou, *Analytical Chemistry*, **76**, 1832, (2004)
- [2] Stefan Haebelre, Thilo Brenner, Roland Zengerle, and Jens Ducre, *lab chip*, **6**, 776-781, (2006)
- [3] Saki Kondo, Tsukasa Azeta, Yoshiaki kita, Yuichi Utsumi, *Microsyst Technol*, **16**, 1577-1580, (2010)
- [4] M.Okada, K.Nakamatsu, Y.Kang, K.Kanda, Y.Haruyama, and S.Matsui, *Applied Physics*, **48**, 06FH15, (2009)

Optimization of Surface Enhanced Raman Scattering Active Three- Dimensional Gold Nanostructure

R. Takahashi*, T. Fukuoka*, Y. Utsumi*, A. Yamaguchi*

*Laboratory of Advanced Science and Technology for Industry, University of Hyogo, 3-1-2 Koto, Kamigori, Hyogo 678-1205, JAPAN

E-mail: jo-ji@lasti.u-hyogo.ac.jp, Phone/Fax: +81-791-58-0232

Abstract: Recently, Surface Enhanced Raman Scattering (SERS) attracts attention as a high sensitive analysis system. Taking into account that one dimensional linearly connected gold nanoparticles (AuNP) [1] and two dimensional array of elongated AuNP [2] showed longitudinal localized plasmon resonance and excellent SERS performance, three dimensional layer stacks of chain-like assemblies of AuNP with numerous particle junctions are desirable. To accomplish thick stacks, we have focused on the three dimensional gold nanostructure (Au3D) using a casting method of convective self-assembly (CSA) of AuNP and polystyrene latex beads (PS) [3]. In this report, Au3D with thicker stacks was developed by optimization of AuNP and PS component in CSA and SERS measurements were demonstrated.

Fabrication of Au3D and SERS measurement: A PDMS sheet with a 6 mm through hole was attached on the uv-cleaned slide glass, where hydrophobic PDMS wall of the 6 mm well was made a circumference of “coffee-ring” so as to pin a drop of the AuNP (8.4×10^{14} particles/l) and PSL (2.3×10^{16} particles/l) mix dispersion with various composition which were dropped into the well. Since the hydrophobic surface of PDMS also made a convex meniscus of the drop around which surface/volume ratio was larger than other part of the drop, evaporation of water was accelerated around the circumference. As a result, the thickly stacked self-assemblies on the edge of “coffee-ring” was formed. After soaking with dichloromethane to remove PSL, sterically-bulky Au3D with enough thickness was obtained as shown in Fig. 1.

In situ SERS measurement was performed using Au3D and 4,4'-bipyridine (4bpy) as the Raman active molecule. 4bpy aqueous solution (30 μ l) was dropped into the measurement well, and covered with a cover glass in order to prevent drying or concentration. The collection time of each SERS measurement was 1 second (average 10 times at 0.1 second) using Raman spectrometer (RAM-100S, Lambda Vision Inc., Yokohama Japan) with 785 nm laser (100 mW). As results, we succeeded in 100 nM 4bpy detection.

Optimization of Au3D: In order to obtain further SERS active structure, we performed optimization of Au3D fabrication concerning dropping volume of mixed dispersion (3, 5, 7, 10, 15, 20 μ l), the particle number ratio (AuNP:PS = 100:1, 300:1, 1000:1, 3000:1), Au diameter (16, 22 nm) and PS diameter (100, 600, 1400 nm). SERS active of the Au3D were evaluated by measuring 4bpy. As results, optimum conditions of dropping volume, the number ratio, Au diameter and PS diameter respectively were 5 μ l, 1000:1, 16 nm and 600 nm as shown in Fig. 2-4. By using Au3D of optimum conditions, we achieved high sensitive measurement of 1 nM 4bpy as shown in Fig. 5. This enhancement reached over 10^7 compared with the normal Raman spectroscopy without Au3D.

In addition, we found that Au3D's width in radial direction depended on Au particle number. Then, the width of Au3D was controlled as shown in Fig. 6. By using this broad Au3D, the background from the slide glass was reduced even inexpensive Raman spectrometer without confocal system. Further high sensitive detection is expected by using broad Au3D. Furthermore, we also succeeded in the detection of 10 μ M histamine and 50 μ M melamine. Au3D is to be applied to the field of bioassay and food safety.

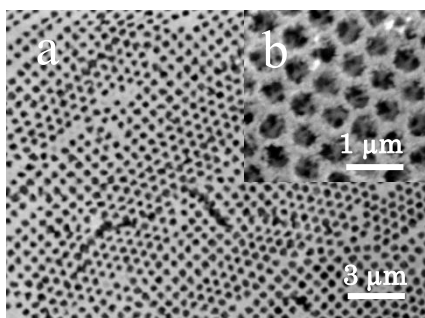


Fig. 1. (a) SEM image of Au3D. The diameter of the holes is about 600 nm. (b) Enlarged SEM image of honeycomb network of granular assembled gold nanoparticles.

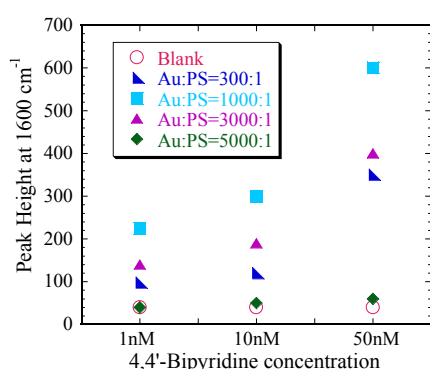


Fig. 2. Optimization of Au3D for SERS activity. Effect of particle number ratio (AuNP:PS).

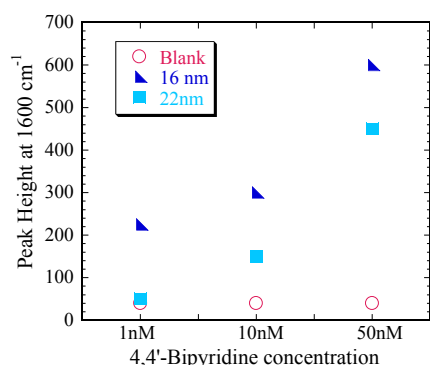


Fig. 3. Optimization of Au3D for SERS activity. Effect of Au diameter.

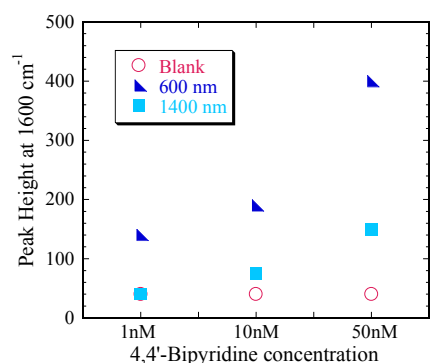


Fig. 4. Optimization of Au3D for SERS activity. Effect of PS diameter.

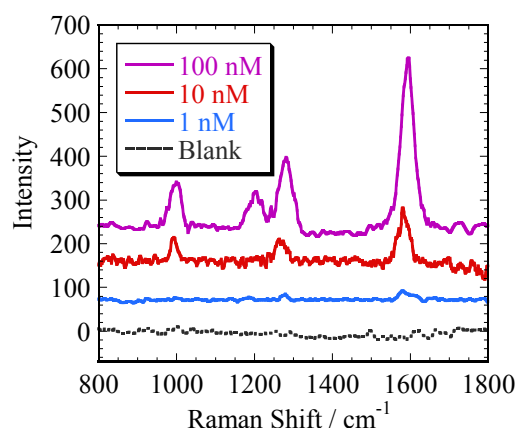


Fig. 5. Characteristic enhanced Raman spectra of 4bpy with different concentration (100 nM, 10 nM, 1 nM, Blank) by using optimum Au3D.

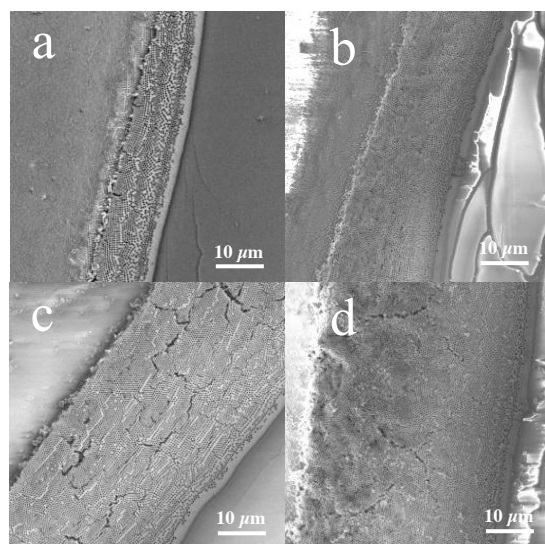


Fig. 6. Changes in Au3D width in radial direction depending on the particle number. (a) $0.5 \times 8.4 \times 10^{14}$ particles/l (b) 8.4×10^{14} particles/l (c) $2.5 \times 8.4 \times 10^{14}$ particles/l (d) $5 \times 8.4 \times 10^{14}$ particles/l.

References:

- [1] T. Fukuoka, *J. Jpn. Inst. Electron. Packaging (Electronics Jisso Gakkai Shi)*, 13(3), 168-176(2010) (in Japanese).
- [2] M. Suzuki, K. Nakajima, K. Kimura, T. Fukuoka, and Y. Mori, *Anal. Sci.*, 23(7), 829-833(2007).
- [3] Y. Mori, N. Shinohara, and T. Fukuoka, *International Workshop on Nanomechanical Cantilever Sensors 2008*, P48, 2008.

Fabrication and characterization of three-dimensional type micro magneto-impedance sensor

T. Yamamoto¹, Y. Yoritama¹, T. Uchiyama², Y. Utsumi¹ and A. Yamaguchi¹

¹Laboratory of Advanced Science and Technology for Industry, University of Hyogo, Koto, Kamigori-gun, 678-1205, Japan.

²Graduate School of Engineering, Nagoya University, Chikusa, Nagoya, 464-8603, Japan.

Abstract

Fabrication and evaluation of a three-dimensional micro-scale magneto-impedance (MI) sensor have been carried out. We present the detail of the fabrication process of the device and the measurement result of the impedance of the sensor head. The measured characteristics indicate that we succeeded the fabrication of the three-dimensional micro-scale MI sensor.

Introduction

In recent years, the people's concern about their health is increasing under the influence of aging society in advanced nations. Physical changes caused by external factor will be offset by the action of the autonomic nerve system. This indicates that the human health state depends on the autonomic nervous system. An un-invasive healthy monitoring system is required for the estimation and control of each of health status. The system consists of near-infrared spectroscopic devices for detecting the amount of substance inside blood and integrated magnetometric sensors to measure the dynamic characteristics of human's circulatory organ system as one of the function of the autonomic nervous system at the same time. The circulatory system response from the measurement results enable us to create the mathematical model which relates the response with exogenous stimulus. Therefore, health-maintenance medicine will be achieved by this model applied to the signal obtained from the sensor.

We need the high sensitive sensor in order to achieve the model. The change in the high frequency impedance of very soft ferromagnetic materials upon the action of external static fields, known as magneto-impedance (MI) effect, has been intensively studied for magnetic sensor applications.[1, 2] The high sensitive MI effect occurs when high frequency current is applied to the amorphous metal in which spin is arranged circumferentially. The MI sensors using MI effect has been recently attracting attention for improved the resolution of up to 10^{-12} T [1], which can measure bio-magnetic field in range from 10^{-10} to 10^{-15} T. The significant change in impedance is basically derived from the skin effect. The estimation of the high sensitivity of magnetic field is of great importance for the sensor application. The development of the general estimation method for the only inductance component of impedance also provides an insight to understanding the physical mechanism with respect to the relationship between the skin effect and micro- or nano-scale magnetization structure.

Experiments and Results

In this study, integrated coil, made of gold Au, is fabricated using UV lithography and succeeding packaging method to improve productivity. The $\text{Fe}_{21.5}\text{Ni}_{78.5}$ (Permalloy: Py) wire with thickness of 60 nm is prepared in the coil. The devices were fabricated by building up SU-8 layers as shown in Fig. 1. The fabrication process is also schematically illustrated in Fig. 1. Finally, one side of the device is covered with Kapton film for electrical insulation. Its size is 1.5 mm in length, 1 mm in width, and the thickness is 35 μm . The optical image of the device is shown in Fig. 2. In our device, the inductance component of impedance can be detected by not only the Py wire itself but also a pickup coil formed around the Py wire.

To evaluate the impedance of the device, we measured the impedance of the device as a function of the frequency (from 100 Hz to 100 MHz) by using a MI sensor electrical circuit device. As shown in Fig. 3, the impedance was rapidly increased with a frequency up to a 10 % when the frequency exceeded at about 20 MHz. The change in the impedance is attributable to not the ferromagnetic resonance but the normal skin effect because the ferromagnetic resonance frequency is far higher than the measured frequency region.

Although further systematic investigation is necessary in order to perfectly understand the physical mechanism and evaluate the MI effect, we have succeeded in fabricating a novel integrated MI sensor by means of UV lithography fabrication technique. The implementation of high sensitive MI sensors can provide biomedical monitoring system, car sensors and so on.

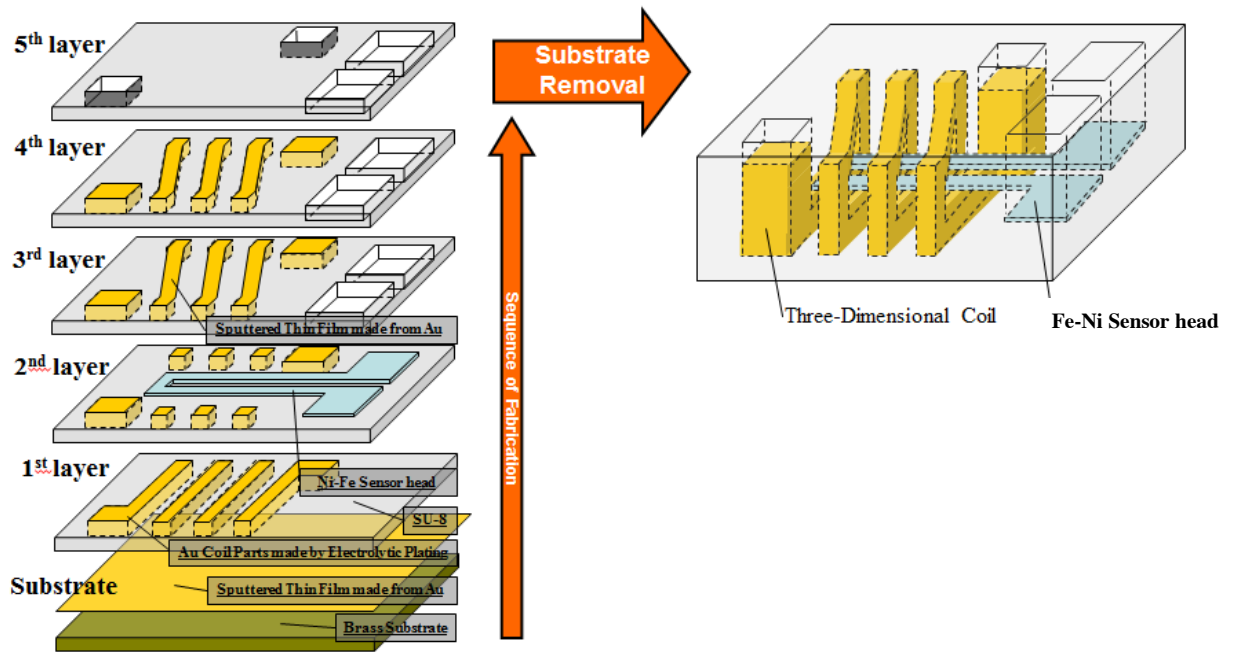


Fig. 1 Schematic of fabrication process and device.

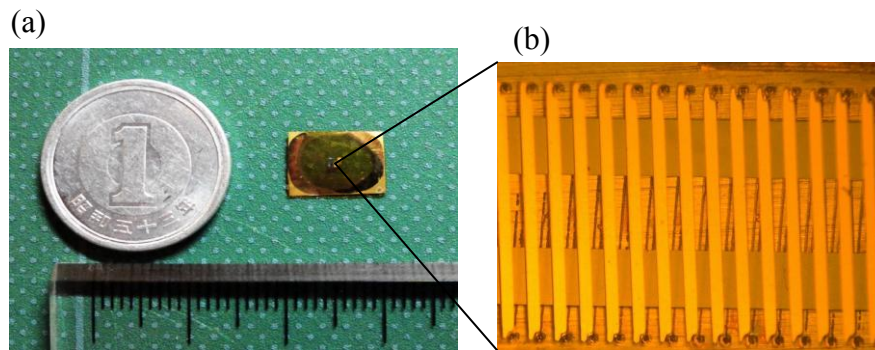


Fig. 2 Optical images of (a) the fabricated MI Sensor and (b) magnified coil region.

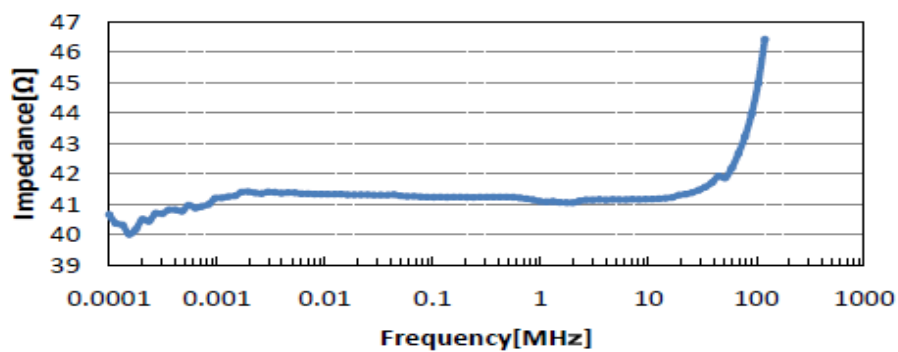


Fig. 3 The frequency dependence of the impedance of the fabricated MI sensor.

References

- [1] T. Uchiyama, A. Yamaguchi, Y. Utsumi., J. Magn. Soc. Jpn., 34(Japan, 2010).
- [2] K. Mori., Magnetic Sensors (Tokyo, Japan, 1998).

Micro-Mirror Array Device for floating image manufactured by Synchrotron radiation

T.Yamane^a, S.Maekawa^b, I.Okada^{a,c}, Y.Utsumi^a and A.Yamaguchi^a

^aLaboratory of Advanced Science and Technology for Industry, University of Hyogo, 3-1-2 Koto, Kamigori, Hyogo 678-1205, Japan

^bNational Institute of Information and Communications Technology, 3-5 Hikaridai, Seika, Soraku, Kyoto, Japan

^cNagoya University Synchrotron radiation Research center, Furocho, Nagoya Chikusa-ku, Aichi 464-8603, Japan

Abstract

We propose a new imaging optics called the Dihedral Corner Reflector Array (DCRA) which is designed to make the floating image. DCRA consists of numerous micro-mirrors placed perpendicular to the surface of substrate. The micro-mirror array is implemented by the inner walls of minute square holes or the side of minute square pillar. We can choose two types of the structure. The primordial is based on two reflections by a pair of adjacent mutually perpendicular mirrors, *i.e.*, a dihedral corner reflector. (S.Maekawa 2006.) Although the principal of operation is based on reflection by mirrors, the device is also transmissive and deflects light. Primordial of DCRA is not so complicated. However, it is too difficult to fabricate the DCRA by usual machining because of high aspect ratio micromachining. Therefore, in this manuscript, we fabricated the device by deep X-ray lithography due to synchrotron radiation. The characteristics of the fabricated DCRA are evaluated by the optical transmission and reflection measurements.

Introduction

There are some basic imaging optics which can form a real image, such as convex lens, a concave mirror, and diffraction optics (a Fresnel lens). For example, there are systems which are based on the lens array of the Graded Index Lens (GRIN) (H.Kita et al 1971), Roof Mirror Lens Array (RMLA) (M.Kawazu et al 1985), and the stacking of various micro-lens arrays (R.Volkel et al 1996). These have an optical axis and a specific focal length. Moving an object closer to the optics, the real image forms farther from it and is magnified. In contrast, imaging optics can form three-dimensional (3D) images without distortion. An example of this is a plane mirror. However, as a plane mirror can only form virtual images, the world in the mirror is treated as fantasy.

The authors of this paper propose a new imaging optics forming a real mirror image with the use of micro-mirrors. We called this imaging optics as the Dihedral Corner Reflector Array (DCRA).

because incident light is reflected twice when passing through a dihedral corner reflector. In the case of two-dimension structure, an incident light from a light source “A” is reflected in the direction “B” parallel to the light source “A” as shown in Fig. 1(a). Next, let us consider that the incident light from “A” into a dihedral corner reflector reflects two times at the mirrors and deflects toward the point “B” in 3D structure as shown in Fig. 1(b). Then, if the micro-mirrors are extremely small, the incident light passes through the substrate plane toward the symmetric point for the light source. When we prepare many dihedral corner reflectors on the substrate, all the light from a light source is converged onto the reflection-symmetric point of the source. As a result, the array of numerous dihedral corner reflectors, namely DCRA, can realize the floating image. (S.Maekawa 2006)

Image-formation and precision of DCRA

Here, we postulate that the transmittance of DCRA is the percentage of incident light through the reflection-symmetric point. The transmittance is given by

$$\text{Transmittance} = I \times R^2 \times T, \quad (1)$$

where I is the ideal transmittance, R is reflectance of micro-mirror, and T is the losses, which is defined as the attenuation of intensity of the incident light after passing through the DCRA.

Reflectance of micro-mirrors is the most important factor in imaging by DCRA. In this study, we expect that it is as close as possible to 100%. However, in the device, the micro-mirrors placed perpendicular to the surface of substrate. Therefore, no one can be polished after manufactured. Accordingly, reflectance of micro-mirrors is determined during the creation of the DCRA.

The perpendicularity of dihedral corner reflector plays an important role on the resolution of the imaging, and it

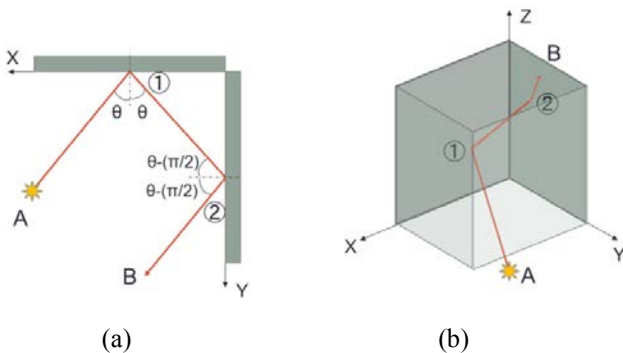


Figure 1 Operation mode of (a) two-dimensional- and (b) three-dimensional-dihedral corner reflectors.

The primordial of DCRA

The primordial of DCRA is based on mirror reflection. Figure 1 describes the operation of dihedral corner reflector. The reflection mode of DCRA is limited,

causes the distortion of the image. The dependence of the perpendicularity of the wall of DCRA can be estimated by using the simulation. This simulation enables us to calculate that the ray trace through position of light reflected by a line of plane mirrors from point light. Then, we can choose the value of the number of the plane mirrors, the distance of point light to the head mirror and the taper of mirrors. If the planes of mirrors in the DCRA are exactly perpendicular, all the reflected light by each mirrors pass through the same position of the head mirror. The floating image produced by the DCRA can be estimated to be distorted up to 10 μm when the plane mirrors have 1 minute taper.

Image resolution is determined by the dimension of the dihedral corner reflector. The higher resolution image can be obtained, the smaller dihedral corner reflectors in the DCRA are fabricated. However, the image produced by the smaller DCRA will darken because the diffractive component of the light increases.

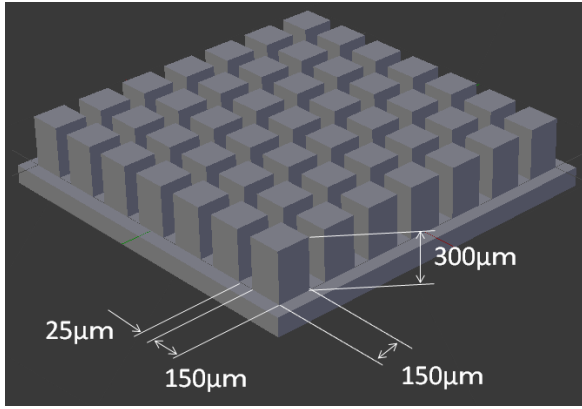


Figure 2 Schematic of the DCRA device designed in this study.

Table 1 Dimension of DCRA

Length of square side [μm]	150
Pillar height [μm]	300
Pitch [μm]	25
Ideal transmittance [%]	100
Aperture ratio [%]	64.9
Perpendicularity [deg]	90
Roughness [nm]	10

Fabrication of DCRA

Polishing the micro-mirrors is easy if they are parallel to the device surface. However, because micro-mirrors are perpendicular to the device surface in the DCRA, it is impossible to polish them in pre- or post- processes. Therefore, the micro-fabrication of high precision is required for the fabrication of DCRA. In this manuscript, we fabricated the pillar patterned DCRA made of Poly-methyl methacrylate (PMMA) by using synchrotron

radiation (SR). The fabrication process using the SR enables us to fabricate the DCRA structure within the limit of accuracy of about 1 nm. Figure 2 shows schematic of dimensions of our DCRA device. As shown in Fig. 2, a dihedral corner reflector is made by a pillar with square section.

The incident light through inside of pillars made of PMMA in pillar patterned DCRA. Considering the PMMA refractive index, we design the aspect ratio (height/width) of our device is two in order to achieve that the theoretical value of light transmittance of our device is expected to be 100%. The aperture ratio, namely the portion of the opening, is determined by the pitch between the reflectors. We estimate the effective fraction transmitted of our device is 64.9% considering the contribution of the aperture ratio. Expressed in another way, the brightness of the floating image is expected to be 64.9% with the respect to that of an object. The dimension and desired values of DCRA are summarized in Table.1.

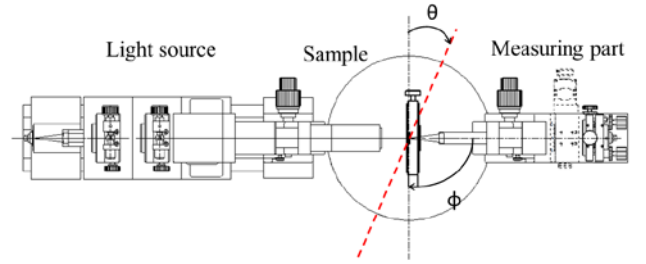


Figure 3 Schematic of transmission-reflection ratio measurement system. θ is an angle between the perpendicular direction of the incident light axis and sample horizontal plane. ϕ is an angle between the perpendicular direction of the light axis and detector.

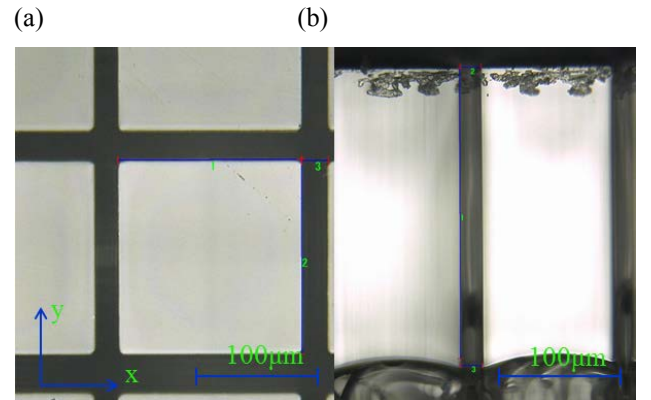


Figure 4 Optical microscope image of (a) top view and (b) cross section of the pillars in our DCRA.

Table 2 Dimension of the fabricated DCRA

Length of square side [μm]	(x) 150.92
	(y) 151.42
Pitch [μm]	25.87
Pillar height [μm]	326.78
Perpendicularity[minute]	5.8

Results and discussion

Up to now, the criteria and evaluation method for the properties such as the resolution and brightness of the image produced by the DCRA have not yet been established. In this study, we evaluate the characteristics of the fabricated DCRA by measuring the dimension, perpendicularity of the reflector, fractional transmitted and reflection. The attenuation of brightness and reflection ratio are measured by transmission-reflection ratio measurement system as shown in Fig.3.

Figures 4(a) and 4(b) show a typical optical microscope image of top view and cross section of the micro-pillars in the fabricated DCRA, respectively. The measured average dimensions of the DCRA are summarized in Table 2. The measured dimensions except the perpendicularity are almost in good agreement with the design dimensions. The perpendicularity of the fabricated pillars have about 6 minute taper. The evaluation using the simulation indicates the taper structure causes the distortion of $65\ \mu\text{m}$ with respect to the distance of light source. This distortion is serious for the observation of a floating image formed by DCRA.

Next, the attenuation of brightness is evaluated by the transmission-reflection ratio measurement system shown in Fig. 5. The measured fraction transmitted was about 40%, being in acceptable range of the design. As shown in Fig. 5, we can see a broad change from 400 nm to 600 nm in wavelength. The change corresponds to the absorption derived from the discoloration of PMMA by SR.

Finally, the reflection ratio was evaluated by using the same measurement system. Here, the coordinate system is defined as shown in Fig. 3. In order to evaluate the angle ϕ dependence of the single reflection of the DCRA at 700 nm in wavelength, we fixed the DCRA at the angle $\theta = 25^\circ$. The measured angle ϕ dependence of the reflection is shown in Fig. 6. As shown in Fig. 6, two reflection peaks are observed. The peak with the larger amplitude (at about $\phi = 0^\circ$) corresponds to the refractive incident light. The other is the single reflection of the light by the DCRA. If the ideal DCRA was fabricated, we would obtain the single reflection peak at $\phi = 50^\circ$ in this experimental setup. However, we

found the single reflection was extended in the ϕ range between 40° and 70° because the reflected light was spread by the distortion due to the taper. The actual fraction transmitted is estimated to be 5.4% by substituting the measured value into Equation (1). This indicates that a dark floating image is formed by the fabricated DCRA. However, we succeeded in forming the floating image by the fabricated DCRA as shown in Fig. 7.

The improvement of fabrication process and evaluation of the DCRA will open the door to the novel imaging devices.

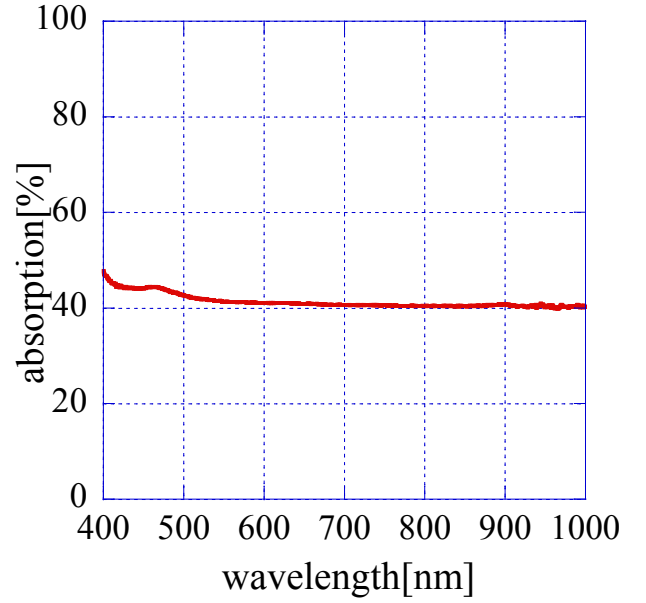


Figure 5 Absorption as a function of wavelength.

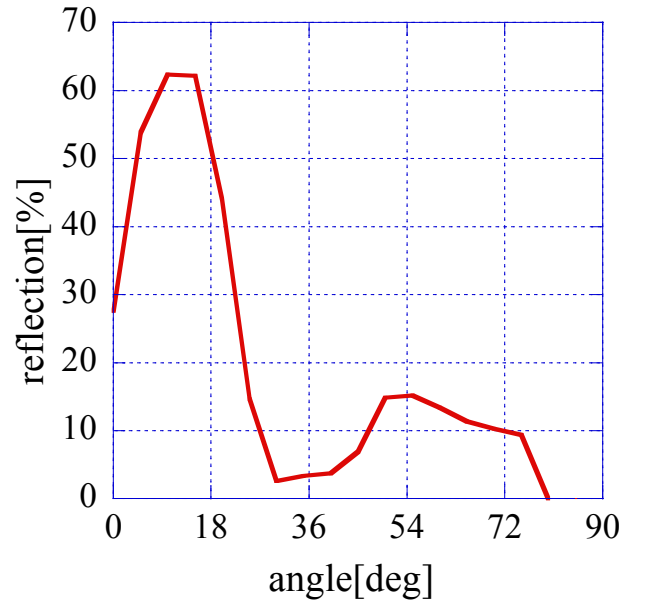
Figure 6 The angle ϕ dependence of the fabricated DCRA.



Figure 7 A typical floating image is imaged by the fabricated DCRA.

Conclusion

We proposed novel imaging optics with micro-dihedral corner reflector arrays (DCRA) which can form a reflection-symmetric image as a real image in the air. It was fabricated by synchrotron radiation. We evaluated the fraction transmitted and single reflection of the fabricated DCRA by the optical measurement system. Although the performance of the DCRA was not good, the fabricated DCRA enables us to observe a floating image. By comparing the simulation result with the experimental evaluation, we can understand what worsen the performance of the DCRA.

Our main work to improve imaging in the future is to increase transmittance and establish the quantitative measurement method of resolution and reflection ratio.

Reference

- [1] S.Mackawa. "Transmissive Optical Imagin Device with micromirror Array" The international society for Optical Engineering, Vol. 6392, 63920E-1, 2006.
- [2] H.Kita, I.Kitano, T.Uchida, and M.Furukawa, "Light-focusing glass fibers and rods," Journal of the American Ceramic Society 54, pp. 321-326, 1971.
- [3] M.Kawazu and T.Inokuchi, "Imaging Device using a roof micro lens array," Applied Optics 24(24), pp.4300-4306, 1985.
- [4] R.Volkel, H.Herzig, P.Nussbaum, and R.Dandliker, "Microlens array imaging system for photolithography," Optical Engineering 35(11), pp.3323-3330,1996.
- [5] M.Ishikawa, "A proposal to create the impression of a miniature garden, and the development of a glasses-free small 3d display", Pioneer R&D 12(3), pp.47-58, 2003. In Japanese.

Broadband noise spectroscopy of a magnetic wire

A. Yamaguchi¹, K. Motoi², H. Miyajima² and Y. Utsumi¹

¹Laboratory of Advanced Science and Technology for Industry, University of Hyogo, Koto, Kamigori, Ako, Hyogo 678-1205, JAPAN

²Department of Physics, Keio University, Hiyoshi, Yokohama, Kanagawa 223-8522, JAPAN

E-mail: yamaguti@lasti.u-hyogo.ac.jp

Tel: +81-791-0041

Abstract

We measured broadband magnetic noise spectrum induced in a single layered Ni₈₁Fe₁₉ nano-scale wire biased with a dc-current in a frequency range from 500 MHz to 8 GHz. The magnetic noise spectra are recorded as a function of external magnetic field and dc-current. Experimental measurement results and analytical calculations reveal that the noise generation is caused by the thermal magnetization fluctuation due to ambient temperature and Joule heating.

Introduction

The spin dynamics in a nano-scale magnet with a confined structure has gained increasing attention over the last decades due to the scientific and technological interest. [1] To understand the mechanism of the spin dynamics from a microscopic perspective, the special instrumentality and measurement system, such as magneto-optic Kerr effect, Brillouin light scattering and ferromagnetic resonance, are required until now. [1] Several electrical measurements that are suitable for investigating the spin dynamics in nano-scale magnets and are extremely sensitive have been proposed recently. One of them is the homodyne detection of the resistance change induced by the spin-transfer torque and magnetic fields. The magnetic noise measurement of a nano-scale magnet, in particular for giant magnetoresistive (GMR) devices and tunneling magnetoresistive (TMR) devices, can be used as other tools. [2, 3] The GMR or TMR noise tests are nondestructive and can be applied to the read heads for the magnetic hard disk drive. For diagnostic testing, we interested in the noise induced by the spin-transfer torque, magnetic fields and thermal excitation. [2-4]

This paper reports our investigation of broadband noise spectroscopy in a single layered Ni₈₁Fe₁₉ (Permmalloy: Py) wire.

Experiments and Results

The soft-ferromagnetic Py nano-scale wire is fabricated onto a polished MgO (100) substrate by means of high-resolution electron beam lithography with a standard lift-off technique. The thickness, width and length of the prepared Py wire are 20 nm, 2.2 μ m and 100 μ m, respectively. The wire is placed between the center strip-line of the coplanar waveguide (CPW) comprising Au conductive strip with thickness of 100 nm. The optical micrograph image and schematic circuit diagram for broadband noise measurement are shown in Fig. 1.

Figure 2 shows the homodyne detection spectrum (black solid line) [5] and the lock-in detection noise spectrum (red solid line). It should be noted that the resonance frequency around 3.8 GHz of the magnetization fluctuation signal almost matches that of the homodyne detection spectrum, indicating that the origin of the noise signal induced by dc-current is the same as that of the homodyne detection signal. We also measured the magnetic field dependence of the broadband noise spectra. As a result, the resonance frequency correlates well with the ferromagnetic resonance frequency, and the amplitude of the noise signal at the resonance frequency decreases with increasing the static field.

These experimental results suggested that the measured noise signal is derived from the magnetization precession induced by the thermal fluctuation. The present experimental results are in good agreement with the analytical solutions. [2-4] We believe this study provides not only the important physics on the fundamental limitation in the possibility of the scale-down size but also the improvement in the read heads and in the radio-frequency devices.

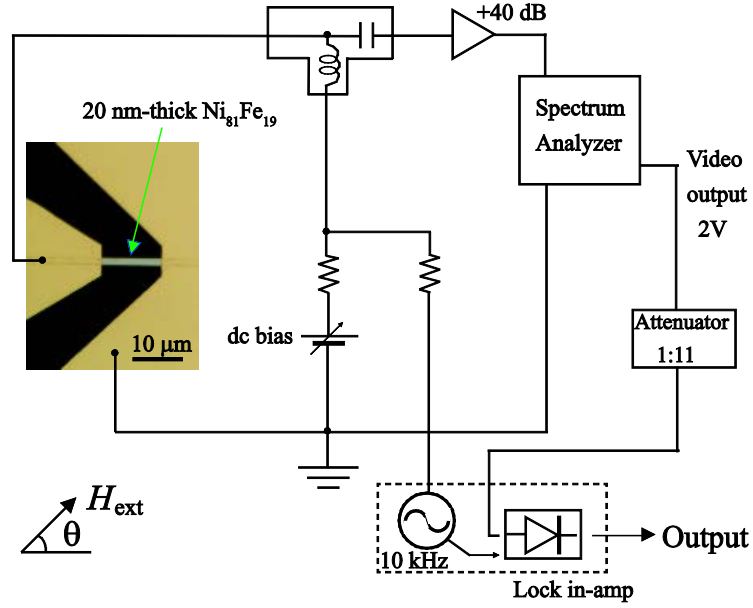


Fig.1 Optical micrograph image of the Py wire and schematic diagram of the broadband noise measurement circuit.

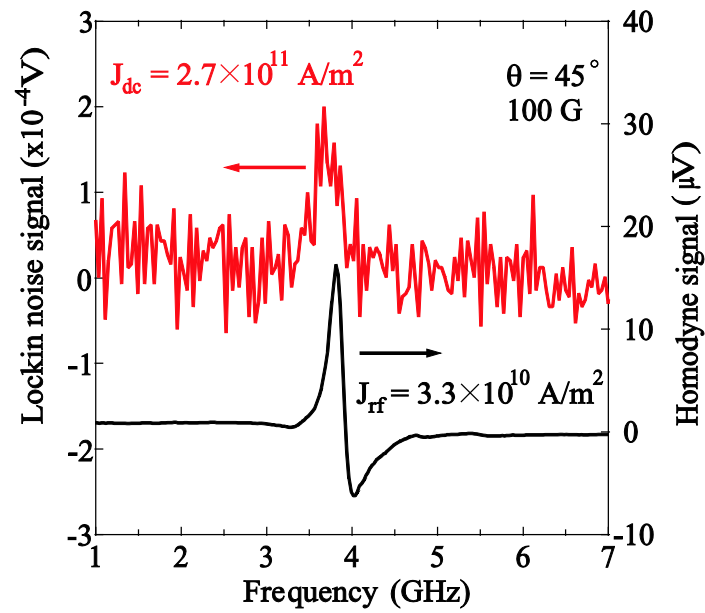


Fig. 2 Homodyne signal spectrum and broadband noise spectrum in magnetic field of 100 G at $\theta = 45^\circ$.

References

- [1] B. Hillebrands and K. E. Ounadjela, Spin Dynamics in Confined Magnetic Structures (Springer, Berlin, 2003), Vols. 1 - 3.
- [2] N. Smith and P. Arnett, *Appl. Phys. Lett.* **78**, 1448 (2001).
- [3] K. B. Klaassen, J. C. L. van Peppen and X. Xing, *IEEE Trans. Magn.* **93**, 8573 (2003).
- [4] V. Safonov and N. Bertram, *Phys. Rev. B* **65**, 172417 (2002).
- [5] A. Yamaguchi, K. Motoi, A. Hirohata, H. Miyajima, Y. Miyashita, and Y. Sanada, *Phys. Rev. B* **78**, 104401 (2008).

Defect Characterization of an EUV Mask using a Coherent EUV Scatterometry Microscope

Tetsuo Harada^{1,2}, Masato Nakasuji^{1,2}, Akifumi Tokimasa^{1,2}, Yutaka Nagata^{2,3}, Takeo Watanabe^{1,2}, and Hiroo Kinoshita^{1,2}

1 Center for EUV Lithography, Laboratory of Advanced Science and Technology for Industry, University of Hyogo, Kamigori, Hyogo 678-1205, Japan

2 Core Research for Evolutional Science and Technology, Japan Science and Technology Agency, Kawaguchi, Saitama 332-0012, Japan

3 Laser Technology Laboratory, RIKEN, Wako, Saitama 351-0198, Japan

Abstract

On extreme-ultraviolet (EUV) masks, phase structures such as bumps or pits on the substrate or particles buried in the multilayers can form printable defects at EUV exposure tool. Property of these defects is required for mask repair by defect hiding and compensation methods using the absorber pattern. We have developed a coherent EUV scatterometry microscope (CSM) to observe EUV masks, which uses a simple lensless system to record a diffraction image from mask patterns. We introduce preliminary observation results for programmed phase defects. We evaluated the defect width and height from the diffraction images, and the detection limit of the CSM system reached a width of 220 nm. To characterize small defects, we proposed a micro-CSM system that focused to the illumination onto the defect with a 100 nm diameter. The diffraction image recorded by the micro-CSM system provides raw defect data, which is essential for defect compensation.

Introduction

In extreme-ultraviolet (EUV) lithography, defect-free mask production is one of the critical issues for high-volume manufacturing. A mask is a master pattern for a semiconductor device, and there must be no defects on this mask. In EUV lithography, the EUV mask is a reflective type mask, unlike the transparent-type mask used for conventional 193 nm lithography. The EUV mask is coated with a Mo/Si multilayer, and an absorber layer, in which patterns are printed to form a device pattern. However, phase structures such as bumps or pits on the substrate or particles in the multilayers can form printable defects. For example, a shallow structure of 1 nm on the surface of a mask substrate causes a large reflection phase shift of 53° at EUV wavelength. As a result, this buried defect is printable.¹⁻⁶⁾

Buried defects can be detected efficiently at the mask blank stage of manufacture, which is just before the deposition of the absorber layer. The Selete and EIDEC groups have developed an actinic blank inspection (ABI) tool to detect phase defects.⁷⁻¹⁰⁾ The ABI tool is a dark-field EUV microscope composed of a discharge-produced-plasma source and Schwarzschild optics, which collects scattered EUV light from buried defects to form a dark-field image on a charge-coupled-device (CCD) camera. Because the defect signal is integrated in a dark-field, the ABI tool has a good signal-to-noise (S/N) ratio for the detection of defects.

Current EUV masks do not satisfy defect density requirements.^{11,12)} As a result, defect hiding and defect compensation methods have also been proposed,^{13,14)} which work by modifying the

absorber pattern to compensate the aerial image. Detailed defect information, such as defect position on the mask, defect size, and phase distribution, is necessary for the compensation process. However, the ABI tool is specifically intended for defect detection, for which the magnification requirement is not high. The spatial resolution is determined by the CCD pixel size, where one pixel integrates the scattering signal from a 500×500 nm² region on the mask. It is thus difficult to use the ABI tool to characterize the phase defect information. In this study, we observed the phase defects using a coherent EUV scatterometry microscope (CSM), which is a lensless type of microscope.¹⁵⁻¹⁹⁾ The CSM records the diffraction from the mask directly using a CCD camera. We discuss the requirements for a defect characterization tool based on the preliminary observation results for programmed defects. We also propose a micro-CSM system for defect characterization, which focuses the illumination onto the defect with a 100 nm diameter.

Experiment

We observed the phase defects using the CSM system shown in Figs. 1 and 2. The CSM system was installed at the BL-3 beamline of the NewSUBARU synchrotron radiation facility,²⁰⁾ which uses a bending magnet as a light source. Two toroidal mirrors collimate the white light into the CSM system. Figures 1 and 2 show a photograph and a schematic view of the CSM system, respectively. A pinhole with a 5 μm diameter is exposed with the collimated EUV beam and the beam diameter is then reduced to improve the spatial coherence. A concave spherical

mirror and a plane turning mirror are then used to reflect the beam onto the EUV mask, and thus the pinhole image is relayed to the mask. The radius of curvature of the concave mirror is 200 mm, and the distance from the pinhole to the concave mirror is 200 mm, which is the same as the distance from the concave mirror to the mask. The mirrors are coated with 40 pairs of Mo/Si multilayers. Diffraction from the mask is recorded using a back-illuminated CCD camera. The CCD surface is placed parallel to the mask surface. The imaging area is $27.6 \times 27.6 \text{ mm}^2$, and contains 2048×2048 arrays of imaging pixels with an area of $13.5 \times 13.5 \text{ }\mu\text{m}^2$. The angle of incidence from normal is 6° on the EUV mask, which matches the angle used in current EUV lithography scanners. The distance from the mask to the CCD camera is approximately 100 mm, which is equivalent to a numerical aperture (NA) of 0.14. The estimated spatial resolution is 59 nm.

A phase defect scatters EUV light illumination, where the signal depends on the phase distribution. When using conventional imaging optics, this phase distribution is recorded as a small dark spot on the detector caused by destructive interference. High magnification is required to characterize the defect. In contrast, the CSM can record the scattering signal directly, including the complex amplitude information of the defect. We have successfully reconstructed edge structure of line-and-space pattern from these scattering signals using a coherent diffraction imaging method.²¹⁻²⁷⁾ We have also succeeded in reconstructing both an intensity image and a phase image.¹⁹⁾

The sample mask was a blank EUV mask, which contained programmed bump structures on a glass substrate. The bumps were located with a $10 \text{ }\mu\text{m}$ pitch. The bump height was 7 nm, and the bump width was varied, ranging from 70 to 420 nm, with a square shape.

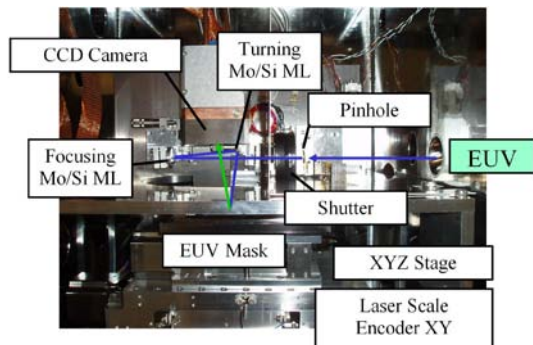


Fig. 1 Photograph of the CSM system. The arrows show the light path of the synchrotron radiation. The CCD camera records diffraction from the EUV mask pattern.

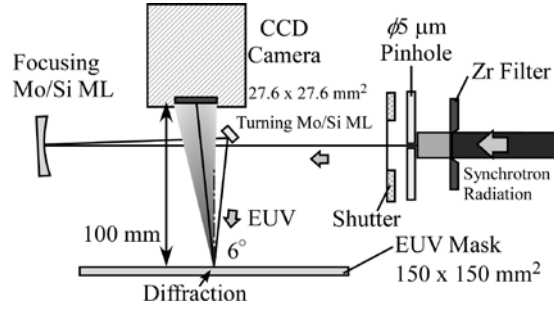


Fig. 2 Schematic view of the CSM system.

Results

Figure 3 shows a diffraction image with a phase defect recorded using the CSM. The exposure time was 1,000 s. The intensity is shown in log scale. The defect was 420 nm wide and 7 nm high, as measured by atomic force microscopy (AFM). This defect had a truncated-pyramid shape with slope width of about 70 nm. The strong diffraction signal around the defect center was from the illumination. The Fraunhofer diffraction from the $5\text{-}\mu\text{m}$ -diameter entrance pinhole was recorded at the center position, as shown in Fig. 3. The illumination profile was asymmetric, because the small turning mirror limited the illumination pupil size. The center illumination signal was saturated because of the long exposure time, and the intensity was estimated to be 8.8×10^5 counts from other data with shorter exposure times. Because the cross-shaped diffraction signal around the illumination came from the defect, the defect shape was determined to be a square. The diffraction signal intensity was about 30 counts, which was 10^{-4} times weaker than the intensity at the illumination center. The defect width was estimated to be about 430 nm from the diffraction width of the crossed line, which corresponded well with the AFM value. The defect height was estimated to be 6.5 or 7.0 nm from the diffraction intensity ratio of the center to the crossed parts. The reflection phase change of the height was equal to 13.0 or 14.0 nm, which was a difference of 0.5 nm (0.23 rad) from the 13.5 nm EUV wavelength. Thus, the estimated height also corresponded well with the AFM value. We therefore successfully evaluated the defect width and height precisely using the CSM system.

Figure 4 shows diffraction images of defects with widths of (a) 420, (b) 220, and (c) 130 nm, and image (d) without a defect. The intensity was shown on a linear scale. All the defect heights were about 7 nm. The defect of 220 nm width also had a truncated-pyramid shape. Thus, the slope widths of (a) and (b) were about 70 nm at both sides, which was measured by AFM. That of the 130 nm-wide defect had a Gaussian shape. At the defect width of 420 nm shown in Fig. 4(a), the diffraction shape was easily recognized as a cross. However, because the diffraction spread to all

areas of the image of the 220 nm defect shown in Fig. 4(b), the defect shape could not be recognized with certainty. For the 130 nm defect, the diffraction intensity was almost the same as that of the sample without the defect. This signal was found to be speckle diffraction from the substrate roughness, which overlapped and hid the defect signal in the background. Figure 5 shows the diffraction signal profile of the indicated area shown in Fig. 4(a) as a white square. The center signal of the diffraction profile included the speckle noise signal of the fringed shape. The outside impulse signals were caused by the CCD camera noise. The profile of the 130 nm defect (dark-gray solid line) was similar to that of the image with no defect (dotted line), because the signal from such a small defect was hidden by the speckle noise.

The speckle noise was observed in the blank area with this mask. However, speckle noise was not observed in the other mask shown in Fig. 6. The exposed region was also a blank region without defects, where no speckle noise was recorded. The speckle signal was thus strongly dependent on the surface roughness, and would therefore degrade the detection limit size and precision of the defect characterization of the CSM system. George et al. reported that this speckle noise affects the line edge roughness.²⁸⁾ As a result, the surface should be smooth not only for multilayer reflectivity, but also for the aerial image quality. From the point of view of roughness evaluation, the CSM system was able to evaluate the actinic surface roughness of mask blanks precisely because it recorded the substrate speckle clearly. In comparison with another method using a photodiode detector^{29,30)}, the CSM can record the two-dimensional speckle profile with a better S/N ratio, and evaluate the effect of speckle on the aerial image.

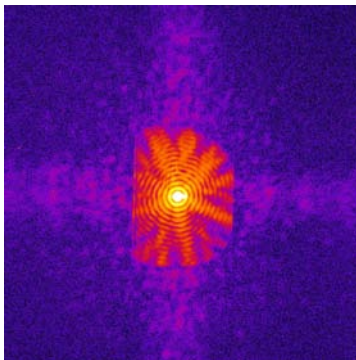


Fig. 3. Diffraction image with a programmed phase defect with 420 nm width and 7 nm height. The intensity is shown in log scale.

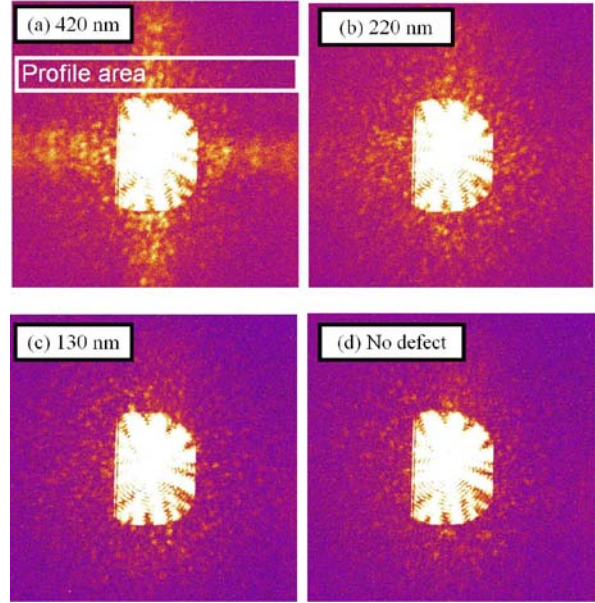


Fig. 4. Diffraction images of programmed phase defects of (a) 420, (b) 220, and (c) 130 nm width, and (d) an image without a defect. The intensity is shown on a linear scale.

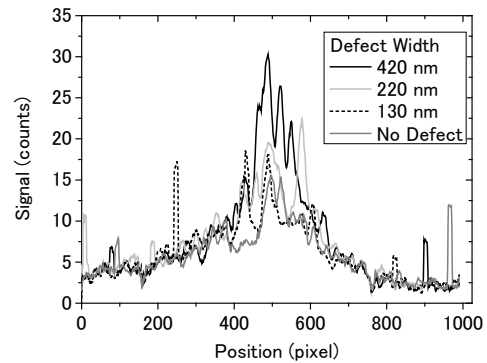


Fig. 5. Intensity profile of the diffraction signals for the defects. The horizontal axis indicates the image position shown in Fig. 4(a).

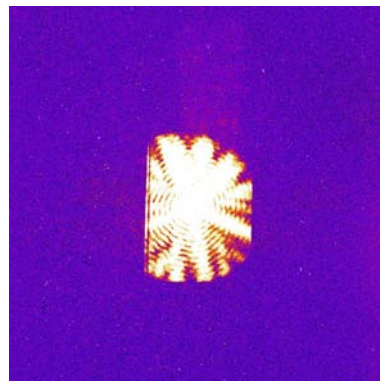


Fig. 6. Diffraction image of a mask blank without defects. There is no speckle noise signal.

Discussion

4.1 Concept of micro-CSM system

The CSM system can evaluate defect properties

without any influence from the imaging optics. The CSM measured the defect width and height from the diffraction signals. However, small defect signals were hidden by the speckle noise because the defect signal was weak relative to the strong speckle noise from the surface roughness. Also, the illumination signal was 10^4 times stronger than the defect signal, making bright-field observation difficult. To minimize the noise and maximize the defect signal intensity, the illumination size should be as small as the defect size, which improves the defect-to-illumination size ratio. Thus, we propose the micro-CSM system shown in Fig. 7. The micro-CSM system has almost the same optics as the CSM system. The specific additional component in the micro-CSM is a Fresnel zone plate (FZP) that focuses the illumination onto a small phase defect. The FZP has an off-axis zone aperture, as shown in Fig. 7. Also, the diffraction from the defect transmits a rectangular aperture to the FZP membrane, which is recorded with a CCD camera directly. The target defect size of the micro-CSM system is 20 nm in width and 1 nm in height.

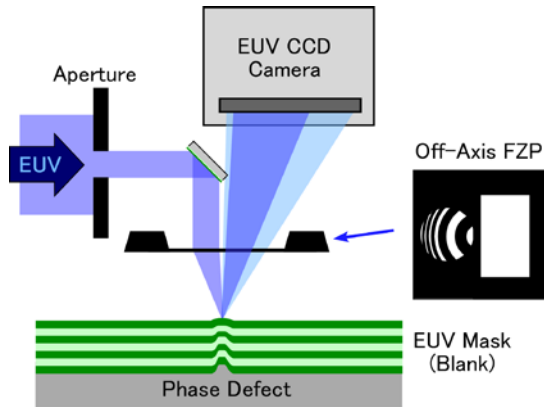


Fig. 7. Schematic view of micro-CSM system. Monochromatized EUV light is focused onto a defect by an off-axis Fresnel zone plate.

4.2 Simulation of diffraction intensity profile

We simulated the diffraction signal from the defect with various illumination sizes to optimize the micro-CSM system. This simulation was based on scalar diffraction theory. The simulation conditions are as follows. The working wavelength was 13.5 nm. The illumination was focused using optics with an NA of 0.17. The angle of incidence was normal. The reflection from the multilayers on the substrate was assumed to be a reflection from a single layer for simplicity. The phase defect had a symmetrical circular shape, and a top-hat phase distribution. For speckle noise calculations, the reflection layer had a surface roughness of 0.15 nm (rms).

Figure 8 shows diffraction images from a phase defect with a diameter of 50 nm and a height of 1 nm. The illumination sizes were varied, with

diameters of (a) 1 μm and (b) 100 nm. The intensity is shown in log scale. The maximum NA position of the image was 0.5. The strong signal at the center originated from the illumination. The weak signal of the outside ring was a diffraction signal that came from the defect. For the 1- μm -diameter case, the speckle noise overlaps the defect signal. For the 100 nm case, there was no speckle noise, and the defect signal was recorded clearly. The intensity profiles of these images are shown in Fig. 9. The horizontal axis indicates the NA position at the detector, and the vertical axis indicates the signal intensity. The NA position corresponds to the diffraction angle. The intensities of the 1- μm - and 100-nm-diameter cases were normalized for the same illumination intensity. In the 1 μm case, the illumination peak signal was two orders stronger than that in the 100 nm case, while the defect signal was two orders weaker. The signal range spanned seven orders of magnitude, from 10^{-5} to 10^2 . Because a typical CCD camera has a dynamic range of 4 orders of magnitude, it is difficult to record the defect signal using a CCD camera. Also, the speckle signal overlapped the defect signal, which was the same as that shown in Fig. 5. In the 100-nm-diameter case, the illumination and diffraction signal were recordable within three orders of magnitude, and no speckle signal was recorded. We thus chose the illumination size of 100 nm for the micro-CSM system, allowing the characterization of the defect using the CCD image.

We also simulated the diffraction signal profile from various sizes of defects with the 100-nm-diameter illumination. Figure 10(a) shows the diffraction signals from a defect with various heights ranging from 0 to 3 nm, while the width was fixed at a diameter of 50 nm. Figure 10(b) shows the diffraction for various diameters, ranging from 0 to 60 nm, while the height was fixed at 1 nm. The horizontal axis indicates NA positions at the detector same as Fig. 9. The illumination was assumed to have a top-hat intensity distribution for simplicity. Because the illumination size and the defect size were comparable for these conditions, the center signal decreases over 10% by destructive interference with the shallow 1-nm-height defect. Under these conditions, the defect position was detectable from the intensity change of the illumination signal. This was very useful for location of the defect position. Because the ABI tool has a low spatial resolution of 500 nm, scanning of the illumination using the micro-CSM system is necessary to characterize defects that are detected by the ABI tool. The diffraction profile for a tiny defect with a width of 20 nm was clearly different to the no-defect case. Thus, the detection limit of a defect signal using the micro-CSM is better than a defect with 20 nm width and 1 nm height, if the mask has

a low surface roughness of 0.15 nm (rms) and the sensor noise is negligible. Because the diffraction signals are very sensitive to the defect height and width, the micro-CSM can characterize the defect properties precisely.

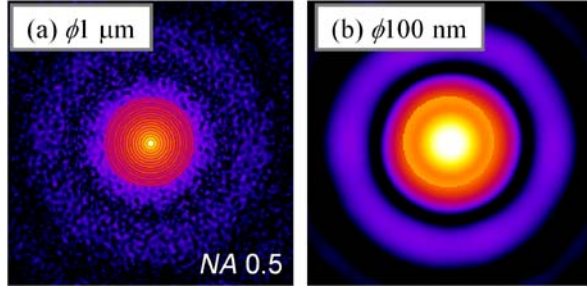


Fig. 8. Calculated diffraction images with illumination diameters of (a) 1 μm and (b) 100 nm. The defect has 50 nm diameter and 1 nm height. The substrate has 0.14 nm (rms) surface roughness.

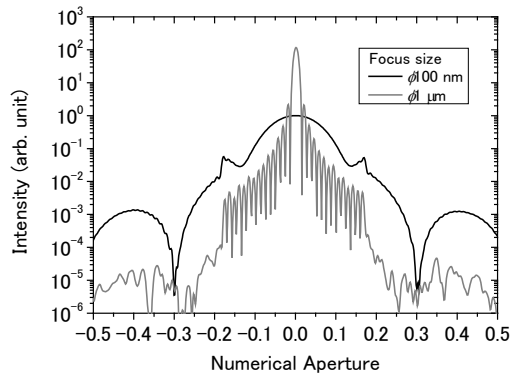


Fig. 9. Intensity profiles of the calculated diffraction images shown in Fig. 8.

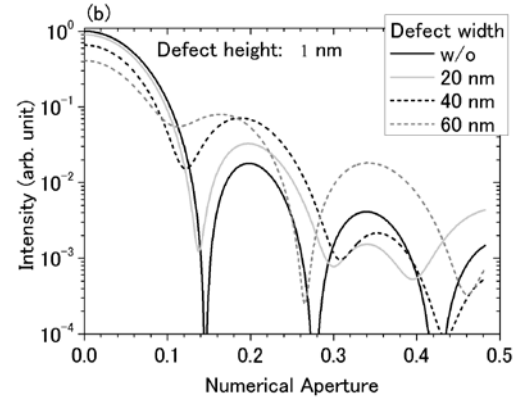
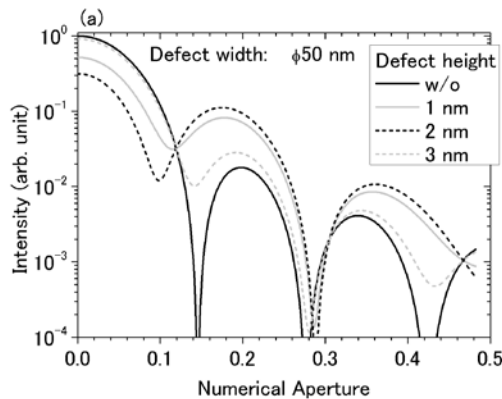


Fig. 10. Diffraction intensity profile with defects with various (a) widths and (b) heights.

Conclusions

Programmed phase defects on EUV mask blanks were observed using the CSM system. The CSM successfully detected phase defects down to a width of 220 nm, and we evaluated the defect width and height precisely for the 420 nm defect. This defect property information is important for repair using defect hiding and compensation methods with absorber pattern modulation. However, because the illumination diameter was as large as 5 μm , the defect signal was too weak. Also, the speckle noise signals from the substrates hid the defect signals for defect sizes smaller than 200 nm. We therefore proposed the micro-CSM system, which focuses the illumination onto the defect with a 100 nm diameter. Simulation results show that the micro-CSM system can record the diffraction signal clearly from a defect with a diameter of 20 nm and a height of 1 nm. As a result, the micro-CSM can characterize the defect properties. In a future work, we will construct the micro-CSM, and collect diffraction images from various programmed defects and actinic defects. The database relations between the ABI signals and the micro-CSM signals will help to enhance the ABI performance. The diffraction images recorded using the micro-CSM provides raw defect data, which is essential for defect compensation.

Acknowledgements

This work is a part of re-contracted research from the EUVL Infrastructure Development Center (EIDEC). EIDEC programs are supported by the New Energy and Industrial Technology Development Organization (NEDO).

References

- [1] Y. Kamaji, K. Takase, T. Yoshizumi, T. Sugiyama, T. Uno, T. Watanabe, and H. Kinoshita: Jpn. J. Appl. Phys. 48 (2009) 06FA07.
- [2] Y. Kamaji, T. Uno, K. Takase, T. Watanabe, and H. Kinoshita: Jpn. J. Appl. Phys. 49 (2010) 126502.
- [3] H. J. Kwon, J. Harris-Jones, R. Teki, A. Cordes, T. Nakajima, I. Mochi, K. A. Goldberg, Y. Yamaguchi, and H. Kinoshita: Proc. SPIE 8166 (2011) 81660H.

- [4] I. Mochi, K. A. Goldberg, B. La Fontaine, A. Tchikoulaeva, and C. Holfeld: Proc. SPIE 7636 (2010) 76361A.
- [5] I. Mochi, K. A. Goldberg, R. Xie, P. Yan, and K. Yamazoe: Proc. SPIE 7969 (2011) 79691X.
- [6] S. Huh, P. Kearney, S. Wurm, F. Goodwin, K. A. Goldberg, I. Mochi, and E. Gullikson: Proc. SPIE 7271 (2009) 72713J.
- [7] T. Terasawa, Y. Tezuka, M. Ito, and T. Tomie: Proc. SPIE 5446 (2004) 804.
- [8] T. Terasawa, T. Yamane, T. Tanaka, T. Iwasaki, O. Suga, and T. Tomie: Jpn. J. Appl. Phys. 48 (2009) 06FA04.
- [9] T. Terasawa, T. Yamane, T. Tanaka, O. Suga, and T. Tomie: Jpn. J. Appl. Phys. 49 (2010) 06GD02.
- [10] T. Terasawa, T. Yamane, T. Kamo, T. Tanaka, and O. Suga: Proc. SPIE 7969 (2011) 79690V.
- [11] T. Shoki, M. Mitsui, M. Sakamoto, N. Sakaya, M. Ootsuka, T. Asakawa, T. Yamada, and H. Mitsui: Proc. SPIE 7636 (2010) 76360U.
- [12] A. J. Kadaksham, B. Lee, M. House, T. Laursen, B. Niekrewicz, and A. Rastegar: Proc. SPIE 7969 (2011) 79690Z.
- [13] C. H. Clifford, T. T. Chan, and A. R. Neureuther: J. Vac. Sci. Technol. B 29 (2011) 011022.
- [14] P. Yan: Proc. SPIE 7488 (2009) 748819.
- [15] T. Harada, J. Kishimoto, T. Watanabe, H. Kinoshita, and D. G. Lee: J. Vac. Sci. Technol. B 27 (2009) 3203.
- [16] H. Kinoshita, T. Harada, M. nakasuji, Y. Nagata, and T. Watanabe: Microelectron. Eng. 88 (2011) 2000.
- [17] T. Harada, M. Nakasuji, M. Tada, Y. Nagata, T. Watanabe, and H. Kinoshita: Jpn. J. Appl. Phys. 50 (2011) 06GB03.
- [18] T. Harada, M. Nakasuji, T. Kimura, Y. Nagata, T. Watanabe, and H. Kinoshita: Proc. SPIE 8081 (2011) 80810K.
- [19] T. Harada, M. Nakasuji, T. Kimura, T. Watanabe, H. Kinoshita, and Y. Nagata: J. Vac. Sci. Technol. B 29 (2011) 06F503.
- [20] T. Watanabe, T. Haga, M. Niibe, and H. Kinoshita: J. Synchrotron Radiat. 5 (1998) 1149.
- [21] J. Miao, D. Sayre, and H. N. Chapman: J. Opt. Soc. Am. A 15 (1998) 1662.
- [22] J. Miao, P. Charalambous, J. Kirz, and D. Sayre: Nature 400 (1999) 342.
- [23] J. Miao, T. Ishikawa, E. H. Anderson, and K. O. Hodgson: Phys. Rev. B 67 (2003) 174104.
- [24] Y. Nishino, J. Miao, and T. Ishikawa: Phys. Rev. B 68 (2003) 220101.
- [25] J. M. Rodenburg and H. M. L. Faulkner: Appl. Phys. Lett. 85 (2004) 4795.
- [26] P. Thibault, M. Dierolf, A. Menzel, O. Bunk, C. David, and F. Pfeiffer: Science 321 (2008) 379.
- [27] Y. Takahashi, A. Suzuki, N. Zettsu, Y. Kohmura, Y. Senba, H. Ohashi, K. Yamauchi, and T. Ishikawa: Phys. Rev. B 83 (2011) 214109.
- [28] S. A. George, P. P. Naulleau, I. Mochi, F. Salmassi, E. M. Gullikson, K. A. Goldberg, and E. H. Anderson: J. Vac. Sci. Technol. B 28 (2010) C6E23.
- [29] N. Kandaka and K. Murakami: PF News 26 (2008) 22 [in Japanese].
- [30] M. Hosoya, N. Sakaya, O. Nozawa, Y. Shiota, S. Shimojima, T. Shoki, T. Watanabe, and H. Kinoshita: Jpn. J. Appl. Phys. 46 (2007) 6128.

Chemical Reaction Analysis of EUV CA Resist using SR Absorption Spectroscopy

Takeo Watanabe, Yuichi Haruyama, Daiju Shiono*, Kazuya Emura,
Takuro Urayama, Testuo Harada, and Hiroo Kinoshita

*Center for EUVL, Laboratory of Advanced Science and Technology for Industry,
University of Hyogo*

3-1-2 Kouto, Kamigori, Ako-gun, Hyogo 678-1205, Japan

** Tokyo Ohka Kogyo Co., Ltd.*

1590 Tabata, Samukawa, Koza, Kanagawa, 253-0114, Japan

It had been reported that tri-phenylsulfonium cyclo(1,3-perfluoropropanedisulfone) imidate (TPS-IMIDATE) as a photo acid generator has approximately four times faster sensitive rather than tri-phenylsulfonium perfluorobutanesulfonate (TPS-PFBS) under the EUV exposure. In this paper, we discussed the differences of the sensitivity and the chemical reaction between TPS-IMIDATE and TPS-PFBS, on the basis of the EUV-induced analysis of the SR absorption spectroscopy. From the analysis of the SR absorption spectroscopy, F and C atoms in the anion of TPS-IMIDATE decomposed rather than that of TPS-PFBS. The sensitivity advantage of TPS-IMIDATE might own to the anion decomposition reaction. The anion decomposition reaction might be originated to the photo-excitation of the photoacid generator. The anion of TPS-IMIDATE decomposed to smaller molecule and the sensitivity becomes higher.

Keyword: EUVL, chemically amplified resist, photoacid generator, decomposition of anion of PAG, SR absorption spectroscopy

1. Introduction

Extreme ultraviolet lithography (EUVL) [1] is a promising lithographic technology which should begin to transfer to the production line for semiconductor electronics from the 25-nm node around 2013. The first top issue of EUVL is to achieve the EUV source power of 180 W at the intermediate focus position, when the resist sensitivity is assumed to be 10 mJ/cm². If the much higher sensitive resist can be performed, the EUV source power could be relaxed. In addition, the third issue of EUVL is to develop the EUV resist which has the sensitivity of 10 mJ/cm² and the line width roughness (LWR) of smaller than 2 nm (3 σ) because of the trade of relationship between the resolution, the LWR, and the sensitivity, so called “RLS” trade off. The photon number which requires for the patterning in EUV is approximately one order smaller than those in KrF

and ArF lithography. Thus, in order to achieve low LWR, the yield of the acid should increase. In addition, to achieve the high sensitivity and the low LWR, the acid production yield from the photoacid generators in the chemically amplifies resist [2-4] should increase.

In focusing, the production acid yield, the chemical reaction analysis on the basis of EUV photo irradiation should be performed in the basic study.[5-9]

In the previous report, for resist A, the peak at the absorbance at 1156 cm⁻¹ in the fourier transform infrared (FT-IR) spectra increased after EUV exposure.[7-9] However, there was no change in the FT-IR spectra of resist B before and after EUV exposure. As a results of the electron orbital calculation using perturbation theory by the software code Gaussion03 [10], the peak at approximately 1156 cm⁻¹ in FT-IR spectra of resist A corresponds to C-F bonding of the anion of

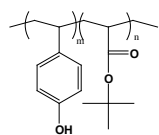
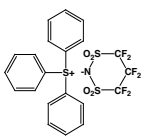
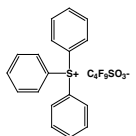
TPS-IMIDATE. As a result, the outgassing measurements and the FT-IR spectra measurements indicated that the EUV-induced reaction of TPS-IMIDATE occurred more efficiently than that of TPS-PFBS. To clarify the difference of the anion decomposition, the analysis using SR spectroscopy is performed. This paper focused on the chemical reaction analysis of the model chemically amplified resists by the SR absorption spectroscopy.

2.Experimental

2.1. Materials

The model resists which were employed in this study are shown in Table 1. The resists A and B is employed poly (hydroxystyrene-co-t-butylacrylate) as the base polymer, and propyleneglycol monomethyletheracetate (PGMEA) as a solvent. Resists A and B employed triphenylsulfonium cyclo(1,3- perfluoro propanedisulfone) imidate (TPS-IMIDATE) and triphenylsulfonium perfluorobutanesulfonate (TPS-PFBS) as the photoacid generator, respectively. The PAG content is approximately 30 wt% of the base polymer to increase the detection S/N ratio of the anion decomposition species from the PAG in the SR spectroscopy measurement before and after EUV exposure. The resist solution was spin coated on a 4-inches silicon wafer to be a 50-nm-thickness. The film thickness was measured by Nanometrics 6100A (NANOmetrics). The prebake conditions was carried out on a hot plate at the temperature of 130°C in the time period of 90 s.

Table 1. Model resist material

Sample	Resist A	Resist B
Resin		
PAG		
Solvent	PGMEA	

2.3. SR Absorption Experiment

The SR absorption spectroscopy measurements were performed at the end station of the BL07B beamline at the NewSUBARU synchrotron radiation facility. The short undulator was employed as a light source of this beamline. The configuration setup of the BL07B is shown in Fig.1. The beamline consists of three glancing mirrors such as M0, M1 and M2, the monochromator (G), the entrance (S1) and exit (S2) slits and the end station exposure and analyzing chambers. The loadlock chamber was adapted to these chambers to exchange the sample. The photography of the BL07B beamline and the end station are shown in Figs.2(a) and 2(b). The variable line spacing plane gratings (VLSPG) were employed as monochromator. Three density types such as 600, 1200, and 2400 lines/mm were installed in the monochromator vacuum chamber. The photon energy region is from 80 eV and 800 eV in the

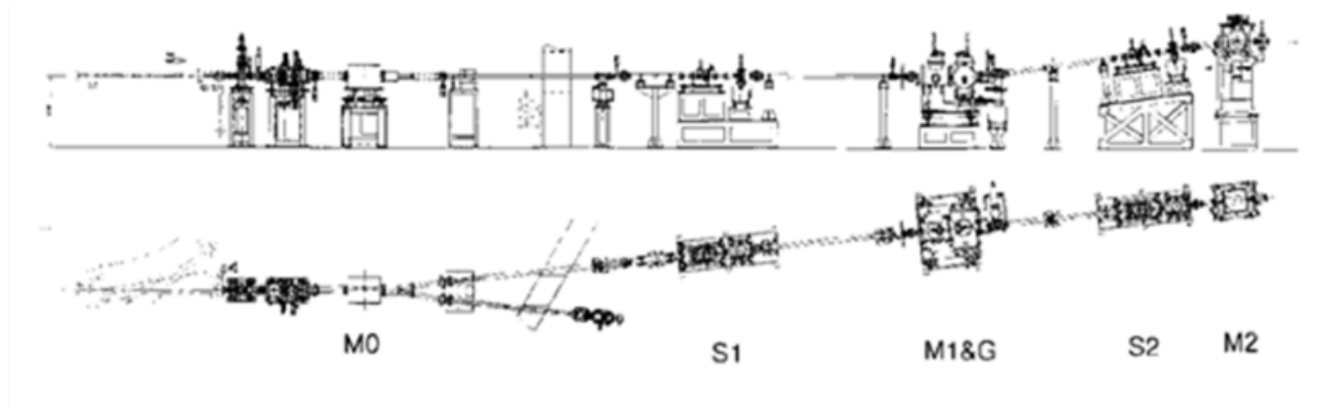


Fig. 1 System configuration of the BL07B beamline.

SR spectroscopy. The exit slit size is $20\ \mu\text{m(H)} \times 20\ \mu\text{m(V)}$ and the SR light spot size on a sample is $1\ \text{mm(H)} \times 1\ \text{mm(V)}$. The energy resolution $E/\Delta E$ is approximately 1000. The photon flux of the photon energy of 91.8 eV ($\lambda=13.5\ \text{nm}$) is approximately 3.0×10^{11} photons/s/100mA.

The absorption signal was obtained from the ratio of the photocurrent from the sample to the photocurrent from the gold mesh. The total energy resolution was $\sim 0.5\ \text{eV}$. The photocurrent was measured by the electrometer (6514, Keithley).

For the absorption measurement of F 1s core level, the measured energy region is 685-735 eV and 2400 lines/mm VLSPG was employed with the undulator gap of 52.0 mm. For the absorption measurement of C 1s core level, the measured energy region is 280-330 eV and 1200 lines/mm VLSPG was employed with the undulator gap of 48.0 mm. For the absorption measurement of N 1s core level, the measured energy region is 390~440 eV and 2400 lines/mm VLSPG was employed with the undulator gap of 51.0 mm. The electron current generated on the sample is measured in the SR absorption experiment during the SR light exposure.

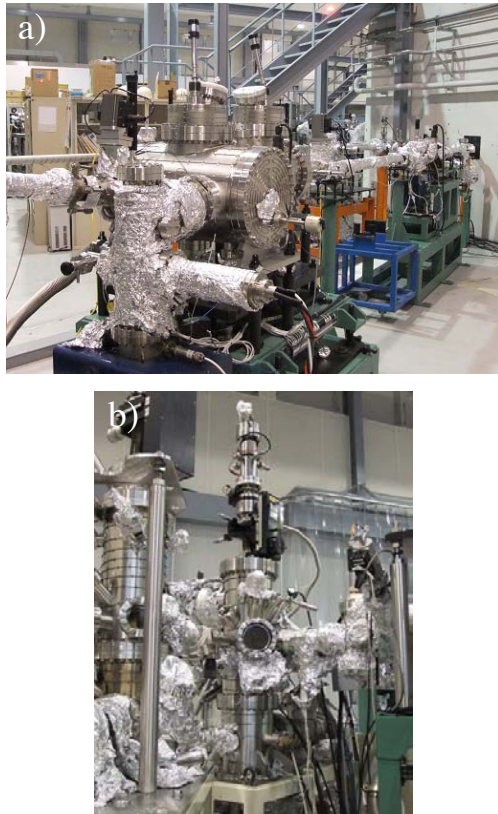


Fig. 2 Photographs of (a) BL07B beamline and (b) end station.

3. Results and Discussions

3.1. SR Absorption Spectra

SR absorption spectra of F 1s core level at the photon-energy ranges of 685-735 eV of resists A and B are shown in Figs. 3 (a) and 3(b), respectively. For resist A, the absorption at the photon energy of 697 eV decreased when the EUV exposure dose increased and the absorption disappeared at the EUV dose of $104\ \text{mJ/cm}^2$. For resist B, the absorption at the photon energy of 697 eV decreased when the EUV exposure dose increased. However, the absorption signal remained at the EUV exposure dose of $104\ \text{mJ/cm}^2$. The EUV exposure dose dependency of the absorption of F atoms at the photon energy of 697 eV is shown in Fig. 4. The decomposition of F atoms in the anion of the TPS-IMIDATE has easier to decompose than that of TPS- PFBS.

As the results, F atoms decomposition speed of the TPS-IMIDATE is faster than that of the TP- PFBS.

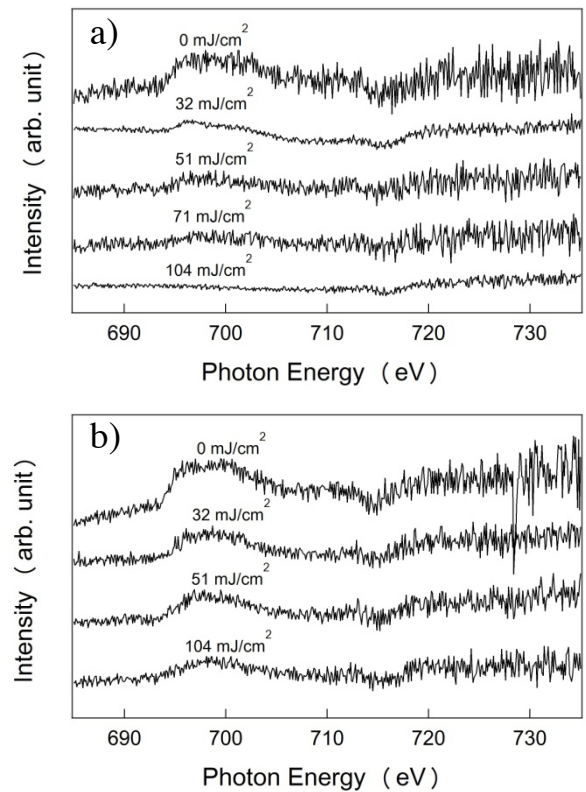


Fig. 3 Absorption spectra of F 1s core level in the anions of (a) TPS-IMIDATE and (b) TPS- PFBS.

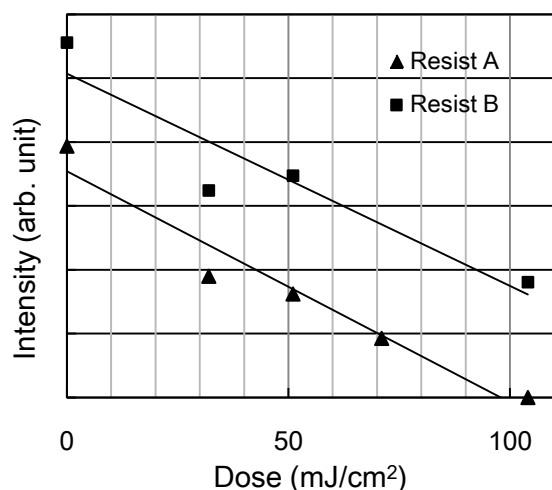


Fig. 4 EUV exposure dose dependency of the absorption of F 1s core level at the photon energy of 697 eV.

Absorption spectra of C 1s core level at the photon-energy ranges of 280-330 eV of resists A and B are shown in Figs. 5 (a) and 5(b), respectively.

For resist A, the absorption at the photon energy of 287 eV had no change. Thus, it means that the π -bonding of the benzyl group of the base polymer has no change. However, the absorption at the photon energy of 290 eV decreased after the EUV exposure. It means that the anion of the σ -bonding of the anion of TPS-IMIDATE decomposed under the EUV exposure.

For resist B, the absorption at the photon energy of 290 eV had no change before and after the EUV exposure. It means that the anion of the σ -bonding of the anion of TPS-IMIDATE decomposed under the EUV exposure.

Absorption spectra of N 1s core level at the photon-energy ranges of 390-440 eV of resist A is shown in Fig.6. the absorption at the photon energy of 405 eV decreased under the EUV exposure. And the photo-energy of 403 eV increased under EUV exposure and the chemical shift was observed. It means that N atoms in the anion of TPS-IMIDATE decomposed and reconstructed under the EUV exposure.

As the results of the SR spectroscopy, the σ -bonding of the anion of TPS-IMIDATE decomposed to the small molecule size and the acid diffusion length might become large. Thus the sensitivity of resist A might become

much higher than that of resist B.

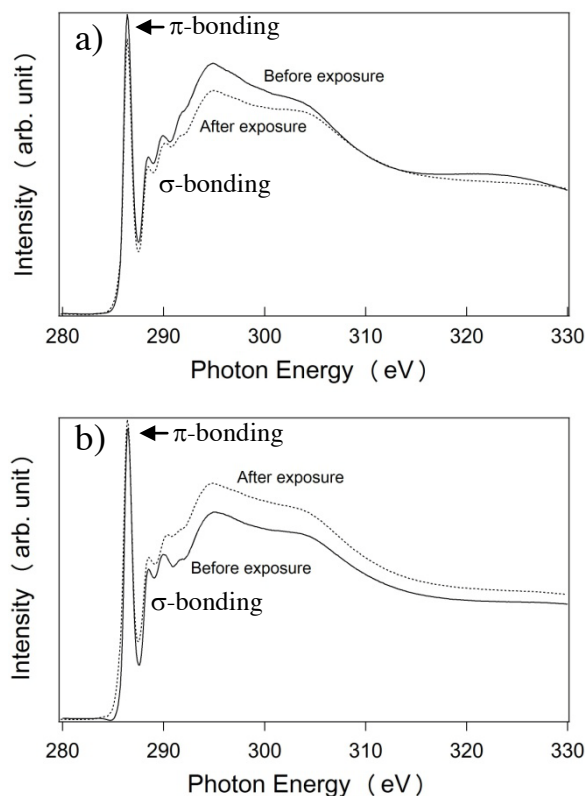


Fig. 5 Absorption spectra of C 1s core level of the anions of (a) TPS-IMIDATE and (b) TPS- PFBS.

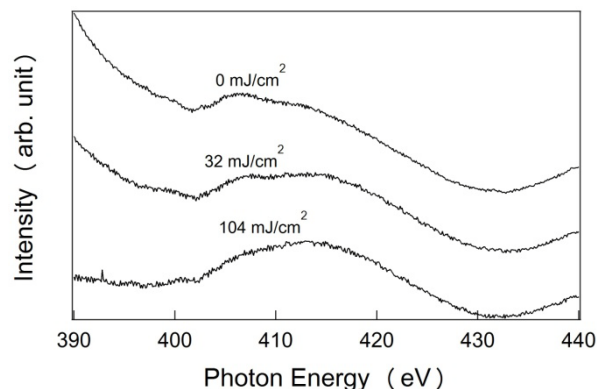


Fig. 6 Absorption spectra of N 1s core level in the TPS-IMIDATE anion.

4. Conclusion

As the analysis results of the SR spectroscopy measurement, it was confirmed that the decomposition reaction begin to occur by the absorption by the EUV photons at F

atoms in the anion of TPS-IMIADTE and the anion molecular size becomes smaller than the original one. However, for resist B, only F atoms in the anion of TPS-PFBS decomposed and the molecular size of the anion did not dramatically change. Since the anion size of TPS-IMIDATE might be much smaller than that of TPS-PFBS, the acid diffusion length in resist A might become larger than that in resist B.

To achieve the low LWR, it had introduced generally that the diffusion length of PAG should decreased by increasing the molecular size of the anion of PAG. However, for the anion PAG which include F atoms, from the results of the SR spectroscopy, F atoms might decompose under EUV exposure. Therefore, since the anion of the PAG which includes F atoms should be analyzed carefully if the decomposition reaction of the anion of PAG would occur or not.

The SR absorption spectroscopy might be a powerful analysis method to analyze the decomposition reaction of the anion of PAG. To satisfy the specification of the EUV resist which require for high volume manufacturing, all the chemical reaction should be taken in account.

References

1. H. Kinoshita, K. Kurihara, Y. Ishii and Y. Torii, *J. Vac. Sci. & Technol.*, **B7** (1989) 1648.
2. H. Ito, C. G. Willson, and J. M. J. Frechet, *Digest of Tech. Papers 1982 Symp. VLSI Tech.*, (1982) 86.
3. H. Ito and C. G. Willson, *Polym. Eng. Sci.*, **23** (1983) 1012.
4. H. Ito, G. Breyta, D. Hofer, R. Sooriyakumaran, K. Petrillo, and D. Seeger, *J. Photopolym. Sci. Technol.*, **7** (1994) 433.
5. T. Watanabe, K. Hamamoto, H. Kinoshita, H. Hada and H. Komano, *Jpn. J. Appl. Phys.* **43** (2004) 3713.
6. H. Hada, T. Watanabe, H. Kinoshita and H. Komano, "Outgassing Analysis in EUV Resist" *J. Photopolym. Sci. Technol.*, **18** (2005) 475.
7. T. Watanabe, H. Hada, S. Y. Lee, H. Kinoshita, K. Hamamoto and H. Komano, *Jpn. J. Appl. Phys.*, **44** (2005) 5866.
8. Takeo Watanabe, Hideo Hideo, Hiroo Kinoshita, Yuzuru Tanaka, Hideaki Shiotani, Yasuyuki Fukushima and Hiroshi Komano, *Proc. SPIE*, **6153** (2006) 615343-1.
9. Takeo Watanabe, Hideo Hada, Yasuyuki Fukushima, Hideaki Shiotani, Hiroo Kinoshita and Hiroshi Komano, *Synchrotron Radiation Instrumentation: Ninth International Conference*, AIP **879** (2007) 1470.
10. Gaussian03 electron orbital calculation software is informed in URL:<http://www.gaussian.com/home.htm>.

Plasma-Debris Sputter Resistant X-ray Mirror

S. Amano, T. Inoue, T. Harada
LASTI/UH

Abstract

A diamond-like carbon (DLC) mirror, used as a grazing incident mirror in a plasma X-ray source, exhibits a high resistance to plasma debris sputtering. The erosion rate due to plasma debris sputtered at the incident debris angle of 20° was measured using a laser-produced Xe plasma source developed by the authors. The results indicate that the DLC film has a 5- and 15-fold higher sputtering resistance compared to films made of the traditional mirror materials Ru and Au, respectively. Because the DLC mirror retains a high sputtering resistance to Sn ions, it may be effective in Sn plasma source applications. We conclude that a grazing incident X-ray mirror coated with DLC can be of use as a plasma debris sputtering resistant mirror.

Plasma X-ray sources, which produce radiation from laser-produced plasmas (LPP) or discharge-produced plasmas (DPP), find use in various industrial applications. However, along with X-rays, the plasmas in these sources emit debris consisting of ions, neutral atoms, various fragments, vapor and so forth. Such debris damages mirrors located near the plasma, quickly degrading their reflectivity. Because the amount of plasma debris increases in proportion to the X-ray generating power, the debris problem is a critical issue in high-power plasma sources for industrial applications. We propose a new approach to mitigate debris effects in plasma X-ray sources, namely the use of debris resistant mirrors that suffer reduced debris damage as compared with traditional mirrors.

In our lab, we developed a laser-produced plasma X-ray source (LPX), which employs a solid Xe target. This device has demonstrated continuous X-ray generation at 5–17 nm with an average power of 20 W. A diamond-like carbon (DLC) coating, also developed in our laboratory, was deemed a good candidate for the mirror material, owing to its high hardness. In this work, we measured the erosion rate due to debris sputtering in the plasma source. The results were compared with similar experiments with mirrors coated with Ru and Au films, which are typically used as mirror coating materials.

The LPX consists of a system that supplies a solid Xe-target and a drive laser. The target supply system comprises a cylindrical drum filled with liquid nitrogen, so its copper surface is at liquid nitrogen temperature. Xe gas blown onto this surface condenses to form a solid Xe layer. The solid Xe layer-coated drum rotates about the vertical axis, simultaneously moving up and down vertically during rotation. The resultant spiral motion ensures that a fresh target surface is continuously supplied for every laser shot. The drive laser is a slab laser with an average power of 100 W and a pulse repetition rate of 320 Hz. The laser pulses ($\lambda = 1064$ nm) with a pulse width

of 20 ns are focused on the solid Xe-target, continuously producing plasma.

We used a quartz crystal microbalance (QCM) to measure the erosion rate of the DLC films after sputtering with Xe plasma debris from the LPX. As such debris bombards a test film that is coated onto the QCM, atoms are ejected from the surface of the film, changing the resonant frequency of the QCM. Mass loss in the film can be deduced from this frequency change, and erosion rates of the film can be calculated directly. The experimental setup is shown in Fig. 1.

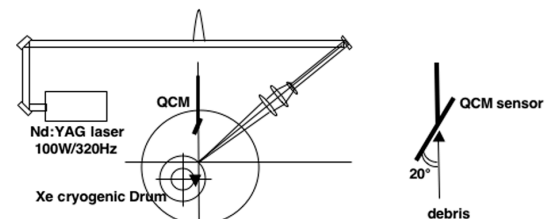


Figure 1. Experimental setup.

The drum target system and the QCM were installed in a vacuum chamber (pressure of 0.2 Pa), while drive laser pulses coming through a window were focused perpendicularly onto the target by a lens. The coated QCM was placed 73 mm from the plasma at a 45° angle with respect to the incident laser beam. Its sensor surface was tilted at a 20° angle with respect to the incident debris axis, thus forming a grazing incidence mirror. Test films coated on the quartz sensors consisted of DLC, Ru and Au, with a coating thickness of 500, 100, and 100 nm, respectively. After laser irradiation of the films for 2–10 min at 320 Hz, we used the QCM to monitor total erosion rates during extended multi-shot plasma operation.

The measured erosion rates of the DLC, Ru and Au films at an incident debris angle of 20° are shown in Fig. 2. We see a decreased erosion rate with increasing binding energy, and the erosion rate ratio is DLC : Ru : Au = 1 : 5 : 15. We also performed an erosion calculation using the SRIM software. SRIM can calculate a sputtering yield Y_{sputt} for normal carbon, Ru and Au. For a given sputtering yield Y_{sputt} (atoms / ion) and an ion flux F_{ion} (ions), the erosion rate of a mirror film ΔT (cm / shot) can be written as:

$$\Delta T = Y_{\text{sputt}} \cdot F_{\text{ion}} \cdot \frac{m}{\rho},$$

where m is the mirror mass (g) and ρ is the mirror density (g/cm²).

The plasma debris emitted from the LPX was studied in detail previously, with the results indicating the debris predominantly consists of fast ions. The time of flight (TOF) Xe ion signal as detected by a Faraday-cup indicated the ion energy is less than 6 keV, and the ion flux at the QCM was calculated to be about 6×10^{11} /shot. Using this result as the ion flux F_{ion} and the calculated sputtering yield Y_{sputt} in the eq., we can predict the erosion rates ΔT for the three films. The ratios of these calculated values are C : Ru : Au = 2 : 6 : 16, which are close to the experimental results of 1 : 5 : 15. Compared with the calculated erosion rate for C, the measured value for the DLC is slightly smaller. This difference may be due to the different types of carbon involved: high hardness DLC in the experiment vs. normal carbon (graphite) in the calculation.

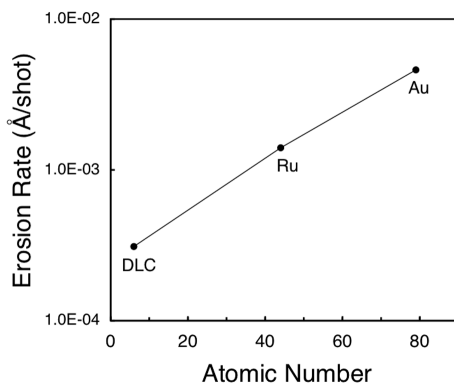


Figure 2. Erosion rate of the DLC, Ru, and Au films as measured by QCM with a debris incidence angle of 20°.

Sn DPP X-ray sources are currently used as extreme ultraviolet lithography (EUVL) sources in the industrial mass production of semiconductors. These sources emit X-rays at a wavelength of 13.5nm, and employ grazing incidence Ru mirrors. As shown in Fig.3, the DLC sputtering yield by Sn ions is similar to the one by Xe ions, as calculated by the SRIM code. Therefore, a DLC mirror may also be resistant to Sn sputtering. Of course, because the Sn plasma debris includes both “deposition” and “sputter” types of particles, additional debris mitigation techniques are necessary. However, we predict that a DLC mirror will enjoy a longer lifetime in a Sn plasma source.

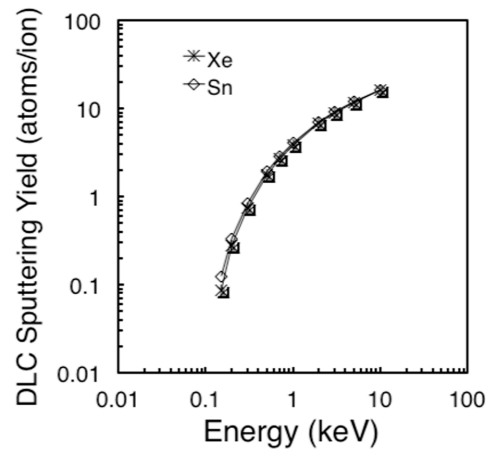


Figure 3. DLC sputtering yield by Xe and Sn ions, calculated with the SRIM code.

References

- [1] S.Amano *et al.*, Appl. Opt., **52**, pp.3845(2013).

Electronic Structure of the Fluorinated Self-Assemble Monolayer by Photoemission and Absorption Spectroscopy

Yuichi Haruyama, Makoto Okada, and Shinji Matsui

Laboratory of Advanced Science and Technology for Industry, University of Hyogo

Abstract

The electronic structure of F-SAMs (fluorinated self-assembled monolayer) thin films with different chain length was investigated by the photoelectron and absorption spectroscopy. The photoelectron spectra in the wide region and in the C 1s core-level region were measured and the chemical compositions and components of the photoelectron spectra F-SAMs thin films with different chain length were clarified. In addition, the C K-edge absorption spectra of F-SAMs thin films were measured and the several spectral features in absorption spectra of the F-SAMs thin films were assigned. Based on the results of the photoelectron and absorption spectroscopy measurements of four kinds of F-SAMs with different chain length, the electronic structure of the F-SAMs thin films is discussed.

Introduction

The study of nanoimprint lithography (NIL) [1-2] has attracted much attention for many industrial field because it is a promising method to fabricate various nanostructures with a low cost and a high throughput. In the process of NIL, the mold is usually coated with an antisticking layer to avoid resist adhesion. As an antisticking layer of nanoimprint mold, the fluorinated self-assemble monolayer (F-SAM) is used, for example. The evaluation of the F-SAM with different chain length is one of the critical issues in NIL [3]. In this study, four kinds of F-SAMs with different chain length were evaluated using the photoemission and the absorption spectroscopy.

Experiments

Four kinds of F-SAMs were prepared from a precursor $[\text{CF}_3(\text{CF}_2)_n(\text{CH}_2)_2\text{Si}(\text{OCH}_3)_3]$; $n=0, 3, 5$, and 7] as denoted FAS-3, 9, 13, and 17, respectively. All photoelectron and absorption measurements were performed on a BL7B end station at the NewSUBARU facility, University of Hyogo. The photoelectron spectra were measured in an analysis chamber mounted with a hemispherical electrostatic spectrometer (VSW Ltd, CL150). The synchrotron radiation and the Mg $K\alpha$ line were used as the excitation source and were incident at 45° with respect to the surface normal. The total energy resolutions were about 0.7 eV for the C 1s core-level regions. Gold films evaporated on copper sample holders and F-SAMs were used for the Fermi level measurements and the total energy resolution reference. Absorption spectra were measured by the total electron yield method. The total energy resolution was about 0.5 eV. The photocurrents from the sample and from a gold mesh were recorded simultaneously. The absorption signal was obtained from the ratio of the photocurrent from the sample to the photocurrent from the gold mesh.

Results

Figure 2 shows the photoelectron spectra in four kinds of F-SAMs with different chain length. The photoelectron spectrum of Si substrate is also plotted for comparison. Several peaks were observed at ~ 688 , ~ 532 , ~ 290 , ~ 100 eV, which

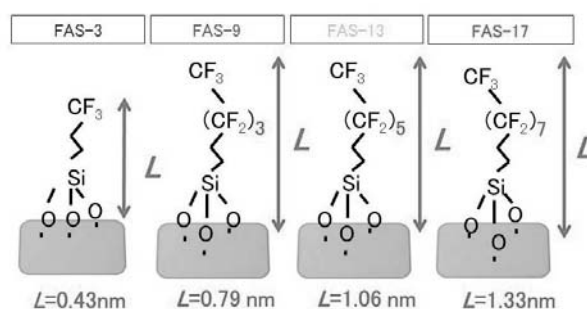


Figure 1. Four kinds of F-SAM thin films with different chain length.

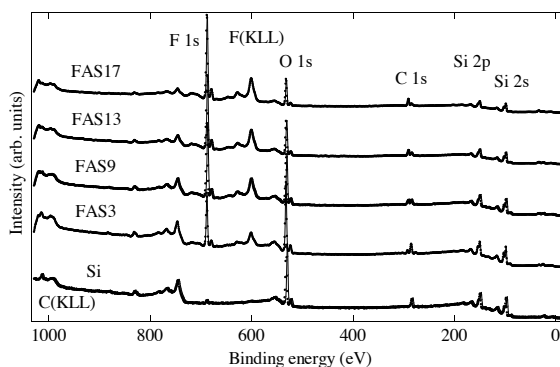


Figure 2. Wide scan of the photoelectron spectra of the four kinds of F-SAMs thin films with different chain length. The photoelectron spectra in this figure were normalized by the C 1s peak intensity.

were originated from the F 1s, O 1s, C 1s, and Si 2p electrons, respectively. With increasing the chain length, the intensity of the peak at $\sim 688\text{eV}$ increased while intensity of the peaks at ~ 532 and $\sim 100\text{eV}$ decreased. On the other hand, the intensity of the peaks at $\sim 290\text{eV}$ did not change with increasing the chain length. These indicate that the intensity of the Si substrate decreased due to the increase of thickness of F-SAM with increasing the chain length. In Figure 3, the photoelectron spectra of the C 1s core-level region in four kinds of F-SAMs with different chain length are plotted. In the photoelectron spectra of the C 1s core-level, three peaks at ~ 293 , ~ 286 , and $\sim 284.5\text{eV}$ were observed in the FAS-3 although four peaks at ~ 293 , ~ 291 , ~ 286 , and $\sim 284.5\text{eV}$ were observed in the FAS-9, 13, and 17. The intensity of the peak at 291eV increased with increasing the chain length. On the other hand, the intensity of the peaks at ~ 293 , $\sim 286\text{eV}$ did not change with increasing the chain length. From the chemical compositions of four kinds of F-SAMs with different chain length, these peaks at ~ 293 , ~ 291 , ~ 286 , and $\sim 284.5\text{eV}$ were assigned to the CF_3 , CF_2 , CH , and C-C components, respectively. Figure 4 shows the absorption spectra in four kinds of F-SAMs with different chain length. Several peaks were observed at 285 , 292 , 295 , $296\text{--}300\text{eV}$. The intensity of the peak at 292eV increased with increasing the chain length. On the other hand, the intensity of the peaks at 285 , 295 , $296\text{--}300\text{eV}$ did not change with increasing the chain length. The peaks at 292eV were assigned to the $\sigma^*(\text{C-F})$ and $\sigma(\text{CF}_2)$ components. On the other hand, these peaks at 285 , 295 , and $296\text{--}300\text{eV}$ were assigned to the $\pi^*(\text{C-C})$ and $\sigma^*(\text{C-H})$, $\sigma^*(\text{C-F})$ and $\pi(\text{CF}_3)$, and $\sigma^*(\text{C-F})$, $\sigma(\text{CF}_2, \text{CF}_3)$, $\sigma^*(\text{C-C})$ components, respectively [4]. When the incident angle of the synchrotron radiation to the sample surface was changed, no clear change of the absorption spectra was observed in four kinds of F-SAMs with different chain length. This indicates that each molecular with different chain length on the Si surface seems to be oriented randomly.

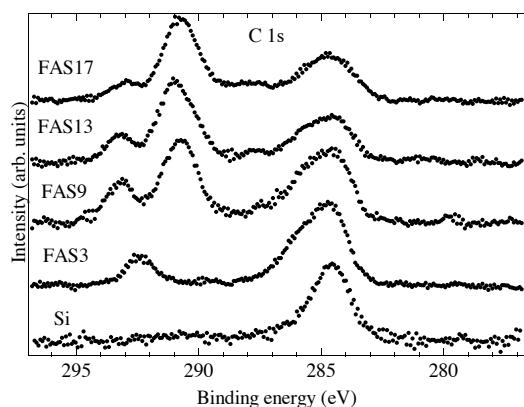


Figure 3. Photoelectron spectra of the C 1s core-level region in four kinds of F-SAMs thin films with different chain length.

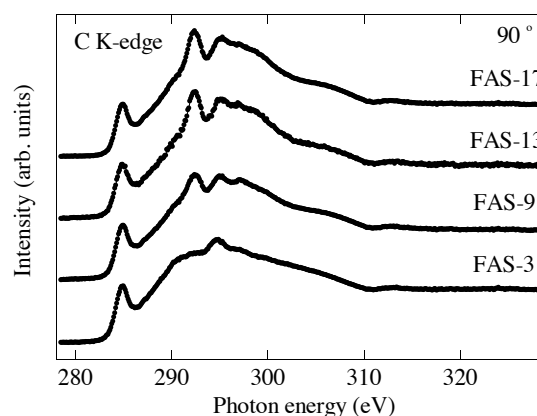


Figure 4. C K-edge absorption spectra in four kinds of F-SAMs with different chain length.

References

- [1] S. Y. Chou, P. R. Krauss, P. J. Renstrom, *Appl. Phys. Letters* **67**, 3114-3116 (1995).
- [2] K. Nakamatsu, K. Watanabe, K. Tone, H. Namatsu, and S. Matsui, *J. Vac. Sci. Technol. B* **23**, 507-512 (2005).
- [3] Y. Nakai, S. Omoto, M. Okada, K. Kanda, Y. Haruyama, and S. Matsui, *J. Photopolymer Sci. and Tech.*, **23**, 55-58 (2010).
- [4] I. Ishii, R. McLaren, A. P. Hitchcock, K. D. Jordan, Y. Choi, M. B. Robin, *CAN. J. Chem.*, **66**, pp. 2104 (1988).

Orientation evaluation of 3D-photoreactive liquid crystalline polymer structure fabricated by thermal nanoimprinting

Makoto Okada¹, Emi Nishioka², Risa Hosoda², Mizuho Kondo², Yuichi Haruyama¹,
Tomoyuki Sasaki³, Hiroshi Ono³, Nobuhiro Kawatsuki² and Shinji Matsui¹

¹Laboratory of Advanced Science and Technology for Industry, University of Hyogo, Japan

²Department of Materials Science and Chemistry, Graduate School of Engineering, Univ. of Hyogo,

³Department of Electrical Engineering, Nagaoka University of Technology

Abstract

Photoreactive liquid crystalline polymer is able to be control by linearly polarized ultra violet (LPUV) irradiation and heat treatment. We found that P6CAM, which is one of the photoreactive liquid crystalline polymers, was reoriented by thermal nanoimprinting. It is confirmed that the P6CAM molecules were reoriented parallel to the imprinted line. To examine whether the two molecular orientation directions are induced on the P6CAM film, we carried out thermal nanoimprinting using a mold with 3D structure pattern. As the results, the P6CAM 3D structure has two molecular orientation directions.

Introduction.

The photo-induced orientation of polymeric films has received much attention due to its potential use in many kinds of optical and photonics applications. P6CAM, which is a one of the photoreactive liquid crystalline polymers, exhibits a large photoinduced molecular reorientation with a high photoreactivity toward linearly polarized UV (LPUV) light and heat treatment [1, 2]. We found that P6CAM was aligned by thermal nanoimprinting[3] using line and space (L&S) pattern mold [4]. We confirmed that the P6CAM molecules were reoriented parallel to the imprinted line on the imprinted P6CAM film in the case of using a normal L&S pattern mold. If a mold with bidirectional L&S pattern is used for the thermal nanoimprint on the P6CAM, two reorientation directions of the molecules according to the bidirectional mold pattern may be induced. To confirm that, we fabricated the bidirectional line pattern mold by electron beam (EB) lithography and reactive ion etching (RIE) and then carried out thermal nanoimprinting using this mold on the P6CAM film on a glass substrate, subsequently evaluated the molecular orientation by measuring the diffraction efficiency.

Fabrication of bidirectional line pattern on P6CAM

Figure 1 shows the illustration of bidirectional line pattern. The linewidth was 2 μm . The line heights were 200 and 100 nm. The two line patterns crossed each other at right angles. The

mold was coated with an antisticking layer. We used a thin polydimethylsiloxane (PDMS) layer as the antisticking layer [5]. We carried out thermal nanoimprinting using this mold.

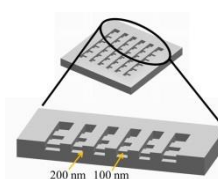


Fig. 1 Illustration of bidirectional line pattern.

The P6CAM was spin-coated on the glass substrate. The mold and P6CAM substrate were heated by 165 °C during thermal nanoimprinting. The imprinting pressure and pressing time were 15 MPa and 4 min, respectively. After thermal nanoimprinting, we observed the fabricated P6CAM structure by POM under crossed-nicols and atomic force microscopy (AFM), as shown in Fig. 2. The POM image showed the pattern contrast which means the molecular orientation related the pattern configuration. In addition, the 3D structure was successfully imprinted on P6CAM, as shown in Fig. 2(b).

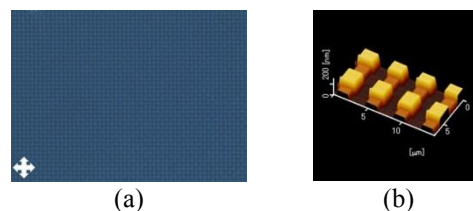


Fig. 2 (a) POM and (b) AFM images of fabricated 3D-P6CAM structure.

The measured erosion rates of the DLC, Ru and Au films at an incident debris angle of 20° are shown in Fig. 2. We see a decreased erosion rate with increasing binding energy, and the erosion rate ratio is DLC : Ru : Au = 1 : 5 : 15. We also performed an erosion calculation using the SRIM software. SRIM can calculate a sputtering yield Y_{sputt} for normal carbon, Ru and Au. For a given sputtering yield Y_{sputt} (atoms / ion) and an ion flux F_{ion} (ions), the erosion rate of a mirror film ΔT (cm / shot) can be written as:

$$\Delta T = Y_{\text{sputt}} \cdot F_{\text{ion}} \cdot \frac{m}{\rho},$$

where m is the mirror mass (g) and ρ is the mirror density (g/cm²).

The plasma debris emitted from the LPX was studied in detail previously, with the results indicating the debris predominantly consists of fast ions. The time of flight (TOF) Xe ion signal as detected by a Faraday-cup indicated the ion energy is less than 6 keV, and the ion flux at the QCM was calculated to be about 6×10^{11} /shot. Using this result as the ion flux F_{ion} and the calculated sputtering yield Y_{sputt} in the eq., we can predict the erosion rates ΔT for the three films. The ratios of these calculated values are C : Ru : Au = 2 : 6 : 16, which are close to the experimental results of 1 : 5 : 15. Compared with the calculated erosion rate for C, the measured value for the DLC is slightly smaller. This difference may be due to the different types of carbon involved: high hardness DLC in the experiment vs. normal carbon (graphite) in the calculation.

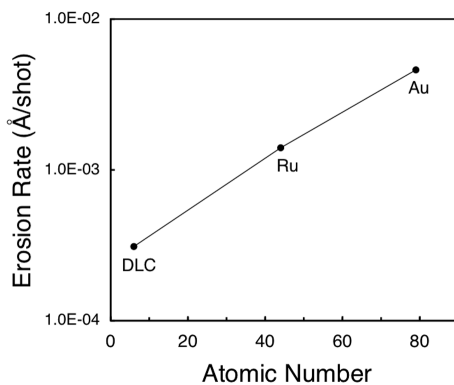


Figure 2. Erosion rate of the DLC, Ru, and Au films as measured by QCM with a debris incidence angle of 20°.

Sn DPP X-ray sources are currently used as extreme ultraviolet lithography (EUVL) sources in the industrial mass production of semiconductors. These sources emit X-rays at a wavelength of 13.5nm, and employ grazing incidence Ru mirrors. As shown in Fig.3, the DLC sputtering yield by Sn ions is similar to the one by Xe ions, as calculated by the SRIM code. Therefore, a DLC mirror may also be resistant to Sn sputtering. Of course, because the Sn plasma debris includes both “deposition” and “sputter” types of particles, additional debris mitigation techniques are necessary. However, we predict that a DLC mirror will enjoy a longer lifetime in a Sn plasma source.

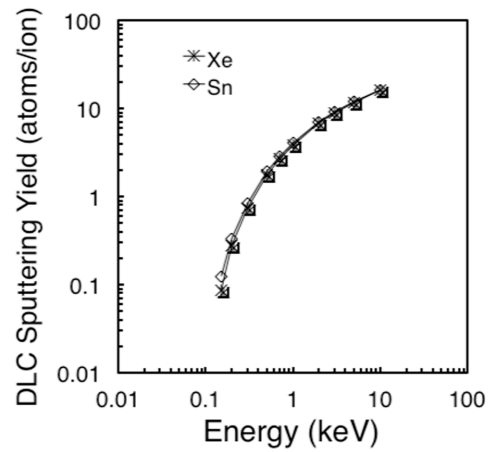


Figure 3. DLC sputtering yield by Xe and Sn ions, calculated with the SRIM code.

References

- [1] S.Amano *et al.*, Appl. Opt., **52**, pp.3845(2013).